Experimental methods for flow and aerosol measurements in human airways and their replicas

Frantisek Lizal, Jan Jedelsky, Kaye Morgan, Katrin Bauer, Jordi Llop, Unai Cossio, Stavros Kassinos, Sylvia Verbanck, Jesús Ruiz-Cabello, Arnoldo Santos, Edmund Koch, Christian Schnabel

PII: S0928-0987(17)30465-7
DOI: doi: 10.1016/j.ejps.2017.08.021
Reference: PHASCI 4179

To appear in: *European Journal of Pharmaceutical Sciences*

Received date: 29 May 2017
Revised date: 14 August 2017
Accepted date: 17 August 2017

Please cite this article as: Frantisek Lizal, Jan Jedelsky, Kaye Morgan, Katrin Bauer, Jordi Llop, Unai Cossio, Stavros Kassinos, Sylvia Verbanck, Jesús Ruiz-Cabello, Arnoldo Santos, Edmund Koch, Christian Schnabel , Experimental methods for flow and aerosol measurements in human airways and their replicas, *European Journal of Pharmaceutical Sciences* (2017), doi: 10.1016/j.ejps.2017.08.021

Experimental methods for flow and aerosol measurements in human airways and their replicas

Authors: Frantisek Lizal[1], Jan Jedelsky[1], Kaye Morgan[2,3,4], Katrin Bauer[5], Jordi Llop[6], Unai Cossio[6], Stavros Kassinos[7], Sylvia Verbanck[8], Jesús Ruiz-Cabello[9,10], Arnoldo Santos[10], Edmund Koch[11] and Christian Schnabel[11]

[1]Faculty of Mechanical Engineering, Brno University of Technology, Technicka 2896/2, Brno 61669, Czech Republic.
[2]School of Physics and Astronomy, Monash University, Clayton, Victoria 3800, Australia
[3]Institute for Advanced Studies, Technical University of Munich, Lichtenbergstrasse 2 a, 85748, Garching, Germany
[4]Chair of Biomedical Physics, Department of Physics, Technical University of Munich, James-Franck-Str. 1, 85748 Garching, Germany
[5]Institute of Mechanics and Fluid Dynamics, TU Bergakademie Freiberg, Lampadiusstr. 4, 09599 Freiberg, Germany.
[6]Radiochemistry and Nuclear Imaging Group, CIC biomaGUNE, Paseo Miramon 182, 20014 San Sebastian, Gipuzkoa, Spain.
[7]Computational Science Laboratory, Department of Mechanical and Manufacturing Engineering, University of Cyprus, Kallipoleos Ave. 75, Nicosia 1678, Cyprus.
[8]Respiratory Division, University Hospital UZ Brussel, Vrije Universiteit Brussel, Belgium.
[9]Universidad Complutense de Madrid (UCM), Av. Séneca, 2, 28040 Madrid, Spain
[10]Ciber de Enfermedades Respiratorias (CIBERES), Av. Monforte de Lemos, 3-5. Pabellón 11. Planta 0 28029 Madrid, Spain
[11]TU Dresden, Faculty of Medicine Carl Gustav Carus, Anesthesiology and Intensive Care Medicine, Clinical Sensoring and Monitoring, Fetscherstrasse 74, 01307 Dresden, Germany

Abstract: Recent developments in the prediction of local aerosol deposition in human lungs are driven by the fast development of computational simulations. Although such simulations provide results in unbeatable resolution, significant differences among distinct methods of calculation emphasize the need for highly precise experimental data in order to specify boundary conditions and for validation purposes. This paper reviews and critically evaluates available methods for the measurement of single and disperse two-phase flows for the study of respiratory airflow and deposition of inhaled particles, performed both *in vivo* and in replicas of airways. Limitations and possibilities associated with the experimental methods are discussed and aspects of the computational calculations that can be validated are indicated. The review classifies the methods into following categories: 1) point-wise and planar methods for velocimetry in the airways, 2) classic methods for the measurement of the regional distribution of inhaled particles, 3) standard medical imaging methods applicable to the measurement of the regional aerosol distribution and 4) emerging and nonconventional methods. All methods are described, applications in human airways studies are illustrated, and recommendations for the most useful applications of each method are given.

Keywords: computational fluid particle dynamics, human airways, lungs, experimental methods, medical imaging, aerosol deposition, velocimetry techniques, flow measurement techniques, gas–liquid two-phase flow, CFD validation

Nomenclature and units

A	radioactivity	(Ci, Bq)
c	number concentration	($1/m^3$)
CPS	counts per second	(1/s)
CV	coefficient of variation	(–)
D	diameter	(m, μm)
d	the Gaussian beam diameter	(m)
D_{qr}	mean droplet diameter with indices q and r used for determination of the diameter type	(μm)
E	energy	(MeV, keV)
f	frequency	(Hz)
FD	fibre density	($1/mm^2$)
f_w	weighting factor	(–)
N	number of particles, number of radioactive atoms	(–)
n	refractive index	(–)
$\dot{n}$	mean sampling rate	(Hz)
p	P value, or calculated probability	(–)
PSD	power spectral density	(m^2/s)
$R2^*$	transverse relaxivity	(s)
S	area	(m^2)
s	fringe spacing (fringe separation distance)	(m)
SR	spatial resolution	(1/m)
T	time period	(s)
t	time	(h)
$T1$	longitudinal relaxation time	(s)
$T_{1/2}$	half-life of a radioisotope	(h, min, s)
$T2$	spin–spin relaxation time	(s)
$T2^*$	decay of transverse magnetization	(s)
TDF	total deposited fraction	(–)
TI	turbulence intensity	(–)
TV	tidal volume	(l)
u	velocity	(m/s, cm/s, mm/s, μm/s)
V	volume	(ml)
$\dot{V}$	flow rate	(l/s, l/min, ml/s)
x, y, z	Cartesian coordinates	(m)
%ID/g	percentage of injected dose per gram of tissue	(1/g)

Greek characters

β	attenuation of the x-ray	(–)
Δt	time lag of two signals (LDA, PDA), delay between laser pulses (PIV)	(s)
$\Delta\varphi$	phase difference	(rad)
δ	change of the phase of the x-ray	(–)
ν	kinematic viscosity	(m^2/s)
Θ	Intersection angle of two beams	(deg)
Λ	wavelength of the laser light	(nm)
λ	decay constant	(–)

τ_I	integral time-scale	(s)
Φ	parameter of the PDA system	(–)

Subscripts

0	initial number
B	frequency shift
b	breathing
D	Doppler
i	index number
in	inhaled
max	maximum
n	normal velocity component
out	exhaled
p	particle
T	transit

Dimensionless numbers

Re	Reynolds number
Stk	Stokes number
α	Womersley number

Abbreviations

Abbreviation	**Full expression**
[^{18}F]FDG	2-deoxy-2-(^{18}F)fluoro-D-glucose
2C, 3C	two-component, three-component
2D, 3D, 4D	two-dimensional, three-dimensional, four-dimensional
AM	Additive Manufacturing
aOCT	anatomical OCT
AUC	area under the curve
CCA	Constant Current Anemometer
CCD	Charge-coupled device
CFD	Computational Fluid Dynamics
CFPD	Computational Fluid Particle Dynamics
CMOS	Complementary metal–oxide–semiconductor
COPD	chronic obstructive pulmonary disease
CS	Compressed Sensing
CT	Computed Tomography
CTA	Constant Temperature Anemometer
DTPA	diethylene triamine penta acetic acid
DOTA	1,4,7,10-tetraazacyclododecane-1,4,7,10-tetraacetic acid
EIT	Electrical Impedance Tomography
FBP	Filtered-Back-Projection
FD-OCT	Fourier Domain OCT, also Frequency Domain OCT
FDA	Food and Drug Administration
FDML	Fourier domain mode locked
FOV	field of view
fps	frames per second

FWHM	Full Width at Half Maximum
GC–MS	Gas Chromatography – Mass Spectrometry
HFOV	High Frequency Oscillatory Ventilation
HUA	human upper airways
HWA	Hot-Wire Anemometry
ICRP	International Commission on Radiological Protection
ID	injected dose
LD	Laser Doppler
LDA	Laser Doppler Anemometry
LDV	Laser Doppler Velocimetry
LES	Large Eddy Simulation
MEMS	microelectromechanical systems
MPI	Magnetic Particle Imaging
MRI	Magnetic Resonance Imaging
MRV	Magnetic Resonance Velocimetry
NIR	near infrared wavelength range
NP	nanoparticle
OCT	Optical Coherence Tomography
OFDI	optical frequency domain imaging
OSEM	Ordered Subset Expectation Maximization
PBPK	physiologically based pharmacokinetic
PCM	Phase Contrast Microscopy
PCXI	Phase Contrast X-ray Imaging
PD	Phase Doppler
PDA	Phase Doppler Anemometry, Particle Dynamics Analysis
PDI	Phase Doppler Interferometer
PDMS	polydimenthylsiloxane
PDPA, P/DPA	Phase Doppler Particle Analyzer
PET	Positron Emission Tomography
PIV	Particle Image Velocimetry
ppm	parts per million
ppp	particles per pixel
PTV	Particle Tracking Velocimetry
px	pixel
RANS	Reynolds-averaged Navier–Stokes
RMS	Root-Mean-Square
ROI	region of interest
RP	Rapid Prototyping
SCPN	single-chain polymer nanoparticle
SD-OCT	Spectral Domain OCT
SEM	Scanning Electron Microscopy
SLA	Stereolithography
SMI	Soft Mist™ Inhaler
SNR	signal to noise ratio
SPECT	Single Photon Emission Computed Tomography
SUV	Standard Uptake Value
TD-OCT	Time Domain OCT
TEM	Transmission Electron Microscopy
UTE	ultra short echo
VOI	volume of interest

1. Introduction

Several methods for predicting the results of pulmonary drug delivery have established themselves in recent years. One such method, used for drugs with very high bioavailability, predicts the total expected lung dose for healthy lungs and uses that to estimate the concentration of drug in blood plasma against time (expressed by the area under the plasma drug concentration–time curve, AUC) (Olsson et al., 2013). In order to improve these predictions, two distinct trends are emerging that require accurate predictions of local (as to opposed global/total) deposition. First, there is a push towards the development of drugs that are customized for a particular class of patients, e.g. for asthma or chronic obstructive pulmonary disease (COPD) patients. Even though they are not likely to be achieved in the very near future, inhalational products that are tailored to individual patients or classes of patients are envisioned and their development also relies on accurate estimates of local deposition (Bettoncelli et al., 2014; Forbes et al., 2016). On the other hand, there is an increasing momentum for the use of large-scale population studies to be used as the basis for the development of statistical correlations linking airway structural, functional and phenotype parameters to the observed trends of regional deposition for various patient classes. Such statistical trends can then form the basis for the development of improved physiologically-based pharmacokinetic (PBPK) models for use in the drug development, approval and regulation cycle (Backman et al., 2017). In both of these emerging trends, the synergistic use of experimental and *in silico* methods is playing a central role.

Impressive work has been carried out in the area of *in silico* modelling of aerosol flow and deposition in last decades. This approach is based largely on Computational Fluid Particle Dynamics (CFPD), developed as a branch of fluid mechanics and involving numerical analysis of fluid and particle flows in digital representations of real or idealized geometries. CFPD is capable of calculating fluid, particle and structure interactions provided the correct boundary conditions were set. The general overview was given e.g. by (Tu et al., 2013).

Overall lung deposition can be predicted both experimentally and by CFPD with sufficient precision nowadays. It is also possible to calculate "regional" deposition at the macroscale, usually per lung lobe or per generation. These equations are available e.g. from the International Commission for Radiological Protection (ICRP) (Bailey, 1994). However, assessing the local deposition at the microscale (e.g. in units of mm^2), either experimentally or *in silico*, remains a challenging task. Experimental methods, particularly in imaging, face problems with difficult and obstructed access to the deposition sites in the human lungs, limited resolution, and/or associated health hazards depending on the particular method. In this regard, *in silico* methods can fill the gaps left by *in vivo* methods that use the current state of the art in pulmonary imaging. *In silico* methods can provide detailed information regarding the deposition of aerosol particles in individual airway branches. The typical workflow for such studies begins with the acquisition of chest Computed Tomography (CT) scans of the patient, followed by the use of specialized software to segment the airways and generate CFPD meshes on which the discretized form of the governing transport equations can be solved. The resolution limitations of current imaging equipment set the limit of such detailed airway reconstruction between roughly the 7^{th} and 10^{th} bronchial generation, depending on the specific airway configuration for each patient. *In silico* estimates of aerosol deposition in the upper part of the bronchial tree using one of the CFPD methods called Large Eddy Simulation (LES) have become fairly routine, especially under conditions of steady inhalation rate. However, for drug development one needs to consider the entire lung and the full respiratory cycle, allowing for variations in possible inhalation manoeuvres. To do this requires coupling the LES simulation in the upper airways with reduced models for the central bronchial tree and models of the acinus. This represents an area of intense research and development with different groups adopting varying approaches for such coupled simulations (Kolanjiyil and Kleinstreuer, 2013; Koullapis et al., 2017a; Longest et al., 2012). The impact of such integrated simulations on drug development and patient care could potentially be quite strong, yet a number of conditions need to be satisfied before these approaches can deliver on their promise.

In modelling airflow and deposition in the various regions of the lung, a number of choices can be made in terms of both the computational tools used and the physical effects that are modelled. As a

result of work carried out over the last decade by several groups, many of the factors that contribute to the fidelity of *in silico* studies are now understood much better. However, this understanding should be documented and clearly spelt out in the specific context of deposition studies in human airways.

The community consensus is that the airflow in the mouth, extra-thoracic and upper tracheobronchial tree can be resolved with satisfactory accuracy using LES (Choi et al., 2009; Jayaraju et al., 2008; Koullapis et al., 2017b; Longest and Holbrook, 2012). But even within LES there are a multitude of choices to be made regarding the use of inlet and boundary conditions, the use of sub-grid scale models, the discretization schemes and the mesh design. Furthermore, these issues are often interconnected, for example, the accuracy of a particular discretization scheme often depends on the particular mesh design adopted. While a large volume of information is available in the literature regarding the factors that affect the performance of LES, these are often examined in the context of canonical flows. When LES is used in the context of aerosol deposition studies, additional questions arise related to the particle tracking algorithms and the modelling of physical effects acting on the dispersed phase. For example, it is often argued, on the ground of dimensional considerations, that certain forces such as the Saffman lift force should be negligible in airway deposition simulations (Finlay et al., 1996). However, this assumption has not been subjected to a systematic validation. Therefore, there is currently a need for systematic evaluation and validation of LES that will specifically target best practice recommendations for *in silico* deposition studies. Such evaluation and validation must rely at least in part on independent flow and deposition data originating from studies on human airway replicas or directly *in vivo*. The problem one is faced with is that *in silico* methods are recruited to fill the gap created by the limited resolution of current imaging technologies, yet the validation and verification of *in silico* methods must, at least to some extent, rely on such limited data. This apparent paradox makes necessary the careful selection of data validation metrics that are both meaningful and reliable at the same time.

Clear guidelines on best practice in the design of *in silico* deposition studies must be the result of a systematic effort that will result in the necessary community consensus. The value of such a consensus from the purely technical point of view is clear. The significance, however, extends beyond technical considerations. One has to appreciate that such a community consensus is a necessary ingredient for enabling the routine use of *in silico* population studies in the drug development and regulatory approval cycle. Without clearly spelt out design rules and validation metrics, both the pharmaceutical industry and the regulatory agencies are likely to resist admitting *in silico* methods in their workflow. Without acceptance from these key stakeholders, the potential of *in silico* methods is destined to be kept locked in the realm of academic and research institutions. These considerations should make clear that the establishment of best practice guidelines for simulation methods used in airway deposition studies is of paramount importance to the future of *in silico* population studies for inhaled drug development.

The main aim of this paper is to provide an overview of experimental techniques that can be used to validate *in silico* methods. We have prepared a summary of principles, features, precisions, strengths, weaknesses, and practical applications of available experimental methods applied on flow and aerosol measurements in human airways and their replicas. Our work can be used as a guide for the selection of a suitable lung geometry and the correct validation approach. It should help the readers to understand the physical limitations of various experimental methods and hence to shape realistic expectations. Experimentalists may find this paper useful when deciding the appropriate experimental method for their research in terms of experimental acquisition and interpretation, and in the context of any existing findings with the described techniques.

This paper also aims to diminish the remaining gap between pharmaceutical/medical and engineering communities, which limits the practical use of *in silico* modelling in medical applications. A frequent source of dispute is how much an *in silico* model simplifies the reality. Some experts insist on using solely *in vivo* measurements for validation of *in silico* models. However, as will become obvious in the next chapter, performing simulations on the identical *in vivo* geometry with completely controlled and correct boundary conditions is virtually impossible. Therefore, measurements are performed on replicas of human airways for validation purposes. In that case, extreme attention

should be paid to include all the relevant forces (inertial, gravity, thermophoretic and electrostatic force, etc.) and features of materials (surface roughness, electrical conductivity…). However, controlling all these conditions is significantly easier than performing measurements *in vivo*. Nonetheless, it is important to understand limitations of this approach. The replica-based validated results represent an indispensable source of data, however, they have to be contextualised using the *in vivo* data, to make sure that all the relevant phenomena were covered. In respect to this issue, we decided to include experimental methods applicable to replicas, *in vitro,* and *in vivo* set-ups in order to cover the complete range of possible needs of researchers. Nevertheless, measurements performed on animals are not included in this review (except for the emerging methods where animal studies are the only source of data), although they surely provide an important source of information. Animal-based experiments represent a very broad spectrum of data, and cannot be covered here with the thoroughness they deserve.

We need to clarify several terms that are frequently used in the related literature, however, sometimes with slightly different meaning. In this paper, we understand by the term *in vivo* the experiments performed on a whole, living human subject; the term *ex vivo* refers to measurements performed on tissue detached from an organism and placed in an external environment with minimal alteration of natural conditions; the term *in vitro* is used to indicate studies performed with cells, or biological molecules outside their normal biological context. This is contrary to the CFPD papers where this term sometimes also includes experiments on physical replicas of parts of the human body (normally without any cells or intentionally introduced living cultures). As we wanted to detach this special group, we designate these experiments as being performed "in replica" (not italicized, as it is used verbatim and not constructed from Latin). The term *in silico* denotes computer simulations, and lastly, *in situ* means performed "on site" or "in place".

Validation of CFPD predictions

The reliability of CFPD predictions is directly related to the method and data used for validation. Longest and Holbrook (2012) emphasize the need for improved experimental data sets to better validate computational predictions in local lung regions. It was recognized, e.g. by (Fleming et al., 2015), that the local deposition will remain questionable unless proper validation is performed. A troublesome fact is that even the meaning of the term "validation" is not fully accepted among researchers in different fields (Oldham, 2006). The exhaustive discussion of all aspects of Computational Fluid Dynamics (CFD) validation was performed elsewhere (Holbrook and Longest, 2013; Oldham, 2006). Following the recommendations that are given in their studies we need to: 1) clarify our understanding of the term validation, and 2) describe what can be done to improve the accuracy of numerical predictions using both the currently available and emerging experimental methods.

For this paper, we have decided to adopt the definition of validation given by (Versar Inc., 1988) "The process of defining the range of problems or situations for which model predictions are satisfactory". The problem is that even if the model agrees well with experiments for a specific set of boundary conditions, it does not mean it will agree if the boundary conditions were to change. Moreover, there can always be some suspicion that the agreement is only fortuitous.

Another issue that cannot be disregarded is connected with measurement errors and uncertainties. Therefore, we include a paragraph on associated uncertainties in the description of individual measurement methods.

2. Airway model geometry and airway replicas

An acquisition of the airway geometry is the first step for both CFD calculations and experiments in replicas. The fidelity of the geometry is a crucial issue, which may result in the failure of an attempt to validate the CFD predictions. It has been proven, e.g. by (Kelly et al., 2004a, b), that the quality of the inner surface of the airway replica has a significant effect on the measured deposition. Kelly et al.

manufactured two models of the same nasal cavity using different stereo-lithographical methods and compared their results with data acquired on other three replicas manufactured by micro-milling or hand carving from the same Magnetic Resonance Imaging (MRI) scans. They found that the deposition efficiency varied significantly among the replicas for particles from 1 to 10 μm in size, whereas the differences for particles in the size range 0.005 to 0.15 μm were negligible. Interestingly, the deposition efficiency did not form a trend with increasing surface roughness even for the inertial regime particles. Instead, the authors speculated that the discontinuities in replicas, that are assembled from several thin elements, can have a major effect on the increased deposition. It is obvious that even a slight change of geometry can significantly alter the results and hence it makes no sense to validate results of CFPD at the microscale (the local deposition sites) by experiments performed on a different geometry.

The real human lungs represent a very complex three-dimensional (3D), multiscale, flexible geometry with moving boundaries, which has to be simplified for both CFD and experimental use. The first approximate airway geometries became available since the 1970s, when the idealized symmetric Weibel A model (Weibel, 1963) and the asymmetric model by Horsfield et al. (1971) were published, followed by the model by Raabe et al. (1976). These geometries were based on morphometric measurements of human lungs and statistical evaluation of the lower airways. These models are still frequently used, often geometrically truncated to a different extent. Some investigators applied even simpler models, such as the trivial Y-shape, to study lung flow in a single symmetrical bifurcation (Corieri and Riethmuller, 1989; Lieber and Zhao, 1998; Peattie and Schwarz, 1998). A more complex model comprising five generations of airways, made of straight hollow glass tubes, was used recently by Kerekes et al. (2016). A common feature of all these idealized models is a significant simplification of the actual lung geometry, by neglecting surface irregularities, physiological traits, protuberances and surface roughness.

With the onset of 3D imaging methods (CT and MRI), realistic models have become available via scans of a living human or *ex vivo* preparations of the human lungs. Examples of such models are those CT models published by Hopkins et al. (2000), Clinkenbeard et al. (2002) or Schmidt et al. (2004), and the MRI model used by Guilmette et al. (1989). Such models were adapted for Hot-Wire Anemometry (HWA), Particle Image Velocimetry (PIV) or Phase Doppler Anemometry (PDA) measurements (Elcner et al., 2016; Jedelsky et al., 2012). The process of development of such a model was described e.g. by (Lizal et al., 2012; Verbanck et al., 2016).

It has to be noted that certain details of the geometry are always altered or lost during the process of imaging and, in the case of an experimental approach, also during fabrication of the physical replica. Generally, the geometry can be acquired to the 10^{th} generation from *in vivo* measurements at most and to approximately the 17^{th} generation from high-resolution CT of a rubber cast originating from *in vitro* preparation (Schmidt et al., 2004). Firstly, not all the details of the airway surface can be detected by the imaging method. Secondly, some of the resolved physiological protuberances are then lost during the segmentation of the data and digital processing. Generally, it is difficult to get below a resolution of 0.6 mm in the final images even when using high-resolution CT and MRI (Mirsadraee and van Beek, 2015). It means that structures below 1 mm in size tend to be smoothed out in the geometries acquired using standard medical imaging methods.

Let us now focus on the methods that are available for the manufacture of a physical replica of airways. The first replicas were made by casting (Phalen et al., 1973). One such replica, which has been used for many experimental studies (e.g. (Su and Cheng, 2015; Su and Cheng, 2006; Zhou and Cheng, 2000)), was manufactured at Lovelace Respiratory Research Institute (Cheng et al., 1999). The oral part of the replica comes from a dental impression of the oral cavity from a volunteer and the rest of the airways come from a cadaver. These two parts, sourced from different individuals, were moulded in wax and coupled together by hand sculpture (Cheng et al., 1997). Then a production mould from silicone rubber was made to cast the secondary wax casts. Each final replica was made from one secondary wax cast by applying a conductive silicone rubber compound and melting the wax core in boiling water. The precision of the manufacturing process and the repeatability of the geometry was not specified by the authors, but it likely did not exceed ± 1 mm.

Micro-milling was used to produce the model of (Guilmette and Gagliano, 1994), and reported to have an accuracy of 0.02 mm. The same team later produced a second replica using the same tools (Zwartz and Guilmette, 2001), however, they claimed that the second replica is a better representation of the original MRI scan with 3mm scan intervals, as a more accurate trace of the MRI was used. Moreover, hand filing was performed to smooth out the discontinuities between adjacent plates of the replica. This led to a 9% difference in olfactory volume between the replicas although they came from the same original images (Kelly et al., 2004a).

A different approach was used by (Kerekes et al., 2016), who connected smooth glass tubes using standard glass manufacturing methods to obtain a simplified model of the human airways. In their case the repeatability of the geometry reproduction was not reported, however, if they used high precision glass tubes (e.g. (Schott Medica GmbH, 2017)) we can assume the tolerance of the tube diameters to fall between ± 0.003 and ± 0.01 mm. The precision of connecting angles of the joined tubes is difficult to assess.

The majority of replicas used in recent years are, however, produced by rapid prototyping (RP, sometimes also referred to as additive manufacturing, AM, methods), namely 3D printing. There have been several reviews published on applications of 3D printing in medicine recently (Lee Ventola, 2014; Liaw and Guvendiren, 2017; Yap et al., 2017). All these studies predict an illustrious future for 3D printing in many medical applications, such as dentistry, tissue and organ implantation, anatomical models, and drug formulation. There are four main groups of 3D printing techniques (Liaw and Guvendiren, 2017): 1) **Vat polymerization-based printing**, which includes stereolithography (SLA) and direct light processing and their derivatives. These techniques use laser light which is directed to cure a liquid resin in a vat, layer by layer. 2) **Powder-based printing** (e.g. selective laser sintering, electron beam melting), which is characterized by local heating and fusing of a powdered material. 3) **Droplet-based printing** (e.g. multijet modelling, binder jetting), which resembles classical ink printing, but upgraded to a third dimension. 4) **Extrusion-based printing**, namely fused deposition modelling, which extrudes suitable composite through a hot nozzle.

The precision of printing differs in lateral and vertical directions, as the printed objects are always built layer by layer. The minimal thickness of the layer, therefore, limits the resolution in the vertical dimension. The powder- and extrusion-based methods are generally less precise (Islam et al., 2017), although they represent an attractive choice due to their low price. (Islam et al., 2017) measured the accuracy of objects printed by SLA and powder-based methods, and found that SLA was generally far more precise, although it was possible to get better dimensional accuracy in the lateral directions using the powder printer. However, the SLA was more consistent, which meant that, for example, the hole in the object had a slightly smaller diameter, but the diameter did not significantly change through the hole, whereas for the powder printer the diameter oscillated, resulting in more jagged surface. The maximal dimensional errors were in the order of hundreds of μm for both methods, when the printed object size was 126 mm. Another comparison of the accuracy in a medical application of 3D printing methods was published by Salmi et al. (2013). In their case, the droplet-based method proved to be the best with a mean difference in dimensions of 0.18 ± 0.13%.

It should be noted that the accuracy of the dimensions of the particular replica of airways depends on the particular technique, precision of the machine and competence of the operator. Additional problems can be caused by any artificial features or textures that are introduced as an artefact of the fabrication process. On the other hand, when the same digital geometry is produced using an identical 3D printer, the repeatability is undoubtedly higher than any attempt to measure within the same geometry *in vivo*.

Several other problems arise in the physical airway replicas. First of all, they usually have rigid walls. This does not cause significant error in the upper airways and the airways supported by cartilaginous rings, however, in the lower airways this may lead to misinterpretation of results. Another source of possible error is the electrical conductivity of the replica. If charged particles arrive in a non-conductive replica, they create mirror charges on the wall and are deposited, and this mechanism is largely impossible to detect during the evaluation of the data, as the electrostatic mechanism of deposition is difficult to include into the deposition equations. Last, but not least, the inner surface of

real lungs is covered by a mucous layer, which should be simulated in replica. However, it is usually impossible to mimic all features of the lining, e.g. density, viscosity, conductivity, movement driven by cilia etc. Similar problems have to be solved during CFD geometry preparation, however, it seems clear that simulating these conditions in the *in silico* airways is significantly easier than simulating these conditions in a physical lung replica.

It is obvious that issues with inducing and controlling the flow are indivisible from experiments performed in replicas of human airways. However, the simulation of physiologically realistic flow is not a trivial issue. The main problem is grounded in the fact that the replicas do not contain complete lungs and hence the missing parts must be simulated. The situation is somewhat easier for flow measurement studies. The easiest solution is to simulate only stationary inhalation (or exhalation). Then only the flow distribution has to be solved e.g. using linear resistors. If an oscillatory flow is to be simulated, the flow distribution can be provided by several cylinders with pistons, whose movement is controlled using a computer (Ramuzat and Riethmuller, 2002). It should be noted that the realistic course of flow rate is not easy to mimic and hence the sinusoidal course of breath is most frequently used. For aerosol deposition studies, the circumstances are even more complex. Researchers need to distinguish between 1) the particles deposited in the replica during inhalation, 2) the particles that would pass the simulated regions and would deposit in deeper regions during inhalation, 3) the particles deposited in deep regions or 4) the replica during exhalation and 5) particles exhaled after the complete cycle. Therefore, the inhalation component and the exhalation component are simulated separately, where all the particles passing through are usually collected on filters without any other information on their possible fate in real lungs. Moreover, the majority of such experiments are performed for steady inhalation or exhalation only. Simulations of aerosol deposition during cyclic inhalation are very rare (Kim and Fisher, 1999).

Some of the above-mentioned problems are naturally solved during *in vivo* measurements. However, repeatability and reproducibility remain an issue there. It is necessary to instruct the volunteers to breathe steadily and monitor the breath with a pneumotachograph or another suitable instrument, ideally using feedback to help the volunteer establish a repeatable breath pattern. It cannot be expected that the breathing pattern of a live human will follow any machine-like rhythm.

3. Flow and particle velocimetry in the airways

The main source of data for validation of calculated velocity fields and other flow characteristics are experiments performed in replicas of lungs. The reason is obvious – the obstructed view and complicated access to the human airways. We will focus on methods routinely applied in fluid mechanics, which can be divided into two groups based on their influence on the fluid. The non-intrusive methods usually require a direct optical path to the replica, however, some of them can provide planar or even volumetric data. In this chapter, we paid special attention to laser Doppler based methods and their application in human airway flows, as this topic has not been compiled yet and they are able to bring important data on turbulent characteristics of the flow, provided the proper data processing was performed. The second group, the intrusive methods, is represented by hot-wire anemometry (HWA).

3.1. Hot-Wire Anenometry in lungs

The first in-depth studies of flow profiles in replicas of human lungs were performed in the 1960s, after Weibel (1963) and Horsfield and Cumming (1967) published their morphometries of human lungs. First flow visualizations were performed using smoke and photography. Velocities were measured by HWA often supplemented with Pitot tubes to sense the flow direction.

The HWA was developed at the beginning of the 20th century and quickly became a fundamental tool for turbulence measurements. The method is based on the measurement of the cooling effect of

surrounding flow on a heated element, usually a wire or a thin metal film (Bruun, 1995). The heat transfer from the element depends on the temperature, geometrical configuration and physical properties of both the element and fluid. Two modalities that differ in the way of heating the element are available currently: a) Constant Current Anemometer (CCA) and b) Constant Temperature Anemometer (CTA), noting the latter is more popular as it is easier to use and is therefore implemented in the majority of commercially available instruments. However, both modalities are equivalent in regards to the electronic noise and measurement frequencies (Bestion et al., 1983).

3.1.1. Constant Temperature Anemometer (CTA) principle

The CTA modality utilizes a Wheatstone bridge to compensate the cooling effect of the flowing fluid on the probe while maintaining a constant wire temperature (see Fig. 1). The current flowing through the wire creates heat, which is equal to the (mainly convective) heat losses to the fluid, once in the state of equilibrium. After the change of velocity, a servo amplifier immediately changes the current to the wire to keep the bridge in balance, and hence the wire has constant resistance, and consequently constant temperature.

The voltage drop across the sensor is proportional to the velocity of the fluid flow. As the heated elements are usually wires of several μm in diameter, they have very low thermal inertia and therefore allow the measurement of extremely fast fluctuations, up to several hundred kHz in the best configuration (Jensen, 2004). Because the voltage output is not directly proportional to the velocity, the voltage output has to be calibrated prior to the measurement (Bruun et al., 1988). It has to be noted that the heat transfer from the sensor is a function of many properties, namely heat conductivity, viscosity, density, concentration and of course the velocity of the fluid.

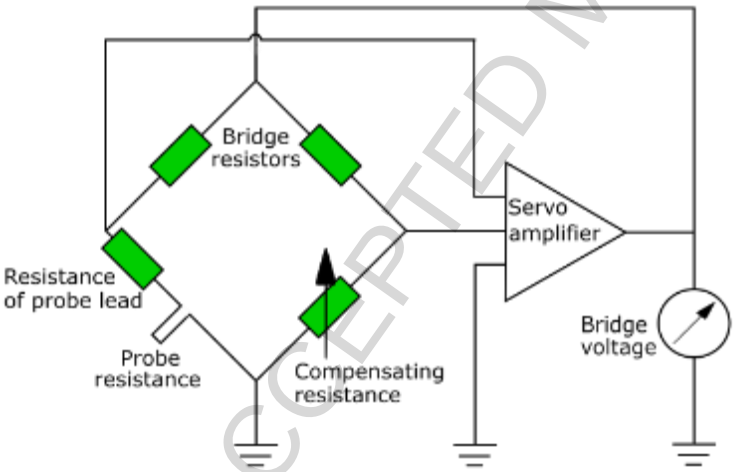

Fig. 1. The principle of CTA.

The main advantages of HWA are:

- fast frequency response: measurements up to several hundred kHz possible,
- analogue output signal — both time domain and frequency domain analysis can be carried out,
- no seeding is required,
- high signal to noise ratio (SNR): resolution of 1 part in 10,000 is accomplished,

- velocity measurement: measures velocity magnitude and fluctuations, also turbulent characteristics like Reynolds stresses or vorticity possible (Lemonis, 1997),
- wide velocity range (few cm/s to supersonic speed),
- allows measurement of other fluid quantities (temperature, concentration),
- relatively cheap.

The main drawbacks of HWA are:

- intrusive technique — disturbs the velocity field,
- rectification error — insensitive to a reversal of flow direction (which appears also in a flow with high turbulence intensity (TI)),
- contamination: deposition of impurities in flow on the sensor alters the calibration characteristics and reduces the frequency response,
- fragility — probe breakage and burn out,
- single-point measuring method,
- inaccurate at low velocities due to natural convection,
- calibration is required,
- accuracy of HWA is really a function of calibration, contamination, temperature changes and other factors, which generally limit the accuracy to a few percent.

Applications of HWA in lung flow studies

Probably the first study to use HWA in a simple model of human airways was Schroter and Sudlow (1969). They manufactured Y-shaped single and double bifurcation models and measured inspiratory and expiratory velocity profiles using a single-wire probe. They clearly demonstrated that developed laminar parabolic flow cannot be assumed in lungs, as each bifurcation disturbs the flow and the disturbances do not dissipate before the next bifurcation. The influence of the local geometry at a junction was also investigated. Change of radius of curvature of the outer wall at the junction in a ratio of 1:4 caused the appearance of flow separation, which was expected to influence the local mass transport.

Another attempt to measure the flow in human lungs was undertaken by Olson et al. (1973), who used Pitot tubes and HWA to measure velocity direction and flow instabilities, respectively. Their geometry covered the airways from the mouth to the second bifurcation and was made of clear rubber. Velocity contours in nine cross sections of the airways were presented demonstrating basic features of the flow. The authors observed a velocity peak on the posterior portion of the trachea as a result of the vocal cords shape. Also, flow instabilities were discussed based on fluctuating velocity measured by HWA. The authors noticed that random fluctuations exist even in sub-lobar bronchi where the Reynolds numbers, Re, fall below 100. They explained that turbulence is generated by the separation just below the larynx, where the disturbances are so large that they are transported several bifurcations downstream. Despite the inspiring discussion, their data can hardly be used for validation of CFD results as many important details of the geometry and experimental setup are missing.

The most exhaustive measurements using HWA in a model of human lungs was published in a series of papers by a team from McGill University, Canada (Chang and Elmasry, 1982; Isabey and Chang, 1982; Menon et al., 1984). All measurements were performed in a 3:1 scale model of the human central airways based on the Horsfield geometry (Horsfield et al., 1971). The model comprised trachea and the first 2 or 3 generations of branching. In the first study (Chang and Elmasry, 1982) they extended the work of (Schroter and Sudlow, 1969) and published steady inspiratory and expiratory velocity profiles for two flow rates (0.4 and 1.7 l/s in the trachea). They found that the velocity profiles depend on the airway geometry rather than on the Re. The flow separation was observed in the right main bronchus only. By simulating different inlet velocity profiles, they wanted to investigate the effect of

factors like vagal stimulation or upper airway geometry. The results showed that only small differences were found in the main bronchi for the various inlet conditions. Their results also proved that curvature of the left main bronchus influences the evolution of the velocity profile.

The second study (Isabey and Chang, 1982) represents truly admirable work measuring secondary velocities during steady inspiratory and expiratory flow. Measurement of secondary velocities using HWA in a confined space is extremely demanding and even despite maximal effort is burdened with significant measurement error. Isabey and Chang used single slanted hot-wire probes that were inserted axially and rotated around their own axis to determine the secondary velocities. The measurement error ranged between 10 and 30%. The secondary velocities never exceeded 21.5% of the mean axial velocity, while the maximal secondary velocities were always observed near the wall. Several regularly appearing eddies at their typical sites were identified. The authors emphasized the influence of geometry, although they were unable to directly link the geometrical features to their effect on the flow.

The last paper of the series (Menon et al., 1984) focused on oscillatory velocity profiles. The velocity profiles resembled the steady regimes for low Re flows. For higher flow rates the velocity profiles tend to flatter, except in the right main bronchus, where the skewed profile persists even during the highest breathing frequencies.

Nasal airflow patterns were measured using HWA by Hahn et al. (1993). They manufactured a 20:1 scale replica of the nasal cavity based on axial CT. A single velocity component was measured in six planes using 77 probe-inserting holes in total. Hahn et al. managed to create detailed velocity maps that were presented as iso-speed contour plots and normalized velocity profiles. The recorded velocity was used for calculation of turbulence intensity (TI) and total shear stress, which enabled the calculation of longitudinal pressure drop across the nasal cavity.

Johnstone et al. (2004) combined several measurement and visualization methods and presented interesting results acquired on an idealized replica of upper airways. The measurements were performed for seven different inspiratory flow rates in a range between 10 and 120 l/min. Single and X-shape hot-wire probes were used, and therefore mean and Root-Mean-Square (RMS) velocities of two components of velocity can be measured. This study confirmed that the velocity profiles depended primarily on the geometry of airways and were almost independent of the Re.

In summary, HWA provides useful data for the validation of CFD, with the most valuable contribution the temporal resolution available for velocity measurement. However, the usability of the published data for validation purposes is limited, because detailed information on the model geometry and position of the measuring points is often missing. The method is intrusive, which means that insertion of the sensing probe can potentially alter the flow. Also, the measuring uncertainty is relatively high for low velocities (e.g. Hahn et al. (1993) presented uncertainty of ±46% for 0.045 m/s which drops to 14% for 0.09 m/s; for higher velocities, it further decreases to ±5% (Johnstone et al., 2004)). Nevertheless, if the method is available within a given institute, the lung geometry for CFD is available for the manufacture of the physical model, and local development of velocity is of interest, HWA can be recommended as a relatively simple, reliable and yet sufficiently precise tool.

3.2. Laser Doppler based methods

Laser Doppler (LD) based methods and Particle Image Velocimetry (PIV) form a specific group of methods called optical flow measuring methods. They have several common features, namely the optical access requirement and the need for tracing particles to be introduced into the flowing media. The following two subchapters are thus valid for both instrumentations.

3.2.1. Requirements on the physical replicas of airways for optical methods

Optical flow measuring techniques require visual access to the flow field within the object and a limited distortion of the optical path. This disqualifies these methods from *in vivo* application and requires the creation of transparent physical models for these studies. On the other hand, the *in vitro* experiments, in contrast to the studies on living humans, are not subject to ethical rules and do not suffer from the "intra-subject" variability and repeatability problems. The *in vitro* experiments need an appropriate geometrical model of the respiratory tract and its physical realisation. The replicas can be fabricated by different types of RP and casting, or by machine cutting.

The simplest models use cylindrical glass, Perspex, silicon or plastic tubes as the airway representation[1]. A critical issue of the laser beam pair passing through the curved model wall is the beam deflection/refraction and deformation of the measurement volume which increases the measurement uncertainties. The beam deflection is proportional to the wall thickness and the tube curvature and can be calculated according to Durst et al. (1981). This deflection negatively influences the measurement of secondary velocities and the axial velocity and shifts the probe volume from its intended location[2]. The irregular shapes of the realistic models limit the applicability of the optical methods even more.

The optical distortions can be eliminated if the ventilated fluid is replaced with a liquid mixture with the refractive index precisely matched with the model material, which is commonly done with PIV (Adler and Brucker, 2007; Fresconi and Prasad, 2007; Theunissen and Riethmuller, 2008). Up to date, no transparent liquid with the refractive index of air (n_{air} = 1.00) is known. Typical model materials are silicone (for PIV e.g. (Adler and Brucker, 2007; Grosse et al., 2007), for PDA e.g. (Lizal et al., 2012) with an optical refractive index of about 1.41, glass (for LD methods: (Corcoran and Chigier, 2000; Corieri and Riethmuller, 1989) or acrylic plastic (Farag et al., 2000; Tanaka et al., 1999). Especially for 3D evaluation methods, the refractive index must be matched to a precision of 0.01 to guarantee adequate reconstruction of 3D PIV images from the planar images. A mixture of water and glycerin with a mass ratio of 0.42:0.58 (water:glycerin) is typically used as working fluid here (PIV: (Adler and Brucker, 2007; Grosse et al., 2007; Janke and Bauer, 2016), LD: (Corieri and Riethmuller, 1989; Zhao and Lieber, 1994b), and others).

The approach with a liquid is possible if only the velocity field is of interest. However, tracking of aerosol particles is impossible in this manner. For optical studies of particle dynamics inside a realistic geometry, the light refraction in gas as a carrier medium can be minimised by using thin-walled models (Lizal et al., 2012). Elcner et al. (2016) used such a model for PDA measurement and pointed out that manual positioning and beam-crossing adjustment at each measurement point was compulsory, with carefully selected sections for measurement, nevertheless, it was not possible to measure near-walls.

The flow studies using a liquid instead of the air must satisfy the flow similarity condition. The characteristic flow parameters for the case of respiration with an oscillatory flow are the Reynolds number Re and the Womersley number, α, with $\mathrm{Re} = 4TV \cdot f_b \,/\, (\nu \cdot D)$, where *TV* denotes the tidal volume, f_b the breathing frequency, ν the kinematic viscosity and *D* the characteristic diameter of the flow tube. The α represents a relation of transient inertial to viscous forces and is defined by $\alpha = \mathrm{D}/2 \cdot \sqrt{2\pi \cdot \mathrm{f}_b/\nu}$. With a viscosity ratio of ν_{air}/ν_{w+g} = (15.9 × 10^{-6}m²/s) / (8.4 × 10^{-6}m²/s) = 1.9, Re can be reduced by the same factor, and α by $\sqrt{1.9}$. These dimensionless groups must be matched also when scaled models used. This can apply for scaled-up optical measurements in small airways[3] or using mechanical probes (Heraty et al., 2008). In contrast to the flow field studies, the measurements in

[1] For LD measurements of flow in transparent models, circular pipes and behind windows see (Zhang, 2010).

[2] Corcoran and Chigier (2002) however reported the probe shift in the order of 0.3 mm negligible to the scale of their measurement.

[3] For example, Lizal et al. (2011) reported their PDA measurement volume about 0.1 mm^3 which limited the minimum diameter of airway for a reliable measurement to 4 mm.

dispersed two-phase flows involve no scaling since several additional similarity criteria must be matched.

3.2.2. Particle size/shape and dynamics, tracer particles, particle issues

Optical diagnostic methods rely on scattering particles dispersed in the flow to provide the velocity information for the continuous medium (liquid or gas). Durst et al. (1981) specified several requirements for these tracer (seeding) particles; they should be: able to follow the flow, good light scatterers, conveniently generated, cheap, non-toxic, non-corrosive, non-abrasive, non-volatile, or slow to evaporate, chemically inactive and clean. Additionally, the particles must be sufficient in number to provide the required temporal resolution of the flow velocity (Albrecht, 2003) but their mass loading must be small enough to not dump the flow turbulence (Hetsroni, 1989) or alter the flow momentum. The size of the seeding particles must be set via compromise; the scattered light improves with increasing particle size, but the opposite results in terms of fidelity in following the flow and its fluctuations. Particles of around 0.5–1 μm are required for most seeding materials to follow the instantaneous motion of the gas phase to ensure acceptable flow tracking (Melling, 1997). In applications that involve liquids, significantly larger particles in the order of 5–20 μm can be used (Tropea et al., 2007). Tracing accuracy errors are below 1% for the Stokes number of particles in the flow Stk < 0.1 according to Tropea et al. Methods generating particles (for an overview see (Albrecht, 2003; Melling, 1997) with a uniform seeding size are favoured to prevent excessive intensity of light reflected from larger particles producing a background noise and resulting in the low visibility of small particles.

3.2.3. Principles of Laser Doppler (LD)/Phase Doppler (PD) systems

LD instrumentation provides accurate non-intrusive measurements of complex flows with separation regions and flow reversals. Before its introduction, HWA was the only means to measure single-point turbulence quantities. Laser Doppler anemometry (LDA), or Laser Doppler velocimetry (LDV), came into widespread use in the 1970s and the PD technique[4] arrived 20 years later. LDA/PDA instruments became standard and commercially available. These instruments have found important applications for *in vitro* lung flow and aerosol characterizations. LD/PD techniques are point-wise optical methods that capture a Eulerian description of the flow field using embedded fluid markers. They are attractive for CFD (Albrecht, 2003) and provide statistical moments of the flow velocity and, in the case of PDA, also of particle size.

The LDA principle is illustrated in Fig. 2a. A continuous-wave monochromatic laser beam is split into two coherent beams that intersect symmetrically, at a small angle θ, via a transmitting lens. The beams interfere in their intersection volume (the measurement volume) generating a series of parallel planes of light and darkness, referred to as fringes (Fig. 2b). Any small inhomogeneities (particles or bubbles) that are present in the flow will scatter the light as they pass through the fringes. In order to eliminate the ambiguity around which direction a given particle is travelling, the frequency of one of the beams is shifted by f_B, using a Bragg cell, so that the fringe pattern "rolls" with a known velocity. A receiving lens[5] projects the fringe patterns scattered by the particle onto a photodetector (receiver)

[4] Commercially available PD systems are generally referred to according to their manufacturer. The first systems came from Aerometrics, in the USA, and Dantec Dynamics, in Denmark. They were known as Phase Doppler Particle Analyser (PDPA) and Particle Dynamics Analyser (PDA) respectively. The latter became better known as the Phase Doppler Anemometer. TSI, in the USA, later acquired Aerometrics and kept the name PDPA. A third alternative is now available from Artium Technologies, USA, and is offered as a Phase Doppler Interferometer, PDI.

[5] which can be positioned in the forward, side or backscatter direction

which produces a "Doppler burst" signal (Fig. 2c) with a Doppler frequency f_D. This is proportional to the velocity component (u_n) of particle motion normal to the fringes, divided by the fringe spacing s:

$$f_D = f_B + \frac{u_n}{s} = f_B + \frac{2\sin(\theta/2)}{\Lambda} u_n, \quad (1)$$

where Λ is the laser light wavelength. The light signal is then processed to yield the velocity and arrival time of each particle.

The beam intersection provides an optical demarcation of the probe volume as a prolate ellipsoid (Fig. 2c). This measurement volume is usually considerably less than 0.1 mm^3 with corresponding spatial resolution SR = 1 / (characteristic size) ≈ 10^4 m^{-1}. For further details on LDA, we refer to (Durst et al., 1981; Zhang, 2010).

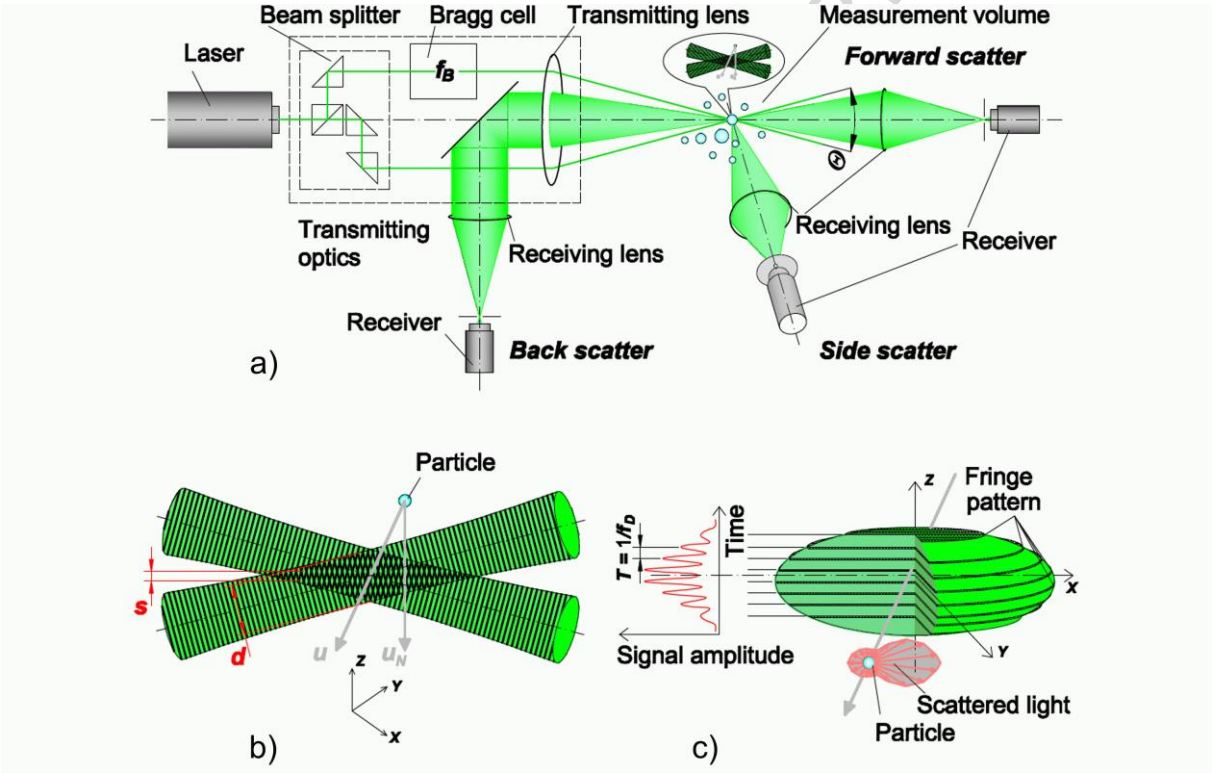

Fig. 2. The LDA principle: a) the optical configuration in the forward, side and backscatter mode, b) fringe pattern with the fringe separation distance s and the Gaussian beam diameter d, c) the "Doppler burst" signal received by the photodetector and the measurement volume with a conceptual cross-sectional cut.

A PDA extends the LDA technique to provide the particle size and velocity simultaneously. This system uses the same transmitting optics as the LDA and a separate receiving optics. The scattered Doppler signals are sensed by at least two detectors. One of them is located in the observation plane, and the other is elevated, at an angle with respect to that plane. The signals collected at different angles show a phase difference $\Delta\varphi$ with respect to each other. This phase shift depends on the particle diameter, D_p, and is a function of the scattering direction and the difference in elevation angles between the detectors. It may also depend on the particle/fluid refractive index, n_p, and fluctuations may be seen in the size diagram, caused by partial wave resonances. Using the "fringe model" gives a simple relationship between the diameter and the measured phase shift:

$$\Delta\varphi = \frac{2\pi D_p n_p}{\Lambda}\Phi\,. \qquad (2)$$

The parameter Φ depends on the scattering mode and the PDA configuration (detailed by (Albrecht, 2003). The measured bursts are sent to a signal processor which extracts the velocity, transit and arrival time, and size data.

The main advantages of the LDA/PDA systems are:

- high spatial and temporal resolution of the fluid/particle flow measurements, with on-line evaluation of single to three velocity components simultaneously,
- the sampled data enables estimation of instantaneous and time-averaged local fluid velocity and TI, and other quantities such as Reynolds stresses or particle path lines can be derived,
- non-contact measurement at a distance of centimetres to metres at an affordable price,
- highly accurate flow measurements with directional sensitivity, suitable for complex unsteady reversal flows with turbulent, transitionary and laminar characteristics, as seen in the airways,
- the PDA adds the particle sizing capability with a spatial and temporal resolution that is not available with any other sizing technique,
- the measurement is absolute, linear with velocity and size (see Eqs. 1 and 2) and does not require a system pre-calibration.

The main drawbacks of the LDA/PDA are:

- the LDA and in particular the PDA cover numerous complex physical processes and require a wide interdisciplinary insight to be operated successfully,
- the optical access required to the measurement space limits these methods for *in vitro* experiments, and introduces issues related to refractive index variations in the complex optical systems,
- it is a slow scanning technique, traversing a point matrix to provide planar or volumetric information (see Fig. 3c), and as a point-wise method, it lacks spatial coherency of the signal so only time-averaged, ensemble-averaged or phase-locked flow fields can be resolved,
- it is an indirect measurement technique, since it measures the velocity of inhomogeneities in the flow, typically tracer particles, that must be carefully chosen to provide sufficient tracking capability (see chapter 3.2.2).

3.2.4. Processing of LD/PD data

LD/PD anemometers provide comparatively high spatial and temporal resolution of velocity and size data (where appropriate) in particle–air flows, making these single-particle counting instruments suitable for estimation of the moments and spectra of turbulent velocity fluctuations and analysis of the particle/fluid dynamics. For illustrative results of time-resolved flow velocity and frequency spectra in a single-point and for flow fields see Fig. 3.

Estimation of velocity moments

Fluid tracer-based methods face two inherent problems when providing statistical analysis of the measured data; velocity bias and the random arrival of tracing particles to the measurement volume. The velocity bias is a problem when calculating simple statistics, such as mean and RMS values, while the random sampling complicates the estimation of quantities that depend on the event timing, such as spectrum and correlation functions.

If one considers a statistically uniform particle distribution in space with mean concentration *c*, and convective velocity *u*, the mean sampling rate is $\dot{n} \propto cSu$, where *S* is the area of the measurement volume projected in the flow direction. The sampling rate is proportional to the particle velocity (see Fig. 3b) and therefore the sampling process is not independent of the event being sampled (McLaughlin and Tiederman, 1973). An application of the arithmetic average to the velocity samples will bias the results in favour of the higher velocities. Several methods were proposed to treat this so-called velocity bias. The signal processors can use a "dead time" feature, when they process only the first Doppler burst that appears during a time window which is set equal to $2\tau_I$, where τ_I is the integral time-scale of the flow. This filtering of the data results in a low data rate, so it is often favoured to instead use a method that utilises a weighting factor f_w, to estimate arithmetical means of the respective flow parameters, e.g. the mean velocity, the second moment and the joint moment (Albrecht, 2003):

$$\bar{u} = \sum_{i=1}^{N} f_{w,i}\, u_i / \sum_{i=1}^{N} f_{w,i}, \tag{3}$$

$$\sigma_u^2 = \sum_{i=1}^{N} f_{w,i} (u_i - \bar{u})^2 / \sum_{i=1}^{N} f_{w,i}, \tag{4}$$

$$\overline{u'v'} = \sum_{i=1}^{N} f_{w,i} (u_i - \bar{u})(v_i - \bar{v}) \Big/ \sum_{i=1}^{N} f_{w,i}. \tag{5}$$

McLaughlin and Tiederman (1973) suggested the use of inverted magnitude of velocity vectors as the weighting factor. An equivalent, and more readily available, weighting factor is the transit time $f_{w,i} = t_{Ti}$ of each particle while passing through the LDA measurement volume.

Estimation of power spectral density (PSD) of velocity fluctuations

Particles dispersed in a fluid appear randomly in space, and hence tracer-based methods are associated with irregular particle arrival times. Presuming a statistically uniform particle distribution in space with a constant convective velocity and mean data rate of the measurement $\dot{n}$, the intervals between the particles, Δt_p, are distributed exponentially: $p(\Delta t_p) = \dot{n} \cdot \exp(-\dot{n}\Delta t_p)$. The probability of inter-particle arrival time increases with a reduction in Δt_p so that data can contain information about very high-frequency fluctuations. Nevertheless, the maximum reliable frequency is $f_{\max} \cong \dot{n}/2\pi$ according to Adrian and Yao (1987). The non-equidistant sampling intervals due to naturally seeded particles in the flow inhibit a direct application of the fast Fourier transform for the estimation of the PSD of the velocity fluctuations, and other methods must be applied. The most reliable spectral estimation techniques developed to address this problem are explained in detail by Benedict et al. (2000). For an example of conversion of the PDA velocity data from temporal to the frequency domain see Fig. 3a and the results in Jedelsky at al. (2012).

The velocity time series allows the calculation of two-time statistics such as correlation and covariance. Integral time-scales can be estimated by use of the auto covariance function.

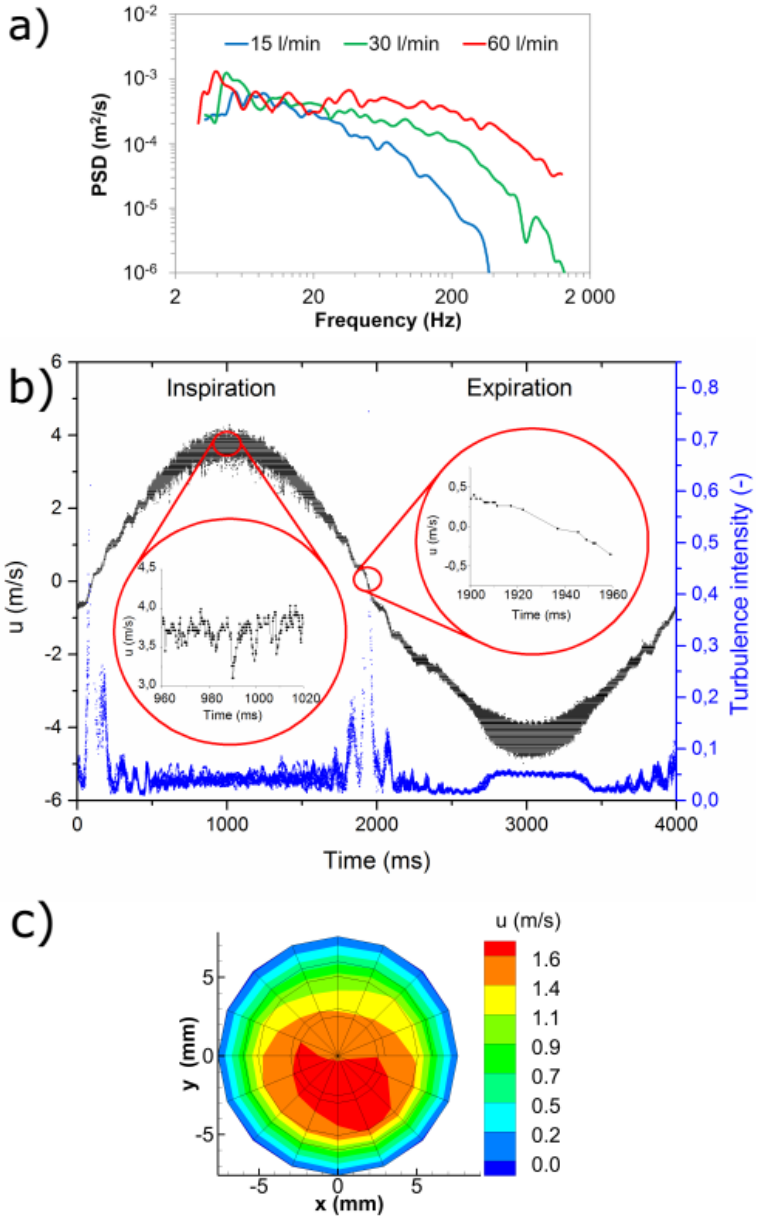

Fig. 3. a) An example of PSD of the velocity fluctuations of air flow in the centre line of the trachea, with different inspiratory flow rates, tracing 4 μm particles. b) A PDA record of air flow velocity during sinusoidal controlled breathing (TV = 0.5 l, breathing period 4 s) with ten overlapped (phase-averaged) cycles. Time intervals with the laminar and turbulent character of the flow are visible. Zoomed windows document irregularly sampled data and the velocity bias effect. c) Mean axial velocity in a cross section in the trachea for steady inspiration, 30 l/min.

Particle sizing

The droplet size dataset provided by the PDA instrument determines a particle number distribution as the primary distribution function[6]. Weight or volumetric distributions are derived quantities. It is convenient to work, not with the entire size distribution, but with mean diameters whose general definition is:

[6] It is in contrast with other sizing instruments, e.g. with laser diffraction technique, which measures the size distribution by volume (Fdida et al. 2010; Robart, D., Breuer, S., Reckers, W., Kneer, R., 2001. Assessment of pulsed gasoline fuel sprays by means of qualitative and quantitative laser-based diagnostic methods. Part Part Syst Char 18, 179-189..

$$D_{qr} = \sqrt[q-r]{\sum_{i=1}^{N} D_i^q \Big/ \sum_{i=1}^{N} D_i^r}\,. \tag{6}$$

Then, for example, D_{10} stands for arithmetic or number mean diameter, D_{32} for volume/surface mean (also called the Sauter mean) diameter. The PDA-based size data must be interpreted with care as the particle size is optically measured while the aerodynamic diameter is mostly used in aerosol flow studies.

Other single-point statistics

The joint particle velocity, diameter and transit time data provided by PDA offer a potential for separation and filtering according to the size or velocity classes. Their mutual correlations and calculation of other derived quantities further characterize two-phase flow systems. Several methods were published (Aisa et al., 2002; Bachalo et al., 1988) to calculate the local particle number concentration and mass/volume flux data. Their estimations, however, face several difficulties and a system calibration, together with sophisticated corrections, is required to obtain bias-free results (Calvo et al., 2009; Dullenkopf et al., 1998; Roisman and Tropea, 2001; Widmann et al., 2001).

Important turbulence characteristics (TI, Reynolds normal and shear stresses, turbulent kinetic energy) can be calculated with multi-component velocity measurements as indicated in Eqs. (3 to 5). Various methods were developed for analysis of point-wise data of the dispersed two-phase flows. Of interest, for lung flow dynamics, can be the ideal spray theory of Edwards and Marx (Edwards and Marx, 1995; Marx et al., 1994) which is based on the droplet arrival statistics and allows for droplet clustering and flow steadiness analysis. The droplet collision phenomena can be studied according to the classic kinetic theory of gases (Santolaya et al., 2013).

3.2.5. The cost and availability of LD instrumentation

The instrumentation costs depend on the system specification, robustness, measurement capabilities, extensibility and variability of the configuration. The cost ranges from approximately 40,000 €/channel for a basic system to more than 80,000 €/channel for a state-of-the-art, well-equipped system. One channel allows for a measurement of one single velocity component, and a PDA system requires an additional channel for particle sizing. Mitchell et al. (2011) report that PD systems are generally more than 60,000 US$/unit and their cost depends on the number of detector units, as well as the sophistication of the data processing equipment. The LD methods are utilised widely for fluid mechanic experiments and such instruments are routinely used in high-tech laboratories today.

3.2.6. Measurement precision and uncertainties

LD-based techniques face some experimental uncertainties associated with the instrument's optics, lasers, and electronics that require attention. The main factors affecting the measurement accuracy are: (1) the geometrical alignment and quality of the optical parts including the crucial effect of the crossing laser beams and the optical properties of the airway model (discussed in chapter 3.2.1), (2) the flow scales with respect to the measurement volume dimensions (see note 3 in chapter 2.2.1), (3) the optical and electronic noise of the photodetectors and other parts of the signal chain and the time response of the system, (4) the flow tracking capability and light scattering properties of the tracer

particles[7] (discussed in chapter 3.2.2) and (5) the system capabilities for the Doppler burst signal processing for particles randomly dispersed in the flow.

The measured size and velocity data are converted into discrete intervals with a finite resolution. This *discretisation error* was quantified as 0.25% for velocity measurements by PDA, (Roth, 1995). Urbán et al. (2017) reported the typical discretisation error for velocity and size measured with the newer Doppler burst spectral analysis technique as 0.002% and 0.08% respectively.

Negus and Drain (1982) documented that the LDA can measure the particle velocity in the range from 1 to 200 m/s in 2D or 3D with a typical accuracy of 1%. Bovendeerd et al. (1987) estimated an error for axial (secondary) velocities in a 90° bend of the circular cross section of 1% (5%) for these velocities with 95% probability intervals.

The PDA applies a linear relation between particle size and the phase difference on bursts that are measured by the photodetectors (see Eq. 2). The linearity assumption, based on the geometric optical theory, is precise for particles greater than a few wavelengths, but does not adequately describe the optical effects on small particles where Mie scattering theory has to be considered. (Sankar et al., 1991) reported a sizing uncertainty of ±0.4 µm for particles below 5 µm and scattering angle 60°. Similar results were published by (Taylor et al., 1994). The detection and processing limit of the PDA is ~0.5 µm and the quoted accuracy is 4% according to (Prokop et al., 1995). Liu (2000) and Tropea et al. (2007) refer the sizing capability of PDA to the 0.5–3000 µm and 1–1000 µm range respectively. We refer the reader to (Albrecht, 2003) for a comprehensive accuracy analysis and guidelines for the design of LDA/PDA systems.

PDA cannot correctly size non-spherical or heterogeneous particles. It is not an issue for liquid aerosols of inhalable size but it is a problem for irregularly shaped i.e. porous, fibrous or crystalline solid particles where other sizing methods must be used.

Further uncertainty might come from the inaccuracy of the model positioning relative to the LDA measurement volume. Elcner (2016) estimated the uncertainty of the measurement probe positioning to be ±0.3 mm. Corieri and Riethmüller (1989) reported a positioning accuracy in three directions of 0.1 mm.

3.2.7. Citations of relevant works

Girardin et al. (1983) used LDV to determine the pointwise velocity of water droplets suspended in air flowing through a nasal model made from a cadaver cast for a flow rate of 166 ml/s. They studied different cross sections of the nasal fossa and showed the influence of shapes and dimensions as well as flow direction on velocity fields. The flow was generally turbulent; the turbinates provided a streamlining effect on the velocity while the liminal valve had a directional effect.

Bovendeerd et al. (1987) measured steady axial and secondary flow velocities in a 90° bend of circular cross section with LDV. They explained in detail the development of the complete flow field.

One of the first LD measurements, targeted to lung flow, was provided by Corieri and Riethmüller (1989) with glycerine and highly idealized glass bifurcation model. They built the Y shape model to a scale of 40, respecting the ratio of diameters and the angles corresponding to generation 12 to 17 and shown the availability and accuracy of LDV to measure the flow in the bifurcating model.

Zhao and Lieber (Zhao and Lieber, 1994a, b) conducted multiple experiments, using a two velocity component LDA in a symmetric single bifurcation airway model of analytically known geometry with aqueous glycerine mixture to simulate flow in the upper human central airways. They measured axial and secondary velocity profiles over the range Re = 518–2089 both for steady inspiratory and expiratory flow. The results showed that in the junction plane, velocity profiles in the daughter

[7] Some principal difficulties appear with the PDA measurement of large particles - particles with diameter exceeding about one third of the diameter of the measurement volume. As inhalable particles do not reach that size, these problems are not discussed here.

branches are skewed towards the inner walls. The inspiratory flow formed “m” shaped velocity profiles in the transverse plane. The biconcave velocity profile also appeared during the inspiratory flow in the parent tube, just downstream of the flow divider, but this rapidly transformed into a velocity peak. These authors (Lieber and Zhao, 1998) later found for oscillatory flow conditions, with a peak of Re 700, 1278, and 2077, that a quasi-steady flow assumption is valid for oscillatory flow for only about 50% of the period. So, quasi-steady equivalents cannot be used to analyse the complexity of flows during the transition between the respiratory phases.

Also, Peattie and Schwarz (1998) used a symmetrically bifurcating tube model. They investigated oscillatory flow using hydrogen bubbles visualization and quantitative pointwise LDV velocity measurements. They measured the secondary velocities (the velocities perpendicular to the axial velocity) under both low and high-frequency ventilation conditions. They pointed out significant differences that developed in the flow properties. At low frequency, the axial velocity field was found to approximate that of a steady flow through a bifurcation. However, even at $\alpha = 3$ only, secondary velocity fields were confined to within a few diameters of the bifurcation.

Ramuzat et al. (Ramuzat et al., 1998; Ramuzat and Riethmuller, 1997) investigated steady and oscillating flows by means of the laser measurement techniques in a two-dimensional (2D) lung bifurcation model and realised later (Ramuzat and Riethmuller, 2002) that the 2D configuration does not represent the complex 3D flow structures, which exist in bifurcating airways.

Tanaka et al. (1999) studied the spatial and temporal variation of secondary flow during a high-frequency sinusoidal oscillating flow with $3.8 < \alpha < 7.5$. They measured using the two-colour LDV technique on an idealized three-generational asymmetrical Horsefield airway geometry materialised from acrylic plastic. They found the secondary velocity magnitudes and the deflection of axial velocity dependent on the branching angle and curvature ratio of each bifurcation and also on the shape of the path formed by the branch cascade.

Farag et al. (2000) investigated axial and secondary velocity profiles in a large-scale Perspex model using LDV. The experiments were conducted with steady inspiratory air flow seeded with salt particles at Re = 1500 and the simple bifurcating 70° symmetrical bifurcation model with 1/7 curvature ratio which mimicked the morphometry of small human airways. They observed a rapid development of strong secondary flows consisting of two main vortices, with two smaller secondary vortex motions toward the inner wall of curvature. The calculated vorticity transport showed the interaction between the viscous force at the boundary layer along the carinal surface and centrifugal force of curvature with further consequences.

Corcoran and Chigier (2000), in one of the ever most cited papers on PDA experiments in lungs, studied the axial velocity and TI contours in the tracheal section of a cadaver-based larynx–trachea model. Measurements were conducted on a model formed by a polyurethane casting of a human larynx and a round glass tube with an inside diameter chosen to match the cadaver tracheal diameter. They assessed the effects of the laryngeal jet on inhalation air flow patterns for steady state flow at three Re numbers (1250, 1700, and 2800) and noted significant reverse flows with high levels of axial TI in the anterior trachea downstream of the larynx for all three flow cases, indicating the potential for turbulent deposition at positions further downstream. Consequently, Corcoran and Chigier (2002) in a similar way studied the axial velocity and axial TI patterns at two different steady inhalation flow rates (18.1 and 41.1 l/min) and qualitatively, using fluorescent dye assessed aerosol deposition in the model. They compared regions with high TI and deposition regions and noted no correspondence between these regions. Gemci et al. (2002) followed with a study of an inhalation aerosol–air flow numerically using the CFD and experimentally with PDA in a simplified throat model (a triangular orifice with a shape similar to that of the glottal lumen contained within a glass cylinder). The authors showed several significant spray deposition mechanisms that were notable in both the experimental and the numerical results.

DeHaan (2002), in his thesis, focused on the enhancement of aerosol deposition in the mouth–throat region by non-ballistic pharmaceutical aerosol devices. He performed *in vitro* tests and CFD in an idealized mouth and throat geometry in a healthy adult male using monodisperse aerosols entering

through various inlets. He used LDV for velocity measurements at the entrance and inside the oral cavity and PDA for particle sizing in front of the model.

Lizal et al. (2012) developed a realistic model of the human upper airways (HUA), which consisted of the throat, trachea and tracheobronchial tree up to the fourth generation. They fabricated the physical model from a transparent silicone and used a sinusoidal breathing pattern with a tidal volume of 0.5 l and a period of 4 s for 1-component PDA measurements of the air–particle flow during full inspiration/expiration breathing cycle in comparison with CFD calculations. Good agreement was found between the experimental and computational velocity courses. Jedelsky et al. (2012) continued with the PDA measurements in the same model, aiming to compare differences in the PSD of velocity fluctuations among (1) steady-flow regimes and equivalent cyclic regimes, (2) inspiration and expiration breathing phase and (3) particle sizes in the size range 1–8 μm. Systematically higher velocity fluctuations in the upper part of the frequency range (30–500 Hz) were found for cyclic flows in comparison with the steady flows. Both the steady and cyclic expiratory flows produced more high-frequency fluctuations than the inspiratory flow. Later Elcner et al. (2016) presented new CFD simulations on the same model in comparison with the previous PDA experiments in eight cross sections in the trachea and the left and right bronchi. They used a full inspiration/expiration breathing cycle with tidal volumes 0.5 and 1 l and the cycle duration of 4 s (sedentary regime and a deep breath). The Reynolds-averaged Navier–Stokes (RANS) simulation agreed with the experiments in almost all the sections and showed unstable local flow structures. The RANS was proven to be a quantitatively acceptable solution for the time-averaged flow field.

Liu et al. (2016) adopted the LDA to measure the airflow velocity profiles in the HUA model for testifying the reliability of LES approach. The study was done under continuous inspiration and expiration with varied respiratory intensities in a realistic HUA based on the medical CT-scan images of a Chinese male patient, the 3D anatomically accurate HUA model including an obstruction resulting from pharyngeal collapse. The LDA velocity profiles and values were almost the same as calculated in the entire measurable region, which identified the LES method as suitable to study airflow dynamics in the obstructed HUA model.

Kerekes et al. (2016) built an idealized 3D human airway model consisting of the trachea and the first five bronchi generations. They used a custom built LDA to obtain velocity profiles in the central airway region for validation of a CFD model they developed. The airway geometry was reproduced from transparent glass tubes, and the LDA measured the axial velocity of monodisperse polystyrene latex particles under an air flow rate of 30 l/min. A high correlation was found between the velocity profiles obtained with the two methods. The results showed the flow to be laminar in the trachea but affected by the airway geometry in subsequent airways.

The PDA is also often applied as a rapid and space-resolved research-based instrument for size/velocity measurements of nebulizer sprays (Kippax et al., 2004; Roth et al., 2003; Stapleton et al., 2000).

3.3. Planar and volumetric flow visualization techniques

While LDA provides only pointwise flow information, PIV and Particle Tracking Velocimetry (PTV) enables us to measure the 3D flow field. Depending on the specific technique, very high spatial and temporal resolution can be achieved.

3.3.1. Planar PIV

For planar PIV, the seeding particles that represent the flow (compare chapter 3.2.2) are typically illuminated by laser light where the laser beam is now widened to a light sheet. In general, two short

light pulses with a distinctive time delay are emitted and two images of the illuminated flow are captured by a camera. A typical PIV set-up is shown in Fig. 4.

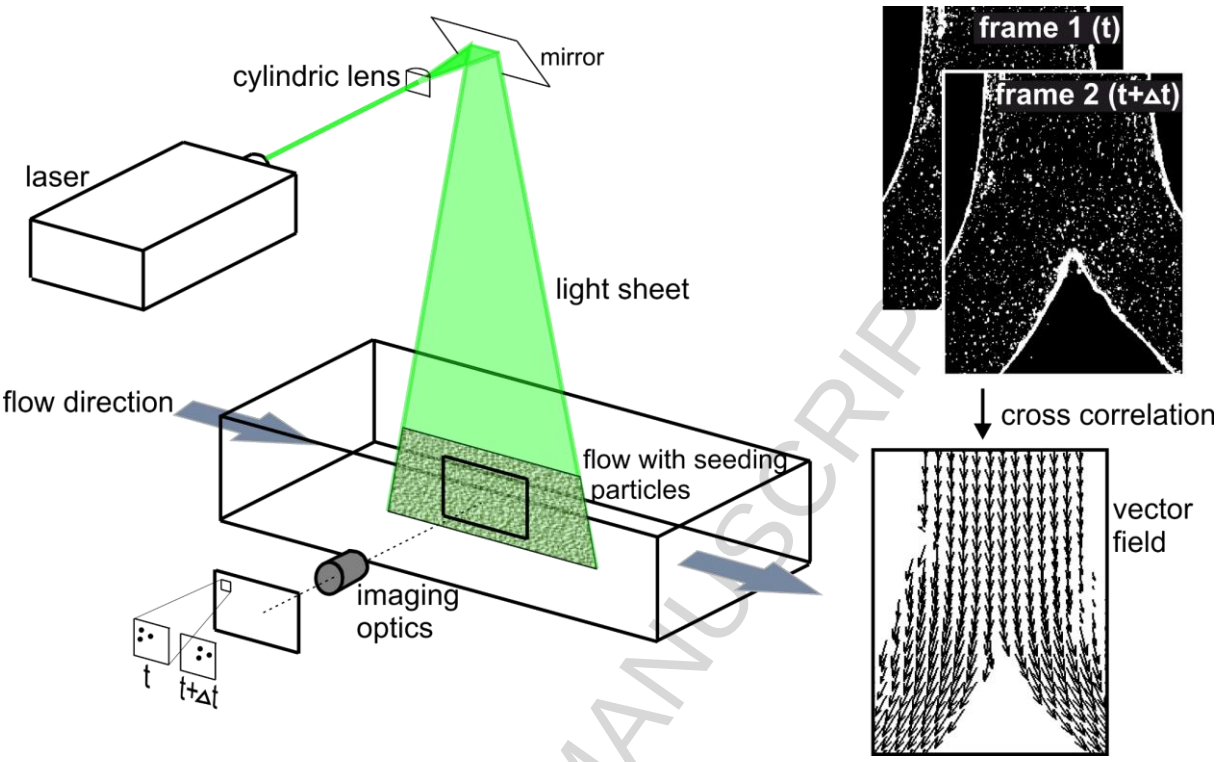

Fig. 4. Typical PIV set-up for planar PIV.

Within this delay Δt between the two images, particles will have moved by a certain distance. In order to evaluate the corresponding particle shift, images are subdivided into small interrogation windows that contain a certain number of particles forming a distinctive pattern. The size of the interrogation windows depends on the particle density in the flow. The higher the density, the smaller the size of the interrogation window can be, since each window needs to contain at least 6 particles in order to determine particle displacement with sufficient statistical accuracy. In contrast, the window size needs to be small enough since each vector represents an averaged velocity within the corresponding interrogation window. Thus, regions with large velocity gradients, e.g. near wall regions, need to be subdivided into small interrogation windows in order to resolve the boundary layer adequately. Typical interrogation windows sizes are 16 × 16 or 32 × 32 pixels with particle densities of about 0.1 particles per pixel (ppp) (Scarano, 2013).

The acquired particle image patterns from two subsequent images are compared by cross correlation. Thereby, a shift in each of the x- and y-directions is calculated forming a displacement vector. By applying the time delay between the images, a velocity vector can be determined for each interrogation window, thus forming a 2D-2C (two-dimensional, two-component) velocity field. An example for planar PIV measurements in the upper bronchial tree is presented in Fig. 5. Here, arrows denote the velocity vector and the velocity magnitude is shown with a colour code.

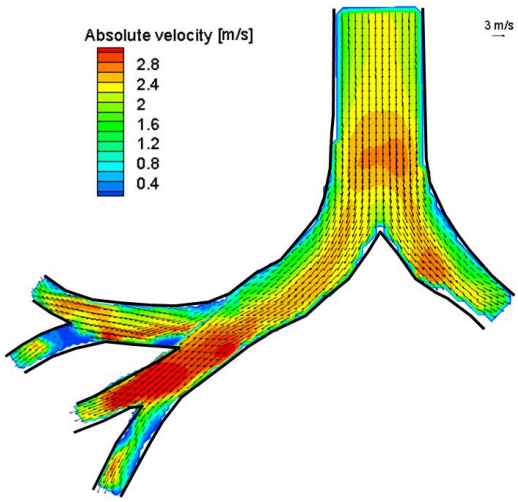

Fig. 5. Velocity vectors and magnitude received from PIV in the upper bronchial tree during inspiration.

The particle shift between two subsequent images should be in the range of about ¼ of the interrogation window size. Assuming a 32 × 32 pixel window, the shift should be about 8 pixels. If the particle shift is too large, i.e. the time delay between two subsequent images too large, the particle images cannot be adequately correlated by cross correlation leading to spurious vectors. In addition, unsteady flow features may be neglected by this kind of averaging. Furthermore, especially applicable to the human lung, in highly 3D flows particles might leave the light sheet plane in the time between two subsequent images and are thus missing in the cross correlation. If instead, the time delay between the images is too short, the distance travelled by particles may be under-sampled, not representative of the flow and/or zero velocity may be determined.

By analogy with LDA special care needs to be taken to match the refractive index of the lung model and the flow. Thus, PIV in realistic human lung models by using air as a medium is not possible. As mentioned in section 3.2.1 a mixture of water/glycerine is used instead and typical flow parameters are adapted in order to maintain flow similarity.

3.3.2. Stereoscopic PIV

The method of stereo PIV allows measurement of all three velocity components, all within one measurement plane. Hence, this method is known as 2D-3C technique. Typically, two cameras focus from different viewing angles on the same plane in order to measure the out of plane component more accurately. A parallel camera arrangement (called “translation” (Adrian and Westerweel, 2011)) is also employed. The advantage of the translational configuration is the uniform magnification of the images, which is not the case for angular positioning. Here, remapping of the distorted image data on a Cartesian grid is necessary. The translation set-up provides constant magnification, avoiding image correction issues, but the viewing angle is limited. As a result, the angular configuration is most frequently used. In the case of measurements in liquids, the change of the refractive index when light passes through different media must be corrected. This is either realized with liquid-filled prisms fixed at outer walls or alternatively, surrounding walls are positioned in an octagonal configuration (see Fig. 6) in order to receive the optical axis of the camera normal to the viewing window. Scheimpflug adapters need to be implemented in order to correct the focal plane.

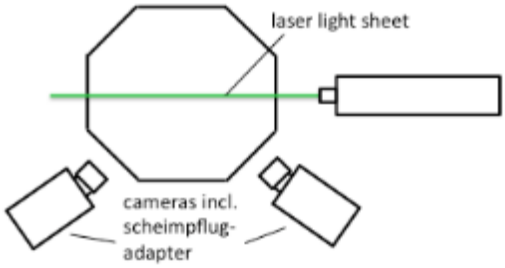

Fig. 6. Camera set-up with octagonal tank walls for stereo PIV or volumetric PIV.

Special care needs to be taken during the measurements to receive high levels of accuracy since otherwise, errors in reconstruction of the 3D displacement vector will occur. This is even more critical for measurements in turbulent flows where velocity fluctuations can be small (Adrian and Westerweel, 2011).

3.3.3. Volumetric PIV

In order to capture a 3D-3C velocity field at least three cameras have to capture an image of the flow from different viewing angles while the domain is illuminated volumetrically. Consequently, volumetric PIV is substantially more complex than planar PIV, since the 3D particle distribution of the viewing domain needs to be reconstructed from the planar images of each camera. A greater number of cameras reduce the reconstruction uncertainty. The 3D-3C PIV method is also known as Tomo-PIV since tomographic image reconstruction methods are employed.

Accurate calibration of the field of view captured by the cameras is most important. Reconstruction deviations in the sub-pixel range of less than 0.2 pixels are required for adequate cross correlation evaluation. Wieneke (2008) introduced the volume self-calibration that needs to be applied at every measurement in order to reduce the calibration errors.

Accuracy problems additionally occur due to spuriously reconstructed particles, so called ghost particles at high particle densities. Thus, the particle density for volumetric PIV cannot be as high as for planar PIV, typically values of 0.05 ppp need to be applied (Elsinga et al., 2006). But this value also depends on the number of cameras being used.

The problem of ghost particles can be circumvented by an advanced PTV technique where the motion of single particles is tracked, so that particle path lines that include local velocities can be reconstructed. Thereby, the history of the particle traces is employed to estimate the exact particle position in the subsequent time step. To determine particle positions in a new time step, an educated prediction of the new position is made and refined by an image matching scheme (Schanz et al., 2013). Hence, higher particle densities (up to 0.125 ppp) can be used than for 3D PIV. Additionally, computational time is strongly decreased since only single particle tracks need to be considered and not the whole voxel volume of a Tomo-PIV algorithm (Schanz et al., 2014).

Advantages of PIV/PTV

- 2D and 3D information of the whole flow field can be obtained simultaneously
- nonintrusive measurement method - no flow disturbances
- High spatial and temporal resolution possible, depending on camera and light source

Disadvantages of PIV/PTV

- Refractive index matching is required
- Use of small particles often requires use of high-intensity light sources (class 4 lasers)
- Expensive measurement method
- Reduced quality of results in high shear flows

- Tracer particles must follow the flow without slip and should have the same density as the fluid, hence only very small/light particles can be used in air

Applications of planar, 2D PIV measurements

Due to their experimental simplicity, 2D PIV measurements have frequently been applied in the upper and lower airways. Earliest measurements have been carried out by (Brücker, 1998) at a planar double bifurcation based on Weibel's (Weibel, 1963) statistical dichotomic lung model, but with rectangular cross section, thus avoiding image deformations due to deviations of the refractive index. Brücker's work covers steady inspiratory flow for a Re range from 900 to 2700 which represents flow conditions in large airways from the trachea down to the 5th generation (Brücker, 1998). The authors observe cyclic oscillations of flow patterns and a strong influence from upstream generation flows in the downstream generations, which might not occur in more realistic geometries with a round cross section of airway branches.

More recently, Ramuzat and Riethmuller (2002) applied planar PIV measurements in a double bifurcation model with round cross branch sections. They investigated the variation of velocity profiles for oscillatory flow during one breathing cycle. Breathing parameters include normal and High Frequency Oscillatory Ventilation (HFOV) while varying Re from 400 to 1000. Moreover, during post processing, they analysed the spatial displacement of various selected points near the outer walls and the carina after one cycle. The net motion thus denotes steady streaming indicating a bidirectional streaming direction between near wall and central locations. In contrast, points very close to the carina hardly show any net displacement. Hence, they associated these zones with higher deposition rates.

A rather exceptional PIV method was applied by Heenan et al. (2003) to measure mean and turbulence RMS velocities. They applied endoscopic PIV in an oropharynx model that allowed flow measurements in air since the camera view was not obstructed by any sidewalls that might alter the refractive index. Their method only required optical access for the laser light source from outside the model. Nevertheless, their field of view was limited by the size and position of the endoscope. The endoscope furthermore had a wide-angle view leading to image distortions that needed correction. Additionally, the surface of focus was not planar, leading to out of focus areas in the image. Hence, the uncertainty for the PIV analysis was increased. Despite the challenges and difficulties of the endoscopic imaging technique, these measurements were well suited as a validation technique for CFD modelling.

PIV measurements at more complex representations of the human airways have been carried out in the following years by Adler and Brucker (2007) and Grosse et al. (2007). Both groups used a 3D lung model made from transparent silicone. Their geometry started with the trachea and bifurcated down to the 6th daughter generation. While Grosse et al. (2007) used a geometry based on a CT scan, Adler and Brucker (2007) developed a generic geometry based on statistical data from Horsfield and Cumming (1968) and Weibel (1963). Both groups used oscillatory flow according to typical breathing scenarios, and time-resolved PIV measurements were applied to investigate the flow patterns in selected planes of the model geometry. Grosse et al. (2007) additionally applied steady flow conditions under varying Re from 1250 to 1700 and stated that the influence of the Re was relatively low. On the other hand, they emphasized the strong influence of α, i.e. oscillatory flow conditions which strongly altered the flow structures during the breathing cycle. Adler and Brucker (2007) additionally investigated the influence of varying α for breathing under rest conditions as well as HFOV. In contrast to Grosse et al. (2007), their results reveal the low influence that varying α has on flow patterns, especially at peak flow conditions. Fig. 7 depicts PIV results for varying breathing parameters representing breathing under rest conditions. Colour coded is here the vorticity distribution indicating local shear rates.

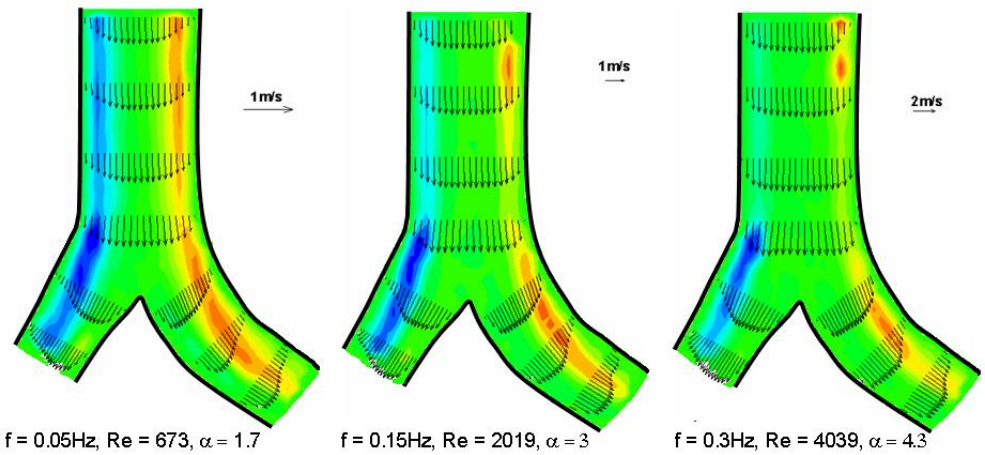

Fig. 7. Velocity vectors and normalized vorticity during peak inspiration for different breathing parameters (with permission reprinted from (Adler and Brucker, 2007)).

Following this, Fresconi and Prasad (2007) carried out a systematic study on secondary velocity profiles in a symmetric planar bifurcation model incorporating three bifurcating generations. They applied steady inspiratory and expiratory as well as oscillatory flow conditions and varied the Re in a low range from 6 to 200. Based on the measurements they could identify the critical Re and Dean numbers at which secondary flows start to develop in the human airways.

Application of stereo-scanning PIV in the airways

Soodt et al. (2013) applied stereo-scanning PIV measurements at the lung model already described in Grosse et al. (2007). The technique allows fully 3C-3D measurements. In addition to the stereoscopic set-up, the authors applied a moving (scanning) light sheet which was generated by a rotating mirror drum driven by a stepper motor. The principle was first described by Brücker (1996). Thereby, the whole measurement domain is scanned by a moving light sheet so that one whole scan can illuminate several adjacent planes simultaneously, i.e. the time span between the first and the last plane is small enough to prevent large particle motion. A new full scan can be regarded as the second set of images, necessary for cross correlation. Limiting factors are the rotation speed of the stepper motor for the mirror drum and the camera frame rate for image acquisition. Modern high-speed cameras work at typical frame rates of 6000 frames per second (fps) or even up to 20,000 fps at a full resolution of about 1 Megapixel. With a frame rate of 6000 fps, only those flows with velocities below 1 m/s can be investigated. Hence, realistic flows in the upper airways cannot be investigated by using scanning PIV. The maximum Re that Soodt et al. (2013) employed in their stereo scanning study was 150 at oscillatory conditions, a value which is more than a factor of 10 below realistic Re numbers in the upper airways.

A further restriction of scanning PIV measurements is the requirement for lenses with a large focal depth, so that they can provide constant magnification at a range of lens-to-object distances in order to avoid correlation uncertainties. Thus, so called telecentric lenses need to be employed.

Applications of volumetric measurements

As a result of improvements in evaluation techniques and equipment, volumetric measurement techniques have been employed only recently in the human lungs. (Banko et al., 2015) carried out magnetic resonance[8] velocimetry (MRV) measurements in a CT based replica of an airway geometry

[8] Please refer to chapter 5.2 for description of principles of magnetic resonance.

from the mouth down to the 8th bifurcating generation fabricated by stereolithography. Flow patterns were visualized by a 3 Tesla General Electric whole-body scanner (Banko et al., 2015). The technique thus does not require optical access and refractive index matching to the measurement domain. The authors used water as a working fluid in a translucent model, generated by 3D printing techniques. The MRV did not allow time-resolved measurements due to large scanning times of 45 min. Results show a fully 3D Eulerian velocity field with a resolution of 0.7 mm in each direction, yielding a similar resolution as PIV measurements in geometries of the same size. In an ongoing study, Banko et al. (2016) investigated oscillatory flow by applying phase-locked measurements. Nemes et al. (2016) used MRV in an idealized planar and symmetric lung model for the systematic study of how the Re influences the development of secondary flows, especially in the transitional regime. They found that after the onset of turbulence, secondary flow intensity started to decrease after reaching a maximum in the still laminar regime.

3D particle path lines have been visualized by Janke and Bauer (2016), see Fig. 8. The measurement technique is based on 3D particle tracking velocimetry (3D-PTV) yielding direct visualization of 3D patterns in the human airways. Janke and Bauer (2016) used high-power light emitting diodes instead of a laser as the light source and three high-speed cameras for image acquisition. Particle tracking was applied by employing a Shake-the-Box algorithm according to Schanz et al. (2013). The method helped to reduce particle reconstruction ambiguities.

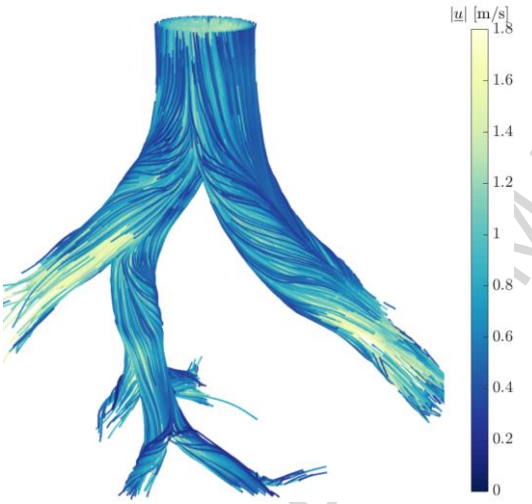

Fig. 8. Particle trajectories received from 3D-PTV during the peak inspiration phase. Trajectories are colour coded by the velocity magnitude (Janke and Bauer, 2016).

Micro PIV Measurements

So far, we have only considered flow measurements in the large, conductive airways. Flow in the bronchioles and alveolar region can be captured by micro PIV measurements. Flow channels are usually made from PDMS (Polydimenthylsiloxane) and have typical dimensions in the range of 500 µm. Due to the small FOV microscopic imaging needs to be employed. A very simple representation was presented by Lee et al. (2006). They investigated Pendelluft flow during HFOV conditions at a single bifurcation model by implementing compliant boundary conditions.

Fishler et al. (2013) developed more complex models in order to mimic pulmonary acinar flows. Their PDMS models are still planar but contain bronchial branches spanning five generations with alveolar sacs. Via a syringe pump, they applied oscillatory flow within the domain. As a working fluid Fishler et al. (2013) also used a mixture of water and glycerin. Yielded flow velocities were in the range of a few µm/s to mm/s. Their model was capable of featuring typical alveolar flow patterns including recirculations. In a further study, Fishler et al. (2015) used airflow added by particles in order to investigate particle transport and deposition under realistic flow conditions. Their model geometry

was improved with walls that could move in a similar way to alveoli. Recently, Fishler et al. (2017) investigated particle dispersion mechanisms in the alveolar ducts by single particle tracking. They observed an irreversible net motion of particles, which they attributed to streamline crossing.

4. Classical methods for the measurement of total and regional aerosol deposition

The following chapter represents a conservative choice of common methods that are used to measure total or regional aerosol deposition. Some of these methods offer measurements of local deposition when applied in airway replicas. Although they normally provide lower resolution than some of the emerging methods, they are still popular as a result of their availability, and in many cases, low price.

4.1. Measurements of inhalation and exhalation concentrations using particle counters, spectrometers or photometers

One of the simplest methods for measuring aerosol deposition works by capturing the concentration of aerosol entering the airways during inhalation and the concentration exiting the airways during exhalation, and calculating the difference. The method can be applied both *in vivo* and in replicas (in a simplified manner). Using the basic setup, either overall lung deposition or nasal airway (Kesavanathan and Swift, 1998) deposition can be measured *in vivo*. The usual experimental setup includes a source of (preferably monodisperse) particles, an in-line aerosol concentration measuring instrument (e.g. laser aerosol photometer (Kim and Kang, 1997)), to be positioned as close as possible to the mouth piece, a flow rate measurement device, and a set of valves allowing the intake to switch between clean air and aerosol during inhalation, and between inhaled and exhaled air-aerosol mixtures, with as little cross sectional changes as possible between these components. The experiment can be performed in the following way: the volunteer inhales a well-characterized monodisperse aerosol out of an aerosol generator or holding chamber through a mouthpiece, and then exhales. The concentration of particles and the actual flow rate are measured in-line during the whole in- and exhalation. The total deposited fraction can then be calculated as TDF = (average C_{in} × inhaled volume – average C_{out} × exhaled volume) / (average C_{in} × inhaled volume). This can be done in a single or a multiple breath manoeuvre. Either total or nasal deposition can be calculated from the non-bolus method, whereas deposition and dispersion at various lung depths can be derived from the bolus method.

An interesting variation of this method is the so-called aerosol bolus method. It can be applied *in vivo* and in replicas and the main idea of this approach is that the aerosol is not delivered throughout the entire inhalation, but in smaller volumes (typically 20–300 ml) inserted at various time points in the inhalation. By delivering the aerosol bolus followed by a progressively larger volume of inhaled air, the aerosol bolus can be pushed deeper into the lungs. Upon recovery of the aerosol bolus during exhalation, one can determine local aerosol deposition at various lung depths (Kim et al., 1996). While sometimes referred to as regional lung delivery, this specifically refers to the aerosol being delivered to more proximal or more peripheral lung regions. On its way through the lungs, the bolus will inevitably split between an increasing number of parallel pathways that may affect aerosol transport in a different way. This is the key to the aerosol bolus being used as a diagnostic tool, whereby the dispersion of the aerosol bolus is considered a measure of convective gas mixing, which can be greatly altered in lung disease (Blanchard, 1996). While aerosol bolus deposition measurement requires a mono-dispersed aerosol, aerosol bolus dispersion is less affected by aerosol particle size and meaningful aerosol bolus dispersion data can even be obtained with a saline aerosol (Verbanck et al., 2001a; Verbanck et al., 2001b). The (monodisperse) aerosol bolus deposition has also been used as a

diagnostic tool, for instance, to estimate the size of widened air spaces in the deep lung in patients with emphysema (Kohlhaufl et al., 1998); in that case the aerosol derived airway diameter is an average measure of airway size for a given lung depth.

The main benefits of both the bolus and non-bolus methods are: relevance of the data — since these measures can be obtained *in vivo*, no radioactive substance needs to be inhaled, and the latex particles or oil droplets that will guarantee mono-disperse aerosols can be inhaled in very low concentrations and still be reliably detected (for deposition measurement). With this, however, come several issues, the main one the repeatability of experiments: repeatability is limited by the ability of subjects to reproduce the same breathing pattern, and in the case of bolus experiments, the accuracy of the setup in injecting the small aerosol volumes at a specific time point in the inhalation; as a result, repeated experiments are needed on the same subject to obtain reliable data. The other issue that is particularly relevant for comparison with CFD-derived 3D flow fields and aerosol trajectories is that aerosol concentration measurements with a photometer typically cover the middle 75% of the tube cross section, and intrinsically produce just an average concentration value for a given tube cross section.

Advantages:

- no radioactivity involved,
- no simplification of the reality,
- can provide diagnostic indices.

Disadvantages:

- complicated control of boundary conditions (to be temporarily stable and inter and intra-subject invariable),
- difficulty with obtaining the geometry and boundary conditions for CFD.

Examples of application — *in vivo* and in replica

As measuring the concentration of inhaled and exhaled particles is a relatively straightforward procedure, it was used as one of the first methods to assess the total deposited fraction. The pioneering works in this area have been reviewed by Lippmann et al. (1980). The first measurements were done by Landahl in the 1950s (Landahl et al., 1951), who collected the exhaled triphenyl phosphate particles using an impactor, washed the samples out using alcohol and estimated the quantity colourimetrically. Many studies followed, however sometimes performed under poorly controlled conditions, rendering the comparison of results difficult. In fact, Lippmann suggested that the data collected by Heyder et al. (1978) could serve as the lower limit of aerosol deposition, since their experiments were well controlled and indeed reported the lowest deposition, compared to other total deposition studies.

The aerosol bolus method was applied by several teams *in vivo* (Altshuler, 1969; Darquenne et al., 1998; Kim et al., 1996; Scheuch, 1994) and also in a canine lung cast (Scheuch et al., 1993). Because of the substantial differences among existing aerosol bolus results in the literature, experimental sources of error in the bolus method were examined by (Verbanck et al., 1999). These authors showed how differences in the bolus deposition of up to 25% can arise in the same normal subject as a result of the aerosol delivery and measurement system. Depending on the tubing system and how developed the velocity profile of the aerosol bolus is upon entering the lungs, the photometer measurement will produce an aerosol concentration curve that is not representative of the average concentration over the entire tube cross section. Since the inspiratory quantity of aerosol (average C_{in} × inhaled volume) serves as a reference for the TDF computation, an inaccurate estimate of the inhaled concentration

profile will lead to TDF errors; in the case of proximal boluses, undergoing very little deposition, this artefact can lead to the paradoxical result that TDF becomes negative.

4.2. Microscopy

Optical microscopy has been used mainly to count and analyse fibres. As we are not discussing invasive techniques, only those experiments performed in replicas of human lungs will be described. The method is very simple in principle. The fibres are dispersed, usually using a fluidized bed generator, treated to equalize the electric charge and mixed with inspiratory air. Then the fibres enter the model of lungs with coated walls, where a certain fraction deposits. The rest of the fibres are then collected on output filters. The fibres deposited in the model are consequently either counted directly *in situ* using the microscope (Myojo, 1987, 1990), or washed out, filtrated, and counted on the filter (Belka et al., 2016).

Several variants of microscopy are available currently. The first established method was the Phase Contrast Microscopy (PCM). This method was developed for detection of samples that are optically transparent and therefore are invisible to an observer with a basic optical microscope, because the human eye is sensitive only to changes in intensity of the light, which is not attenuated by passing through the transparent sample. Since the phase of the passing light is shifted, these phase changes can be converted to an observable intensity change using e.g. Zernike's method (Zernike, 1942).

The PCM method was utilized and standardized for counting of asbestos and other fibres as part of NIOSH 7400 (NIOSH, 1994), WHO (WHO, 1997) or ISO 8672 methodology for occupational protection and toxicology. Other variants of microscopy, such as the Transmission Electron Microscopy (TEM) or Scanning Electron Microscopy (SEM) (Baron, 2001), can be used in principle for the analysis of deposited fibres, however, these methods are mainly being used in toxicological studies and have not obtained popularity comparable with PCM for non-invasive particle deposition studies.

Analysis performed by microscopy provides data in the form of a number of particles (usually fibres) deposited in either whole replica, or separate segments commonly containing one bifurcation.

Examples of application

PCM has been applied by several teams in replicas of human airways. Deposition of carbon fibres in nasal replica was measured by Su and Cheng (2005). They found that deposition of fibres is generally lower compared to equivalent spherical particles. A year later they performed a follow-up study focused on the deposition of particles in oral airways and part of the tracheobronchial tree (Su and Cheng, 2006). They proved that low inertia fibres can easily penetrate through the first four generations of bronchial branching and deposit in the lowest regions of lungs. As a next step, comparison of fibre deposition in two realistic replicas was performed by (Zhou et al., 2007). Although they observed a large variability among bifurcations from the same generation when comparing the two replicas, they stated that general trends could be drawn from their study: fibre deposition in the tracheobronchial tree is lower than that of the equivalent spherical particles. The authors also emphasized the need to use a realistic airway model, including larynx, for plausible simulation of flow patterns in the airways. Lastly, the same team added TiO_2 and glass fibres to get very low momentum fibres (Su et al., 2008). Their results confirmed an overall continuity between fibre materials. The equations used to estimate a fibre's regional deposition efficiency in the human respiratory airways were devised based on this experimental data. The numbers of fibres in samples from all the above-mentioned studies were counted manually using adapted NIOSH 7400 methodology. A similar approach was used also by (Wang et al., 2008) for the analysis of nasal deposition of fibres. Because the manual counting of fibres is demanding and subjective, due to the human factor involved in the analysis, attempts were made to develop an automated counting methodology based on image

analysis techniques. Such a technique was presented e.g. by (Belka et al., 2016). Their method was tested against the standard manual method and proved to be consistent with the results obtained by a trained human operator, while avoiding those factors that contribute to subjectivity such as mood, fatigue or the health state of the PCM operator. However, only high-quality filters free of impurities can be evaluated using the automated algorithm (Fig. 9).

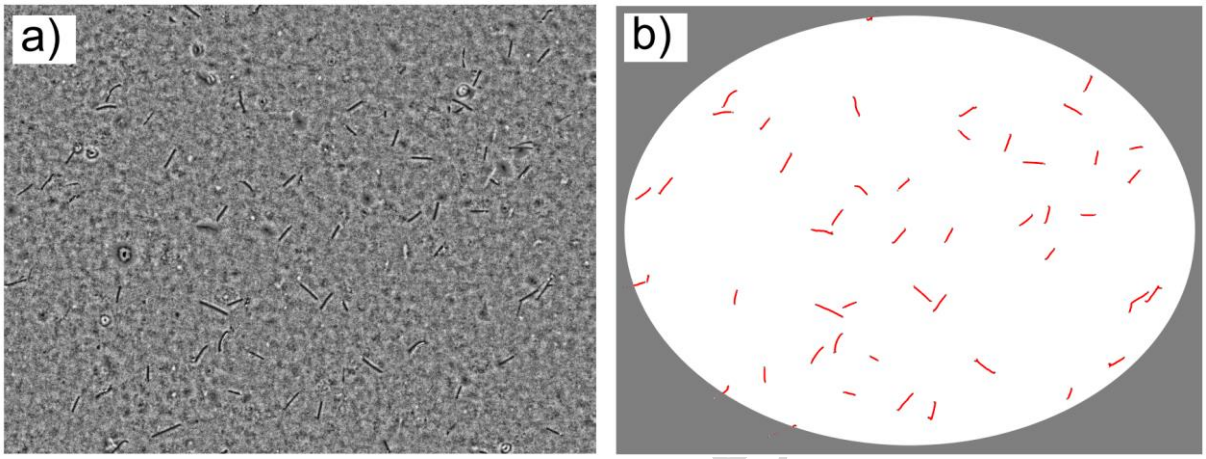

Fig. 9. Example of an automated fiber detection method applied on glass fibers deposited on a nitrocellulose filter: a) a processed image with fibers enhanced by a special algorithm, b) automatically detected fibers in the identical image.

Uncertainties:

Both manual and automated counting provide data with relatively high uncertainties. The precision of the manual counting using PCM for the determination of airborne fibre number concentrations was discussed by WHO (1997). The coefficient of variation (CV) in the number of counted fibres depends on the density of fibres on the filter. Microscopists generally tend to under-count dense samples and over-count sparse samples. The recommended density range for optimal accuracy is between 100 and 1000 fibre/mm^2. The intra-laboratory CV is in the range of 21 to 49% depending on the number of counted fibres. However, inter-laboratory CV can be twice as great as intra-laboratory CV. These values are acceptable in occupational protection measurements as the counts of particles are evaluated in orders of magnitude, nonetheless, the usability of this method for validation of CFD results is limited. Automated counting can decrease the CV, however, values below 20% can hardly be expected. Therefore, only confirmation of general trends can be provided, while comparing the exact counts in specific segments of lungs is questionable.

Advantages:

- simple and relatively cheap method,
- no radioactivity needed,
- can provide diagnostic indices.

Disadvantages:

- relatively high uncertainty,
- time-consuming,
- applicable only on replicas.

4.3. Gravimetry and Fluorometry

The term gravimetry refers to a method based on weighing filters or collecting plates that contain deposited aerosol particles. This method is commonly used with cascade impactors, but can be generally used for the analysis of samples washed out from lung replicas. The term fluorometry refers to those methods that are based on fluorescence measurements on the samples collected by washing out the segments of airways. Both methods are routinely used in many laboratories as standard methods in many disciplines. Their application in deposition studies usually employs replicas of lungs. The most common setup consists of the particle generator or disperser, a charge equilibrator, an aerosol-air mixer, a replica of lungs with connected output filters and a vacuum pump. Then, for gravimetry, either the whole replica or its parts are washed out, the resulting dispersion is filtrated and the filters analysed. This requires filters that are insensitive to temperature and humidity changes, and are not easily electrically charged. The samples for fluorometric analysis are created directly by washing out the model. The particles must be dissolved using a suitable solvent. A second set of samples is created from the output filters, while the material of the filters is commonly dissolved to provide a pure sample. Procedures similar to fluorometry can also serve for other common chemical methods, such as Gas Chromatography – Mass Spectrometry (GC–MS). GC–MS is suitable for analysis of multicomponent particles (Nordlund et al., 2017).

Type of data provided:

Mass or particle number distribution in the replica and output filters.

Examples of application

The gravimetrical analysis was applied e.g. by (Grgic et al., 2004) or (Zhang and Finlay, 2005), who measured deposition in three idealized proximal lung bifurcation models with an idealized mouth–throat. They revealed the important role of the laryngeal jet on tracheal deposition, and that its effect in the following bifurcations was negligible. Fluorometry was applied e.g. by (Kim and Iglesias, 1989) and more recently (Cheng et al., 2015), who used sodium-fluorescein-tagged oleic acid particles. Solid polystyrene latex fluorescent particles in the size range of 0.93 to 30 μm were used by (Cheng et al., 1999). As a proof that fluorescence based methods can be used *in vivo*, we present the study of (Bowes and Swift, 1989), who (apart from using ^{99m}Tc tagged particles) let their volunteers inhale fluorescence tagged di-ethylhexyl sebacate particles. After the inhalation, the subjects gargled to remove the deposited fluorescent tracer from the oral airway and the solution was analysed. The study focused on the sensitivity of the filtration efficiency of the oral airway to different levels of physical activity. Somewhat surprisingly the deposition efficiency was lower during heavy exercise than during moderate exercise, although the inhalation flow rates increased. The explanation was that because the mouth was opened more widely, the cross-sectional area of the oral airway probably resulted in decreased particle velocities and hence lower inertia of particles.

Uncertainty:

For gravimetry, an analytical balance with a resolution about 0.1 mg is needed. It is necessary to select suitable filters that do not absorb humidity and keep them in well-controlled conditions. The uncertainty of results is usually expressed only as the standard deviation of measured values, which is typically around 5%. The advantage of fluorometry can be seen in higher sensitivity, providing the suitable tracer is used.

Advantages:

- simple and relatively cheap methods,
- both routinely used in many laboratories.

Disadvantages:

- low spatial resolution (especially for gravimetry).

5. Standard medical imaging methods

A relatively wide database of experimental results describing aerosol deposition has come from standard medical imaging modalities. The main advantage of this group of methods is that the instrumentation is broadly available in hospitals and specialized centres and the methods are routinely used in clinical practice. The results are acquired mainly *in vivo*, although several applications in lung replicas have been reported as well. The crucial issue for a successful nuclear measurement is proper labelling of the aerosol particles. The tracer can be either directly chemically incorporated into the molecule of the particle material, attached to the surface of the particle or physically embedded into the volume of the particle. In any case, proper labelling is necessary to ensure that the signal received from the tracer truly represents the distribution of particles.

5.1. Nuclear imaging methods

Nuclear imaging techniques, which comprise Positron Emission Tomography (PET), Single Photon Emission Computed Tomography (SPECT) and planar gamma-camera imaging or 2D-scintigraphy, are *in vivo* and minimally invasive imaging modalities which allow the determination of the spatiotemporal distribution of a radiolabelled tracer (radiotracer) after administration into a living organism. Gamma ray-emitters or positron emitters (which ultimately result in the emission of gamma rays, see below) are suitable radioisotopes for this purpose, as high-energy gamma rays can travel through biological tissues without suffering significant scatter or attenuation. Such gamma rays can be detected and quantified using specific instrumentation and tomographic reconstruction algorithms.

It should be noted that although the nuclear imaging was developed for *in vivo* measurements, successful attempts have also been made *in vitro* as documented e.g. by Lizal et al. (2015) or Verbanck et al. (2016).

5.1.1. The basis of nuclear imaging: radioactivity, radioactive isotopes and radiotracers

When the nucleus of an atom has an excess of energy, it undergoes a spontaneous and stochastic process called radioactive decay. In this process, the nucleus reaches a lower-energy state while emitting radiation in the form of alpha particles, beta particles (electrons or positrons), gamma rays or conversion electrons. The emission type, the level of transition energy and the lifetime of the radionuclide before decaying are characteristic for each radionuclide.

Radioactive decay is a stochastic process in which the probability of an atom to undergo radioactive decay is constant over time. The radioactive decay formula is expressed as:

$$N(t) = N_0 e^{-\lambda t}\,, \tag{7}$$

where N_0 is the initial number of radioactive atoms, $N(t)$ is the number of radioactive atoms at time = t, λ is the decay constant (ln2 / $T_{1/2}$). $T_{1/2}$ is the half-life of the radioisotope, and corresponds to the period of time required to decrease the number of radioactive atoms to one half of the starting value. In the International System of Units (SI) the activity is expressed in Becquerel (Bq), 1 Bq corresponding to one disintegration per second. Curies (Ci) are also commonly employed, with 1 Ci = 37 GBq.

Radioactive isotopes are usually administered after attachment or incorporation into a molecule (radiotracer). During recent decades, many radiochemical strategies have been developed that enable the radiolabelling of a wide range of molecular formats including small molecules, peptides, proteins, antibodies, affibodies and nanoparticles (NPs) using a wide range of positron and gamma emitters. For some reviews, refer to (Gillings, 2013; Li and Conti, 2010; Miller et al., 2008; Morais et al., 2012; Pratt et al., 2016; Price and Orvig, 2014; Stockhofe et al., 2014).

5.1.2. SPECT

SPECT relies on the detection of gamma rays originated during radioactive decay of single photon-emitting radionuclides. Single-photon emitters commonly used in nuclear imaging have half-lives ranging from a few hours to a few days and photon energies in the range 100–300 keV. Among single photon emitters, metastable technetium-99 (^{99m}Tc) is the most commonly used, with nearly 80% of nuclear medicine imaging procedures currently performed with this radionuclide: It has a favourable gamma-energy (141 keV), a suitable half-life of 6.02 h, and well-known coordination chemistry. Additionally, it can easily be obtained as $^{99m}TcO_4$ in an aqueous buffer from commercially available ^{99}Mo/^{99m}Tc generators. Other widely used gamma emitters include ^{123}I ($T_{1/2}$ = 13.22 h, E = 159 keV), ^{111}In ($T_{1/2}$ = 2.8 d, E = 171 and 245 keV) and ^{67}Ga ($T_{1/2}$ = 3.26 d, E = 93, 185, 300, and 394 keV).

SPECT scanners consist of at least one gamma-ray detection module and one collimator. The core of the detection module is normally a scintillation crystal which absorbs the energy of incident gamma rays and re-emits a flash of light, which is subsequently detected by a photo-electronic system. Both the location in the crystal and the intensity of the flash of light, which is proportional to the energy of the incidental gamma-ray, are recorded. The collimator most commonly consists of a lead plate containing a large number of holes, which stop all the rays that do not reach the detector in a given direction. Hence, the collimator forms a projected image of the radioisotope distribution on the surface of the scintillation crystal. SPECT systems are typically composed of one or more detection heads which are mounted on a gantry that rotates around the imaged subject. If only one set of static detectors is used, the imaging modality is referred to as planar gamma-camera imaging or 2D-scintigraphy (Fig. 10).

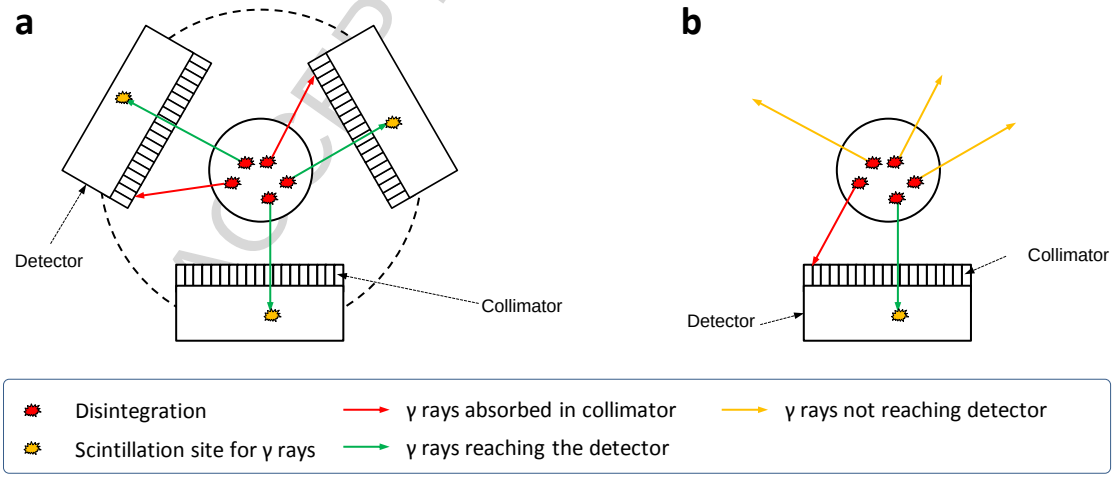

Fig. 10. Schematic representation of the detection of photons using SPECT (a) or planar gamma-camera imaging (b). Only a fraction of the emitted gamma rays reaches the detectors, while others are absorbed in the collimator or never reach the detectors.

5.1.3. PET

The positron is the antiparticle of the electron, with equivalent mass but positive electrical charge. When a positron is emitted, it interacts with other charged particles and loses kinetic energy while transiting a random path. When most of this energy has been lost, the positron annihilates with an electron of a surrounding atom, resulting in the emission of a pair of gamma rays travelling in directions 180° apart and each with an energy of 511 keV. The distance between the locations where disintegration and annihilation take place is called positron range, and depends on the energy of the emitted positron and the media. Typical positron emitters have positron ranges of a few mm in water.

The unique feature of gamma rays generated by positron–electron annihilation is exploited by coincidence detectors, which are placed around the subject under investigation. Two photons detected almost simultaneously by two detectors are assumed to arise from one single annihilation. The position of annihilation is determined by tracing a line between the two detectors, and hence PET imaging relies on back-to-back detection heads (coincidence detection). As a result of this, PET scanners do not need collimators: The detection of "pairs of photons" is known as "electronic" collimation. A schematic representation of a PET scanner is shown in Fig. 11.

Positron emitters typically used in the medical or biomedical fields have shorter half-lives than single photon emitters. The most commonly used radionuclides are presented in Table 1.

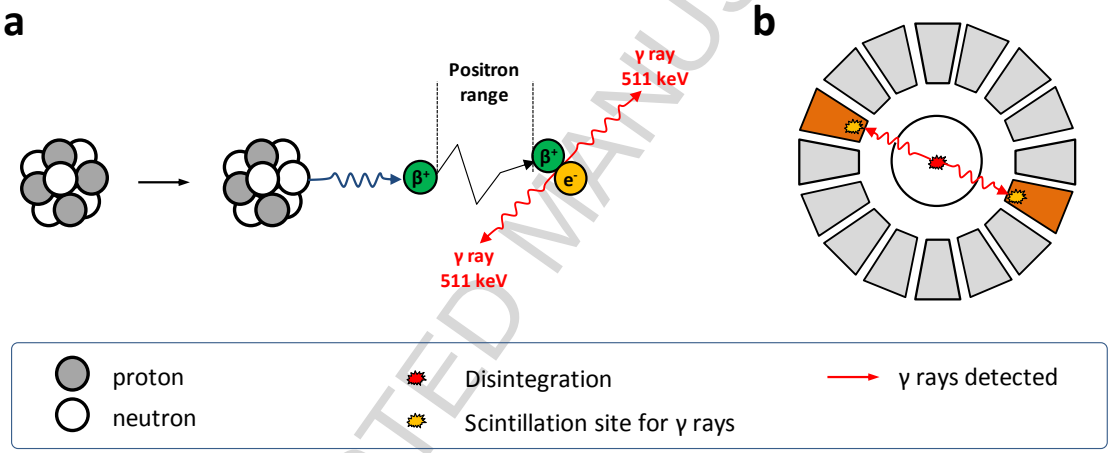

Fig. 11. a) Schematic representation of the annihilation process of one positron and one electron, with subsequent emission of two gamma rays. b) Representation of a PET camera. The two photons emitted after the annihilation process are detected simultaneously by two detectors of the ring, placed around the subject under investigation.

Table 1
Typical positron emitters (with half-life and positron range).

Isotope	Half-life	β^+ Energy
^{18}F	109.8 min	0.63 MeV
^{11}C	20.4 min	0.96 MeV
^{13}N	9.97 min	1.20 MeV
^{15}O	122 s	1.73 MeV
^{68}Ga	67.6 min	1.89 MeV

Both in PET and in SPECT a set of projections at different angular positions around the subject under investigation is acquired. The images are then reconstructed using different algorithms (e.g. Filtered-Back-Projection or FBP, Ordered Subset Expectation Maximization or OSEM) and the resulting images can be analysed to gain quantitative information about the spatiotemporal distribution of the radiotracer.

5.1.4. Nuclear imaging: important remarks

As mentioned above, nuclear imaging techniques offer information on the spatiotemporal distribution of the radionuclide within the organism under investigation. Importantly, the radiotracer is usually injected in a sub-pharmacological amount (trace amount) and hence no pharmacological, adverse or toxicological effects are expected. However, these techniques have certain limitations that are worth mentioning and which need to be taken into consideration.

Lack of anatomical information

Nuclear imaging techniques do not provide any anatomical information of the subject under investigation. Because of this, nuclear imaging techniques are often combined with other imaging modalities which can provide accurate anatomical information, essential to unequivocally determine the location of the radioactivity. CT (3D x-ray imaging) is the most commonly used, and most of PET and SPECT scanners currently available exist only as hybrid systems (PET-CT or SPECT-CT). Besides providing anatomical information, the CT image is also used to create the attenuation map for appropriate correction during image reconstruction (for more details, refer to (Ay and Sarkar, 2007)). In the recent years, hybrid PET-MRI systems have been developed. MRI provides excellent spatial resolution and high contrast in soft tissue. However, determination of the attenuation map is still a challenge and hence this hybrid technology is still not fully established (Paulus and Quick, 2016).

Limited spatial resolution

Contrary to other imaging modalities such as CT or MRI, one of the major limitations of nuclear imaging techniques is the spatial resolution. Preclinical SPECT devices provide high spatial resolution that can reach well below a millimetre, whereas it is very difficult for PET scanners to attain sub-millimetre spatial resolutions, due to the effect of the positron range. On the other hand, PET systems are typically much more sensitive than SPECT cameras as no collimator is required for imaging. In general terms, PET cameras can achieve resolutions in the range of 1 mm in the preclinical setting and around 5 mm in the case of clinical scanners.

Motion effects

One of the major challenges in nuclear imaging is to correct for motion effects. This is especially relevant when imaging the thorax or the abdomen, as the subject's breathing causes artefacts. Many different approaches for artefact avoidance or correction have been developed, most of them based on gated acquisition and synchronization between the respiratory signal and image acquisition. Although routinely performed in routine clinical practice, this approach fails to adequately correct for respiratory motion because each gate can mix several tissue positions. Other correction techniques integrate motion information before, during, or after the reconstruction process. For a recent review, refer to (Pépin et al., 2014).

Quantification of the images

Quantification is the process of deriving meaningful quantitative data from the images. The physical property that is directly measured in nuclear imaging cameras is the concentration or radioactivity. However, the cameras can only detect a small fraction of the gamma rays emitted.

Consequently, it is necessary to calibrate these devices by scanning objects with a known activity concentration and derive a multiplicative calibration factor that will be applied subsequently. Of note, activity concentration values depend on a number of confounding factors which require correction during the quantification process. The most obvious factor is the injected amount of activity (injected dose, ID): the larger the ID, the higher the signal. A common way to correct for this is to express activity concentration values as a percentage of the total injected dose per gram of tissue (%ID/g). The value of %ID/g can be misleading when comparing subjects of different weights, because the total body volume in which the radiotracer distributes also affects the concentration value. To overcome this drawback, the Standard Uptake Values (SUV), calculated as activity concentration / (ID/subject weight), are usually determined. As the activity concentration is normalized by body weight, the resulting SUV of a radiotracer with an even distribution in the whole body would be 1. It is important to take into account that the limited spatial resolution of nuclear imaging techniques poses some limitations in the quantification of the images. When the object or structure that is imaged is smaller than 2–3 times the spatial resolution of the scanner, as measured by its Full Width at Half Maximum (FWHM), activity concentration values obtained after quantification are underestimated (partial volume effect). Reciprocally, the concentration of radioactivity in small regions with low activity surrounded by regions with high concentration of radioactivity can be over-estimated (spill over effect). In this scenario, accurate estimation of the activity concentration requires knowledge about the size of the object and the reconstructed image spatial resolution. There are several possible approaches to correct or minimize the partial volume effect. A detailed description is beyond the scope of this review (Bettinardi et al., 2014).

Stability of the radiotracer

Nuclear imaging cameras detect the position of the radionuclide. Hence, if detachment of the radioisotope or metabolism occurs during imaging studies, the distribution of the *in situ* generated labelled species may significantly differ from that of the parent compound, leading to misinterpretation of the results or a decrease in the signal-to-noise ratio. Hence, a crucial aspect to guarantee reliable data is the stability of the radiotracer once it has been administered to the subject under investigation.

5.1.5. Use of nuclear imaging in the assessment of aerosol distribution in the lungs

Lung administration of drugs has recently gained attention because pulmonary administration offers numerous advantages (Loira-Pastoriza et al., 2014). However, one of the major challenges of lung administration is determining the dose actually deposited in the lungs and the regional distribution of the drug, and these parameters will have an impact on the clinical effect. When the drug is administered in the form of an aerosol, the regional distribution can be determined using nuclear imaging techniques, by just labelling the aerosol (or the drug itself) with a positron or gamma emitter that enables subsequent imaging studies using PET or SPECT/2D-scintigraphy, respectively.

Determination of regional distribution using SPECT/2D-scintigraphy

As mentioned above, ^{99m}Tc can be obtained from commercially available generators, it is reasonably inexpensive, it has a relatively long half-life, close to 6 hours, and has appropriate emission properties. Not surprisingly, it has been one of the most commonly used radionuclides to tackle the determination of regional lung distribution of aerosols in the lung. The most straightforward route to incorporate ^{99m}Tc in the aerosol consists of adding the radionuclide to the nebuliser solution, to achieve a physical association of the label and the drug. However, the chemical form plays an important role. When ^{99m}Tc is added as pertechnetate (as obtained from the generator) its residence time in the lungs

is very short (close to 15 min, (Walker et al., 2001)) and hence long term investigations are not possible. However, information about the regional distribution of the aerosol immediately after administration can be obtained. Other forms of technetium can be used to enable longer-term investigations, such as the complex ^{99m}Tc-DTPA (^{99m}Tc-diethylene triamine penta acetic acid) (Eberl et al., 2001) or a colloidal suspension of albumin (human serum albumin freeze-dried micro colloid) (Fleming et al., 2011). It is important to take into account that images reflect the distribution and clearance of the labelled entity. Hence, differences in the behaviour of the labelled entity with the drug itself may lead to misinterpretation of the results. Additionally, it is important to demonstrate that the radiolabelling process has no effect on the properties of the aerosol in order to get reliable data.

After the acquisition of images, qualitative information can be obtained by visual inspection. To obtain quantitative data, regions of interest (ROIs) or volumes of interest (VOIs) can be delineated on the 2D-scintigraphy or SPECT images, respectively, and the concentration of radioactivity in the region/volume of interest can be determined. However, such delineation is often challenging because the radioactivity does not necessarily distribute in the whole lung. Nowadays, with multimodal (hybrid) systems available in most clinical centres, x-ray or CT scans can be carried out sequentially to the nuclear image acquisition, enabling accurate delineation of the lungs on the x-ray or CT images. The ROIs or VOIs are then translated to the 2D-scintigraphy or SPECT images, respectively, for quantification. In the past, when no hybrid imaging systems were available, delineation of the lungs was carried out with transmission scans using external radioactive sources or from ventilation scans using radiolabelled gases (e.g. ^{81m}Kr) (Newman and Fleming, 2011).

Examples of ^{99m}Tc-labelling to assess deposition of drugs in the lungs can be found both in the context of SPECT and 2D-scintigraphy. For example, Brand *et al*. used 2D-scintigraphy to compare the deposition pattern of ^{99m}Tc-labeled Berodual® (fenoterol hydrobromide 50 µg / ipratropium bromide 20 µg per actuation) in COPD patients using two different inhalers (Respimat® Soft Mist™ Inhaler (SMI) and a pressurized metered-dose inhaler) before and after training the patients on the use of the inhaler (Brand et al., 2008). One of the inhalers (Respimat® SMI) showed superiority in terms of global deposition in the lungs. Additionally, training improved the inhalation profiles (Fig. 12). In another study, Behr *et al.* investigated lung deposition of a liposomal cyclosporine A solution consisting of uni-lamellar 50 nm liposomes in single and double lung transplanted patients using a customized nebulizer and planar scintigraphy (Behr et al., 2009). The authors could quantify total and peripheral lung deposition as a function of the administered dose.

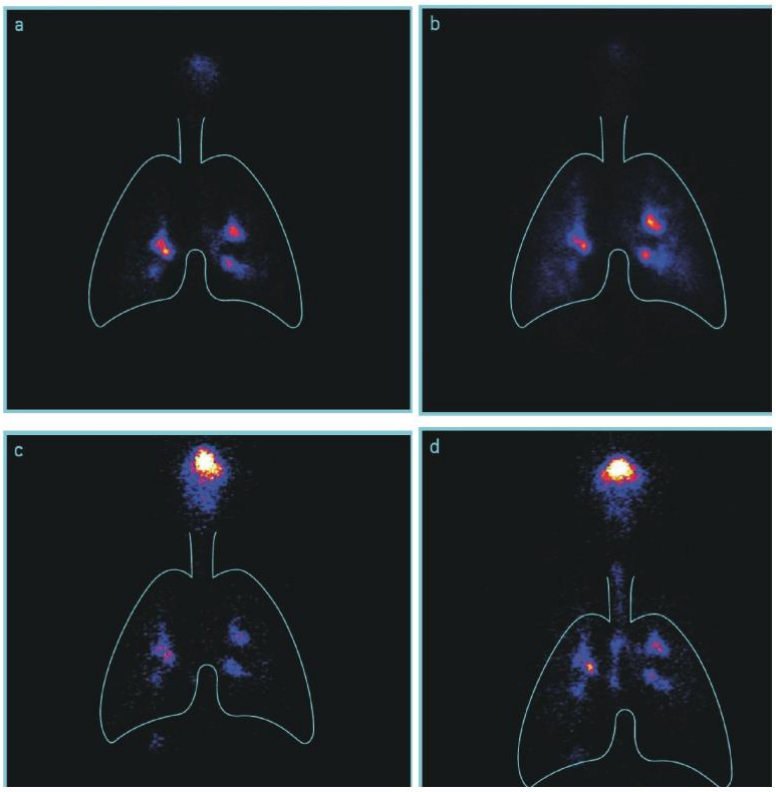

Fig. 12. Samples of scintigraphic images from a patient showing deposition pattern from Respimat® SMI before training (a) and after training (b), and from pressurized metered-dose inhaler before training (c) and after training (d). Reprinted with permission of (Brand et al., 2008).

The main limitation of 2D-scintigraphy relies on the fact that 3D information is condensed in a 2D-image (projection). To overcome this drawback, SPECT imaging can be used. In this modality, volumetric information can be obtained and the images can be displayed as slices in three different views (transverse, coronal and sagittal planes). However, even in this case quantification of the images to get volumetric information about the regional distribution of the aerosol is not trivial. Firstly, most of the gamma emitters used in nuclear medicine have relatively low gamma energy emission (e.g. 141 keV for ^{99m}Tc) and hence attenuation effects have to be taken into account. As mentioned above, this can be easily solved nowadays because CT scans can be obtained using hybrid systems to determine the attenuation map for correction of the SPECT images. Secondly, the relation between the number of gamma rays detected by the detectors and the number of disintegrations taking place depends on many different factors, such as the injected activity, the geometry of the collimator, the energy of the gamma rays, and the geometry and material of the detectors, among others. Hence, appropriate calibration is paramount to achieve absolute quantitative data.

Just to mention one example of the use of SPECT in the determination of aerosol deposition in the lungs, Dugernier *et al*. have compared the total and regional pulmonary deposition of aerosol particles generated by two different nebulizers (a vibrating-mesh nebulizer and a jet nebulizer) in six healthy male subjects (Dugernier et al., 2017). With that aim, nebulizers were filled with ^{99m}Tc-DTPA and pulmonary deposition was measured using SPECT-CT. As demonstrated by the authors, aerosol deposition was six times increased with the vibrating-mesh nebulizer as compared to the jet nebulizer (34.1 ± 6.0% versus 5.2 ± 1.1%, $p < 0.001$) (Fig. 13). However, aerosol penetration (calculated as the normalized ratio of the outer and the inner regions of the lungs) was similar between the two nebulizers.

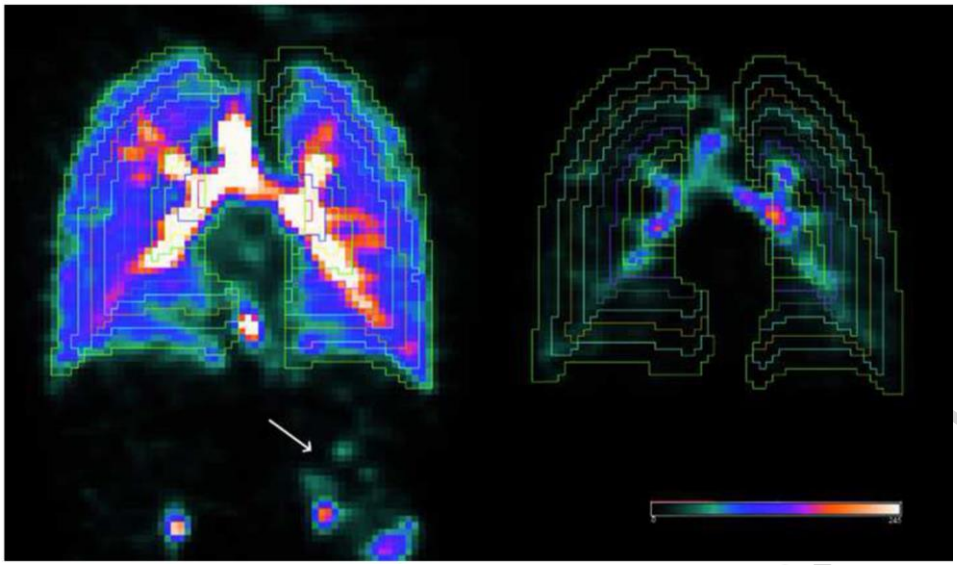

Fig. 13. Shell decomposition of SPECT-CT coronal slices at the level of the right hilum for both nebulizers on the same subject, with the same level of brightness. Both lungs were divided in ten shells (coloured lines through both lungs) distributed from the hilum to the lung periphery. The deposition of the radiolabeled particles of aerosol, depicted in colour, is highly increased with the vibrating-mesh nebulizer with its specific valve-holding chamber in comparison to the constant-output jet nebulizer with a corrugated tube. Activity is seen in the stomach with the vibrating-mesh nebulizer (white arrow). Reprinted from (Dugernier et al., 2017), with permission of Springer.

Examples of the use of SPECT-CT to assess regional lung deposition of aerosols are also found in the pre-clinical setting. For example, Gracia et al. recently reported the synthesis of water-dispersible dextran-based single-chain polymer nanoparticles (SCPNs), which might be used as drug carriers for inhalation. Radiolabeling of these biocompatible NPs with the gamma emitter ^{67}Ga followed by SPECT-CT imaging allowed the longitudinal investigation of lung deposition of the NPs in rats after intratracheal nebulization using the Penn-Century MicroSprayer® (Gracia et al., 2017) (see Fig. 14a). Acquisition of CT images enabled appropriate delineation of the VOIs in the whole lungs (Fig. 14b). In this case, the species of interest (the NPs) and not the aerosol was labelled, and hence the SPECT images reflect the deposition and clearance of the NPs (and not the aerosol). This example is a proof that nuclear imaging can be effectively employed in the determination of drug deposition in the lungs after aerosol administration. Of note, pre-clinical studies in small animals face the main drawback of limited spatial resolution (1 mm in preclinical scanners), which, together with motion effects due to breathing and heart rate, will limit the accurate quantitative determination of regional distribution.

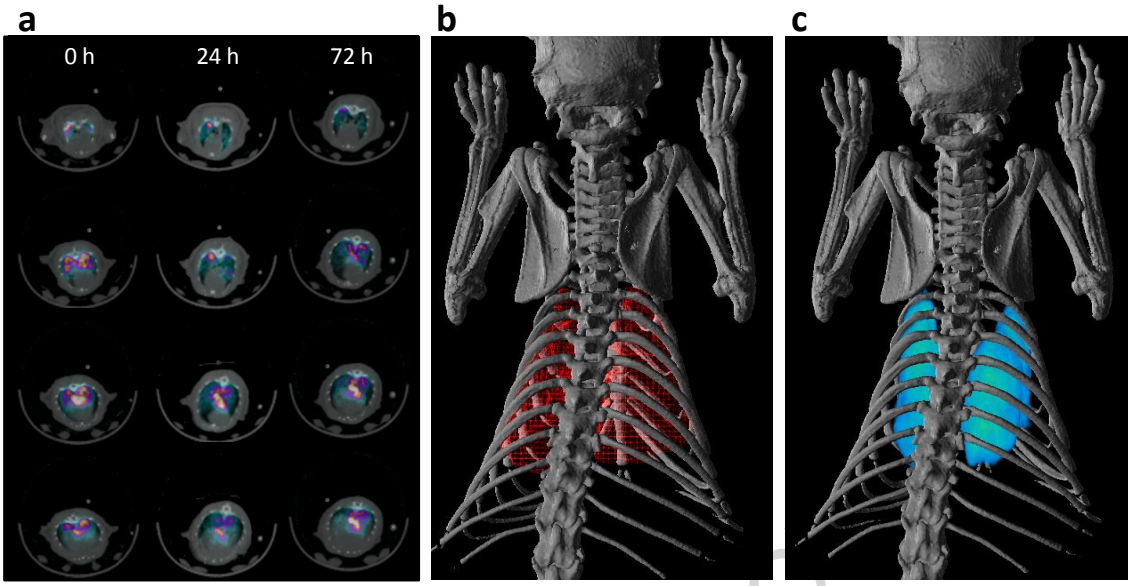

Fig. 14. a) Representative axial slices of SPECT-CT images obtained at t = 0, 24 and 72 hours after administration of ^{67}Ga-labeled particles by intra-tracheal nebulization; SPECT images are co-registered with CT images for easy localization of the radioactivity; b) 3D CT images of the skeleton (grey) co-registered with surface-rendered 3D CT images of the lungs; c) 3D CT images of the skeleton (grey) co-registered with volume-rendered SPECT images of the lungs (green tones).

Determination of regional distribution using PET

PET has higher sensitivity and higher spatiotemporal resolution than SPECT, and absolute quantification of the images is less challenging. Hence, PET is a valuable option to assess lung deposition of aerosols. However, most of the commonly used short-lived positron emitters are cyclotron-produced, and hence their use is restricted to centres with a cyclotron in house.

Due to this limitation, PET studies performed to date to assess lung deposition have been conducted with the well-known indirect proliferation marker 2-deoxy-2-(^{18}F) fluoro-D-glucose ([^{18}F]FDG), which is widely used in the clinical field, with a production/distribution network well established in most developed countries. A nice collection of examples on the use of this radiotracer to evaluate changes in the deposition of inhaled aerosols within the lung, related to the presence of disease or resulting from inhalation challenge interventions or inhaled therapies, has been recently reported (Dolovich, 2009), and one representative example of the work reported there is shown in Fig. 15. In this particular study, 13 patients with asthma and 10 healthy volunteers were challenged with methacholine aerosol and PET images were obtained after inhalation of 1.5 µm aerosol containing [^{18}F]FDG. As it can be seen, quite a uniform distribution was found pre-challenge, although hot spots could be observed in the anterior third of the lung (transaxial view). The images acquired post-challenge show a patchier ventilation scan, with localized areas of tracer deposition throughout the lung.

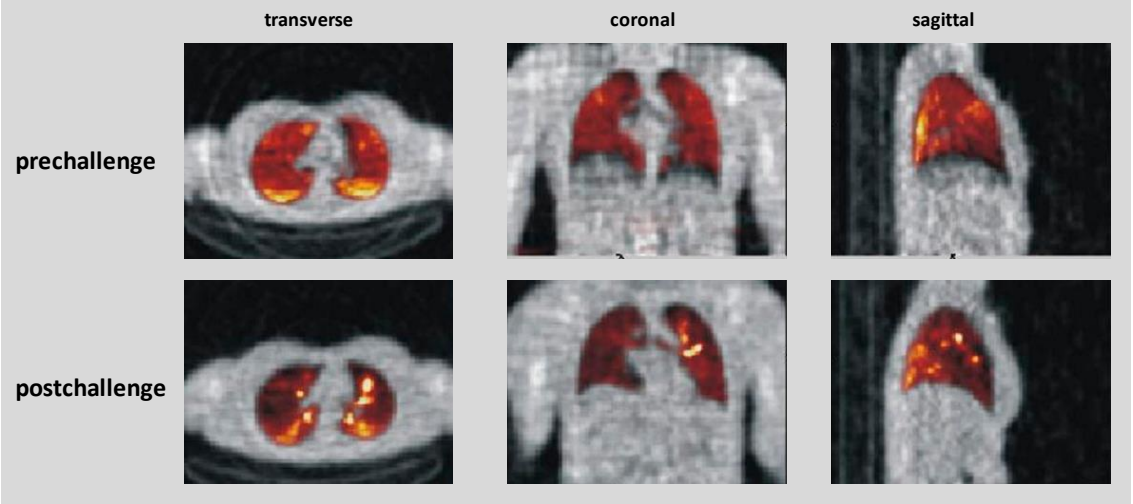

Fig. 15. Images from a PET scan obtained following inhalation of [^{18}F]FDG aerosol in one subject with asthma and immediately after a methacholine challenge. The baseline scan is reasonably uniform with ventilation posterior and basal as seen in the one slice in the transaxial plane. On the repeat scan, hot spots are evident throughout the lung as seen on these single slices from the transaxial, coronal, and sagittal planes. Adapted from (Dolovich, 2009).

Advantages:

- high sensitivity (especially PET),
- images can be acquired at the whole organ or body level,
- quantitative information can be obtained (especially PET).

Disadvantages:

- low spatial resolution, in the order of a few millimetres in the clinical setting,
- low temporal resolution,
- use of ionizing radiation,
- expensive (especially PET), sophisticated equipment and specialized personnel are required.

5.2. Proton MRI for aerosol deposition studies

Conventional MRI is based on the principle that atomic nuclei can absorb and emit electromagnetic energy when manipulated using an external magnetic field. First, a strong magnetic field is applied to align the 'spin' of protons in hydrogen atoms, which are found in water molecules within the body. A radio frequency signal is then used to resonate the atoms, and the relaxation signal is measured by conductive coils placed around the patient. Parameters of the magnetic field pulse sequence can be varied and hence different contrasts can be acquired between various tissues due to the relaxation properties of the hydrogen atoms in different tissues.

Using proton MRI for lung studies is especially challenging due to the low water content of lung parenchyma (about 15%) and the large difference between tissue and air susceptibilities (around 10 magnetic field homogeneity units in parts per million, ppm), which normally results in a low MRI signal that can be a source of a new contrast possibility using susceptibility mapping approaches. The study of aerosol deposition using proton MRI is based in 1) the use of oxygen as paramagnetic contrast agent, 2) the use of chelated Gadolinium (diethylene triamine penta acetic acid, Gd-DTPA, or 1,4,7,10-

tetraazacyclododecane-1,4,7,10-tetraacetic acid, Gd-DOTA) as an inhaled paramagnetic contrast inhaled agent, and 3) the use of ultra-short echo (UTE) time sequences more adapted to lung parenchyma imaging and new applications especially in the paediatric field to reduce respiratory artefacts and deal with the short lung T2* (decay of transverse magnetization caused by combination of spin–spin relaxation time, T2, and magnetic field inhomogeneity). The first two options have the advantage of studying aerosol inhalation based on longitudinal relaxation time (T1, hot spot or positive contrast). In general, paramagnetic agents reduce both the T1 and T2 relaxation times of the water in the lung parenchyma, and thus can be used to quantify the regional delivery of this tracer based on the significant increase in signal intensity with the ventilation of these agents (Sood et al., 2010; Sood et al., 2008). The vast majority of studies have utilized the reduction of T1 times with increasing contrast concentration to detect the agents (Thompson and Finlay, 2012), which area surrogate marker of aerosol deposition of other therapeutic components. The combination of this technology with UTE-MRI data acquisition has proven to provide more accurate concentration measurements (Wang et al., 2016).

Application of MRI in aerosol deposition studies

The results using Gd-DOTA aerosol nebulization with spontaneously breathing rats (see Fig. 16) yielded a homogenous signal enhancement in the lung despite a reduced and less controlled dose (Wang et al., 2016). Still, the protocol was applied with smaller doses of contrast agent to previous results and it is the first quantitative map of aerosol deposition *in vivo* using MRI. For reproducibility, regional distribution in the lungs was analysed using an automatic procedure to divide the lung into equal volume regions. A comparison of regional aerosol distribution images showed significant differences for left versus right, head versus feet and central versus peripheral dependencies (Wang et al., 2016).

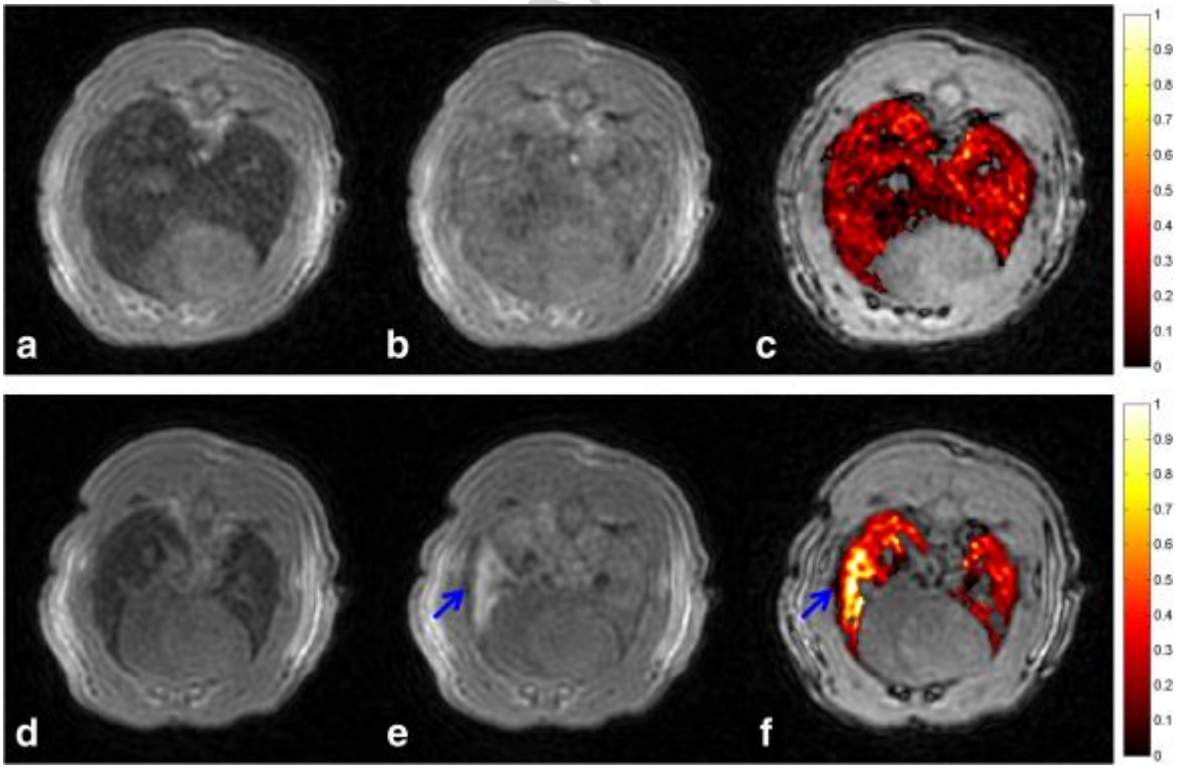

Fig. 16. Aerosol deposition in the lungs of spontaneously breathing rats using Gd- DOTA-based contrast agents and ultra- short echo time MRI at 1.5 Tesla. Reprinted from (Wang et al., 2016) with permission of John Wiley and Sons.

Compared to other T1-weighted MRI applications, this UTE imaging has also the advantage of opening the field to the use of superparamagnetic iron oxide NPs with or without drug loaded in the final preparation to study direct aerosol deposition. Due to the enhanced pulmonary signal intensity, this imaging modality facilitates the real quantification of the tracer using, for instance, parametric transverse relaxivity (R_2*) mapping with two or more echo time datasets, utilising the linear relationship between this parameter and particle concentration (Oakes et al., 2013). In this study, superparamagnetic iron oxide particles were employed to study *ex vivo* regional aerosol deposition on rat lungs nebulized during conventional mechanical ventilation. As expected from previous experiments using radiolabelled particles, deposition was higher in the lung periphery than in the central airways, and no differences were found in the gravitational dependent and independent regions of the lung, such as is known from previous multiple-breath washout experiments in ventilated rats (Verbanck et al., 1991).

As observed in the above-mentioned studies, although the advantages of proton MRI for human application have been described for many applications, proton MRI is still far from clinical applicability (except for pediatric patients with restricted and controlled radiation exposure). Also, besides the described lung MRI problems, studies on aerosol deposition are mainly based on the ability of MRI to trace the surrogate marker and not any other component of the aerosol. If specific compounds are to be traced, the MRI contrast should be incorporated into that compound. The use of aerosolized iron oxide particles compared to oxygen or Gd-based contrast has then the potential to be applied in humans more than any other alternative, especially at low magnetic fields, and facilitates the possibility of integrating these extra compounds in the final formulation. Finally, current approaches require contrast agent doses that are too high to be considered competitive with traditional radionuclide aerosol deposition measurement methods in humans (Thompson and Finlay, 2012).

Advantages:

- No radioactivity (suitable for paediatric patients),
- Both flow velocity and aerosol distribution can be measured.

Disadvantages:

- Trace marker needed,
- Long imaging time (low temporal resolution),
- Low differences in contrast between lung parenchyma and air,
- High doses of contrast agents needed.

6. Emerging methods in aerosol flow and deposition measurements

The rapid development of experimental methods in recent years promises to provide results of a quality and resolution that was inconceivable in the past. Three of the methods (Hyperpolarized gas MRI, Optical Coherence Tomography (OCT) and Phase Contrast X-ray Imaging (PCXI)) are described in detail in this paper. However, several other methods that are not discussed here are also expected to expand our knowledge of the inhaled aerosol flow in the near future. Because of the lack of human imaging with these techniques to date, we break the convention of this review and include animal experiments in this chapter.

There is a large group of methods that can be grouped under the title “intravital microscopy”. These techniques are based on fluorescence light microscopy and their growth is driven by the progress in the non-linear microscopy. Intravital microscopy can be used for dynamic imaging of

cellular and even subcellular structures, which will be especially useful for drug delivery studies. The reader who is interested in this group of methods is referred to the well-written review by (Amornphimoltham et al., 2011). One method that is suitable for the acquisition of airway geometries is multi-planar 3D ultrasound imaging (Or et al., 2013). Its main advantages include a high level of safety for patients and a relatively low price.

As the flow distribution within human airways is of great importance, especially for CFD boundary conditions, it can be expected that Electrical Impedance Tomography (EIT) will gain popularity, serving as a source of such data (Moerer et al., 2011; Riera et al., 2013). EIT is based on measurement of potential differences between electrodes positioned around patient's thorax after the injection of high frequency and low amplitude electrical currents.

Distribution of magnetic nanoparticles with unique spatial and temporal resolution can be measured by Magnetic Particle Imaging (MPI). The method achieved rapid growth after Gleich and Weizenecker (2005) published the principles of the technique. MPI utilizes superparamagnetic iron oxide nanoparticles as tracers and a key advantage is the absence of any radiation delivered to the patient. Recent developments in this area were reported recently in (Knopp et al., 2017).

6.1. Hyperpolarized gas MRI

The introduction of hyperpolarized gas has improved the development of functional lung MRI by allowing measurements that are impossible with conventional proton-based MRI and maybe beyond the limits of any other technique (van Beek et al., 2004). In all possible applications, hyperpolarized gas MRI appears as a solution for one of the most important problems regarding the MRI of the lung, e.g. the weak signal intensity coming from the low density of air-filled lung parenchyma that results in low proton density (Mosbah et al., 2008).

Noble gases are hyperpolarized through the transfer of angular momentum from circularly polarized light to the nucleus, known as optical pumping. This process allows the hyperpolarized gas to exhibit polarizations exceeding the thermal equilibrium level (Moller et al., 2002). Such processes have been demonstrated on ^{3}He and ^{129}Xe, both with potential clinical applications, starting from 1994 when the first publication appeared (Albert et al., 1994) from the Princeton group and Magnetic Imaging Technologies Inc. was created. Despite all the problems including a ^{3}He shortage in 2008, the field has demonstrated a continuous improvement in polarization performance, but is still facing regulatory and technical hindrances. In order to facilitate universal access to the technology, this field is demanding a coordinating effort to bring a comprehensive package solution with the input and collaboration of many types of expertise and businesses. For a real final clinical application, any new user needs to take into account that this will need: 1) an MRI system with a broadband amplifier (for not proton based applications), 2) a gas polarizer (probably different for ^{129}Xe and ^{3}He), 3) a polarimetry and calibration method, 4) a dose delivery system with an automatic or semi-automatic gas delivery applicator, 5) a dedicated chest coil (dual ^{1}H-^{129}Xe or ^{1}H-^{3}He, or triple nuclei coil (^{129}Xe-^{3}He-^{1}H and applications have been demonstrated by some investigators and coil manufacturers), 6) hyperpolarized-proofed MRI pulse sequences, 7) gas phantoms for quality control, 8) more affordable access to ^{3}He (almost impossible in Europe, except in the Sheffield group) or ^{129}Xe supplies, 9) special software for data analysis, and 10) lastly any application needs to go through the corresponding Investigational New Drug Application and obtain the Institutional Review Board approval to start these studies. For Food and Drug Administration (FDA) clearance, phase II clinical trials have finished in Summer 2016 and the Phase III trial is about to begin in 2017.

Despite all these issues, hyperpolarized gases still appear to be a promising technique and probably the only one that can evaluate and quantify air flow and aerosol deposition into the airways (^{19}F MRI is probably far from this due to sensitivity restraints). Although some different data acquisition encoding methods are possible, De Rochefort et al. proposed a novel application; combining dynamic radial MRI with phase contrast and hyperpolarized ^{3}He to map velocities *in vivo* and in replicas of the human airways (de Rochefort et al., 2006). Phase contrast is a well-known and established technique

in proton MRI to map blood velocities and relies on the quantification of the signal phase. Phase contrast makes it possible to quantify motion and is not constrained by signal-amplitude variations. Radial encoding (Song et al., 2001) was used to improve the temporal and spatial resolution of the final application. This combination overcomes previous approaches for measuring gas flow *in vitro* using thermally polarized ^{1}H (Koptyug et al., 2000) or hyperpolarized ^{129}Xe (Brunner et al., 1999). In previous approaches, acquisition times were not appropriate for *in vivo* measurements due to the time scale of a breathing cycle.

In the next section, we summarize the different steps of the first demonstration of human gas flow measurements in the trachea using ^{3}He performed by de Rochefort *et al.* to illustrate the potential and the difficulties that MRI-based methods exhibit, noting these are similar to other imaging techniques included in this article. Immediately after the gas is produced, a mixture, in this case with nitrogen, is prepared at atmospheric pressure, for rapid transferral to the imaging system. In this first application, authors did not include any automatic or semi-automatic gas delivery device, so the gas was directly inhaled by a volunteer from a Tedlar bag containing the gas mixture, and the gas was extracted through a valve with a mass flowmeter to monitor the input gas flow. The volunteer was previously trained to breathe slowly by the mouth to establish a steady flow in the trachea, placed in a prone position with a dedicated MRI coil to increase SNR. Proton MRI was initially performed for scout and localization imaging. A hyperpolarized gas mixture (52% ± 10% ^{3}He, 48% ± 10% N_2 in this case) was inhaled via a deep inhalation from the volunteer's lung residual volume. The bolus volume of the tracer gas (around 800 ml) was first inhaled and then supplemented with air to make the total inhaled gas volume (the total volume was not specified by the authors). For a reproducible location, cross-sectional MRI slices were positioned in the trachea, 4 cm downstream from the vocal cords. ROIs were manually selected for each reconstructed image. Due to the radial acquisition, data reconstruction was performed by complex FBP (this is not standard in all MRI vendors, so it will probably require offline reconstruction). For a set of projections, the raw data was first filtered by a ramp, and then Fourier-transformed and back-projected. The velocity component of each voxel was determined by the phase difference between the corresponding encoded image and the reference image scaled with a phase-conversion factor. The integration of through-plane velocity over the chosen section provided a measurement of the flow rate.

The results of the measurements of this experiment are shown in Fig. 17 (Fig. 7 from reference (de Rochefort et al., 2006)). Human trachea velocity maps found by de Rochefort *et al.* agreed with findings from *in vitro* models and CFD (Heenan et al., 2003). The profiles of the through-plane velocities presented an M-shape along the left-right axis, and an asymmetrical shape along the anteroposterior axis, with higher velocity magnitude in the anterior part.

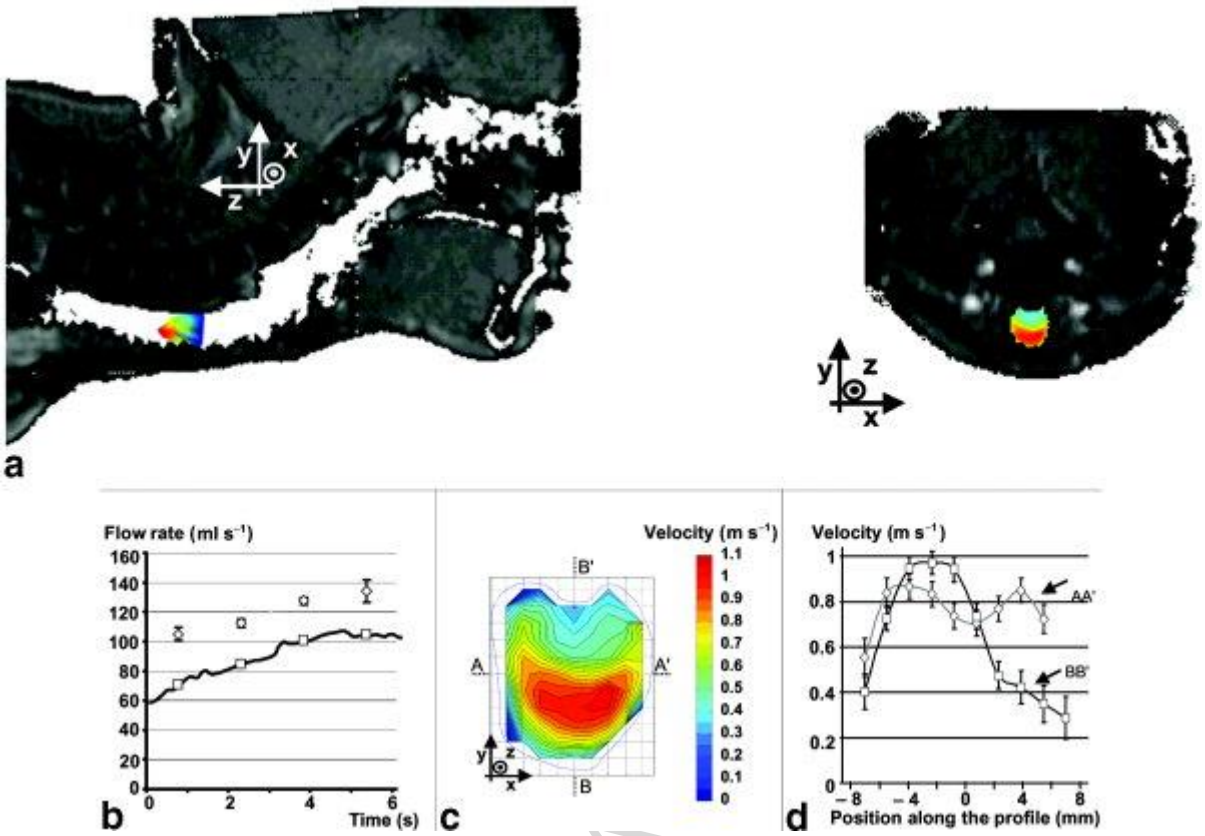

Fig. 17. Phase- contrast velocimetry with hyperpolarized ^{3}He for in vitro and in vivo characterization of airflow. Reprinted from (de Rochefort et al., 2006) with permission of John Wiley and Sons.

In another example, Collier and Wild (2015) conveniently implemented the Compressed Sensing technique (Lustig et al., 2007) to reduce the ever shorter acquisition times of hyperpolarized gases in human lung MRI in order to measure flow velocity maps in free breathing lungs. Compressed sensing works by acquiring a small number of random linear combinations of the signal values, much smaller than the number of signal samples nominally defining it. The signal is still reconstructed with good accuracy from these measurements by a nonlinear procedure. For MRI, the sampled linear combinations are simply the individual Fourier coefficients (*k*-space samples). In that setting, compressed sensing is expected to be able to make accurate reconstructions from a small subset of *k*-space rather than an entire *k*-space matrix. Application of compressed sensing to lung MRI with hyperpolarized gases is based on the intrinsic sparsity of the images, as the gas is confined to the airways only. Collier and Wild extended the sparsity of the complex difference image (Kwak et al., 2013) to a four point velocity encoded scheme and developed a compressed sensing reconstruction algorithm for hyperpolarized gas flow in three directions with a time resolution of 1.2 s. This temporal resolution still needs to be improved for rapid flow fluctuations during a normal breathing cycle at rest. The feasibility of these methods was demonstrated with both ^{3}He and ^{129}He mixed with nitrogen in the trachea and main bronchi (see Fig. 3 from reference (Collier and Wild, 2015)).

Due to the high sensitivity and possibilities of hyperpolarized gases, these techniques present also a potentially unique opportunity for the study of aerosol deposition into the human airways. In a study using mouth–throat replicas Sarracanie et al. (2015) measured extra-thoracic aerosol deposition using phase-contrast ^{3}He MRI and compared the results with gold-standard SPECT. For this application, a double-labelled aerosol with superparamagnetic iron oxide (for MRI labelling) and radioisotope ^{99m}Tc (for SPECT) was prepared to ensure the same deposition pattern for both measurements. Iron-based markers placed in the magnetic field of an MRI unit generate dipolar fields that locally modify the magnetic field, which typically leads to regions of low signal amplitude (Branca et al., 2010). The

magnetic field perturbations induced by the presence of iron are embedded in the phase of the magnetic resonance signal and can be processed to obtain absolute quantification of the iron mass distribution (de Rochefort et al., 2008; Mills et al., 2008). By measuring the relaxation times of the total magnetic moment or by mapping the static magnetic field perturbations in the presence of superparamagnetic iron oxide markers, the spatial distribution of the absolute aerosol particle quantification can be determined (Martin et al., 2008). Hyperpolarized ^{3}He was used to overcome the low-SNR and long-acquisition time limitations of lung imaging. The results of both the magnetic perturbation and quantified aerosol particle deposition are seen in Fig. 18 (Fig. 6 from reference (Sarracanie et al., 2015)). Results from this work show that particle deposition can be assessed with ^{3}He MRI and iron oxide labelling through measurement of the inferred static magnetic field perturbations.

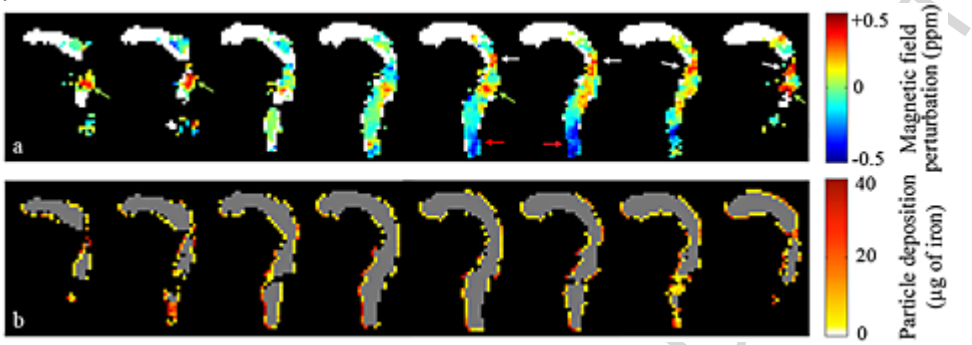

Fig. 18. Phase- contrast helium- 3 MRI of aerosol deposition in human airways. Reprinted from (Sarracanie et al., 2015) with permission of John Wiley and Sons.

The introduction of hyperpolarized gases has allowed MRI to enter into the field of air flow quantification using velocity-encoding MRI. This measurement and applications will evolve in a clinical setting in parallel to the resolution of all technical difficulties and regulatory approval related to the use of these gases. Still, the field of hyperpolarized gas applications requires complex infrastructure for gas production and the confluent effort of different technology providers. As far as we perceive the field of quantification of aerosol deposition by MRI, this field can only benefit and expand, aligned with the expansion of MRI systems equipped with broadband amplifiers (required for all non-proton based MRI applications), the growth of the hybrid imaging systems markets and the corresponding development of dual makers. In this line, ^{19}F solutions, mainly using perfluorinated compounds and doped iron oxides can benefit. As we have seen in this article, Gd preparations have been also introduced, but safety investigations related to Gd deposits in different regions are currently under evaluation and will suppose a barrier difficult to overcome for future applications. The use of dual systems, such as those based on metastable ^{99}Tc (SPECT) and ^{68}Ga (PET) -^{1}H protons, combined with the use of hyperpolarized SNR can then have enormous potential and future.

Advantages:

- Both flow field and particle deposition can be measured,
- Can be combined with SPECT and PET (for simultaneous measurements).

Disadvantages:

- Complex infrastructure and highly skilled personnel needed,
- Low resolution for flow measurement compared to PIV.

6.2. Optical Coherence Tomography (OCT)

OCT was introduced in 1991 (Huang et al., 1991) as a method to image biological samples at high resolution. OCT is based on white light interferometry with near infrared wavelength range (NIR) due to the relatively high penetration of NIR. A probe shines light onto the sample and the scattered light is collected in reflection, hence OCT needs access to the sample only from one side. The resolution in beam direction (axial), as well as perpendicular (transversal), is of the order of 1 to 15 µm (Drexler et al., 1999). The imaging range is limited by absorption and scattering, reaching no deeper than 1 mm in most tissues. Moreover, the Rayleigh length of the Gaussian beam that is typically used will limit the sensitive range to less than 1 mm. For a single depth scan, called A-scan, the length of the reference arm has to be varied over the measurement range. Due to this mechanical depth scanning, the speed of OCT was rather limited until a breakthrough in speed was achieved by introducing the concept of Fourier Domain OCT (FD-OCT), also known as Frequency Domain OCT. In FD-OCT, the mechanical depth scanning is replaced by spectral analysis of the interfering light. Interfering light causes, as a function of wavenumber (reciprocal of wavelength), periodic oscillations with a frequency proportional to the optical length difference between sample and reference arm. It can be shown that FD-OCT is not only much faster, but achieves a better SNR compared to the previous method, called Time Domain OCT (TD-OCT) (de Boer et al., 2003; Choma et al., 2003; Leitgeb et al., 2003). The interference spectrum can alternatively be acquired by analysing the light with a spectrometer, resulting in a technique called Spectral Domain OCT (SD-OCT), or by sweeping the wavelength of the incident light, known as optical frequency domain imaging (OFDI) (Vakoc et al., 2009) or Swept-Source OCT (SS OCT) (see Fig. 19). The first is limited in speed by the spectral read out of the CCD[9] or CMOS[10] cameras while the second achieves even higher speeds after the introduction of Fourier domain mode locked (FDML) lasers. Fast SD-OCT systems achieve today more than 200,000 A-scans/s, while FDML systems regularly accomplish up to 1.5 million A-scans/s. 20 million A-scans/s have been demonstrated, which means video rate volume scans (Wieser et al., 2010). The acquisition of 2D and 3D images is achieved by deflecting the beam using galvanometers (Duma et al., 2011), resonant scanners or microelectromechanical systems (MEMS) (Jung et al., 2006; Lu et al., 2014). A 2D image, with intensity colour coded as a function of depth and one coordinate, is called, in analogy to ultrasound, a B-scan. For other promising clinical applications, rotating fibre optic catheters were developed enabling the imaging of hollow organs and cavities like the esophagus (Tearney et al., 1997; Vakoc et al., 2007) and human vessels (Bezerra et al., 2009; Brezinski, 2006; Tearney et al., 1997) by OCT. Optics with smaller numerical apertures and therefore longer Rayleigh lengths can collect over a larger distance of 10–30 mm only a fraction of the scattered light, which reduces the signal intensity and transversal resolution (100–200 µm). This is still sufficient for the anatomical structure, which explains the name of the method “anatomical OCT” (aOCT) (Armstrong et al., 2006; Bu et al., 2017; Wijesundara et al., 2014).

[9] Charge-coupled device
[10] Complementary metal–oxide–semiconductor

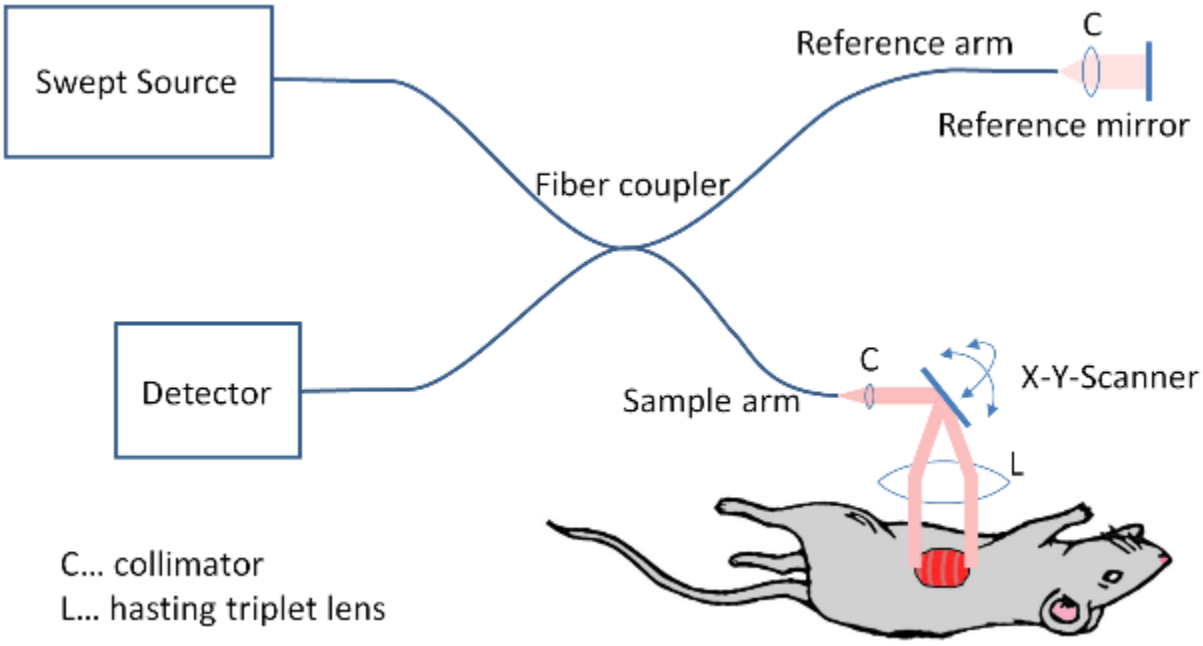

Fig. 19. Principle of SS OCT. The light from a tunable laser source is guided by optical fibres to a fibre coupler. While one part is reflected at the reference mirror the other part is scattered and partially reflected at the sample, placed underneath a two dimensional scanner, steering the light over the sample. The interfering light is recorded with a detector in the fourth arm of the fibre coupler as a function of wavelength. From the spectrum, the depth information is retrieved.

Imaging airway and alveolar structures

In order to image the airway and alveolar structures by OCT, three different attempts have been made. External scanning can be applied to isolated lungs by visualizing the alveolar structure close to the pleura (Meissner et al., 2009a; Meissner et al., 2009b). With some effort, this method can also be applied to anaesthetized animals by opening the chest or by preparing a thoracic window *in vivo* (Meissner et al., 2010a). This method has been applied to mouse and rabbit models to study alveolar sizes and the change during ventilation in healthy and injured lungs (see Fig. 20). While in the early systems gated imaging was used to study the dynamic shape during the ventilation cycle (Meissner et al., 2010b), modern high-speed systems capture complete alveoli with some tens of fps, sufficient for breathing rates of the order of one per second (Kirsten et al., 2013). In larger animals, the movement of the lung prevents single alveoli to be followed through the complete ventilation cycle. Therefore, lightweight MEMS-based probes were developed to resting on the lung and follow the alveolar structures (Namati et al., 2013). These measurements confirmed that most of the compliance of the lung is caused by the cyclic dilatation of the alveoli.

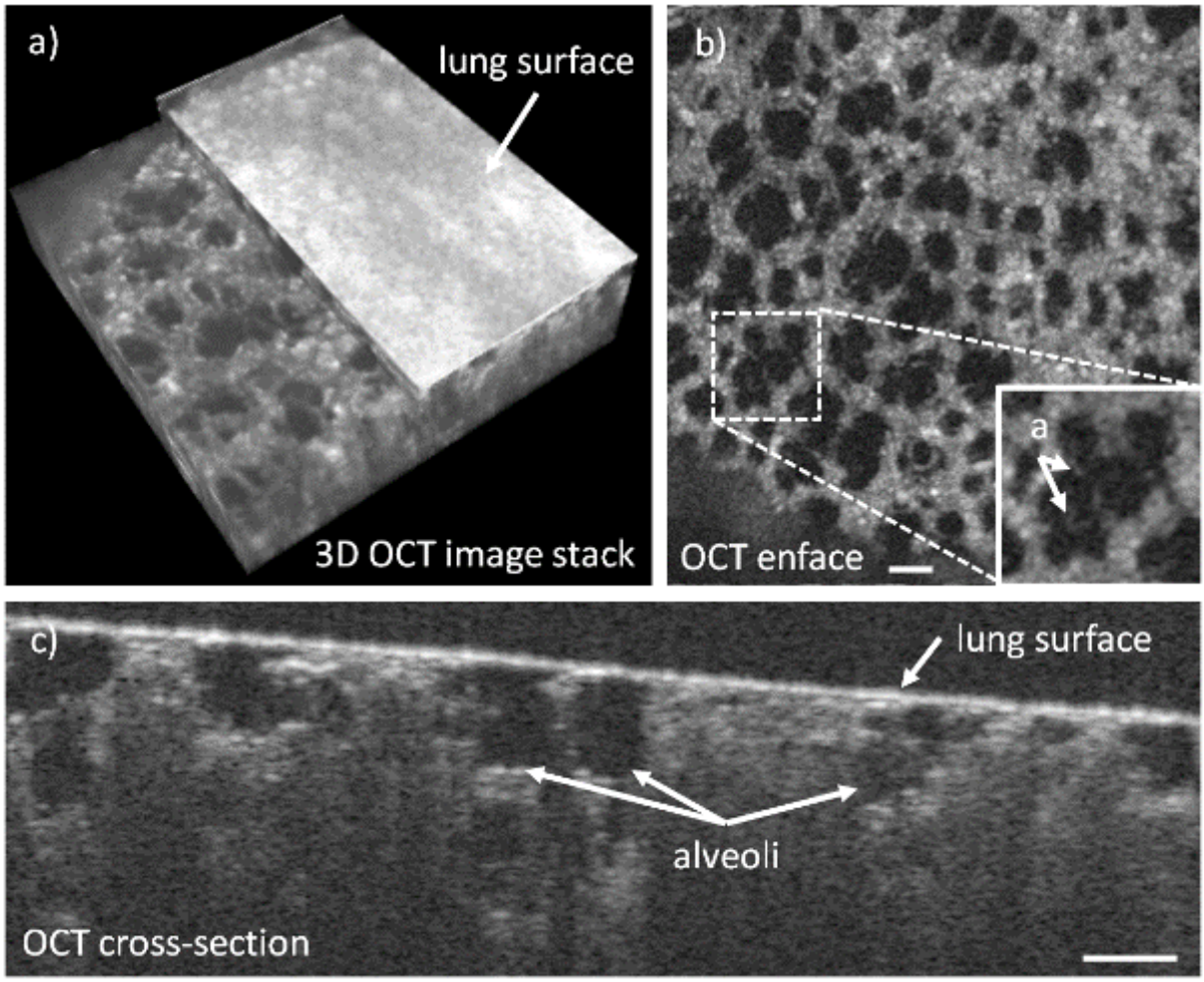

Fig. 20. Imaging of alveolar structures with OCT in ventilated rats. OCT allows the imaging of morphological features of lung tissue. Even the inner alveolar walls can be visualized. Scale bar 100 µm. While a) shows the 3D image with part of the lung surface (pleura) removed from the data set, b) shows a plane approximately 50 µm beneath the lung surface, c) shows a cross section perpendicular to the pleura. Imaging of deeper alveoli is hampered by the refractive index step between tissue and air.

To access internal regions of the lung, endoscopic OCT probes have been used. Typically, such probes use radial scanning by rotating the entire probe or by using micro-mechanical motors placed in the probe (Yang et al., 2004). While the rotation provides circumferential 2D images, the fibre may be retracted while accumulating subsequent radial images to provide 3D information (Armstrong et al., 2006; Bu et al., 2017; Wijesundara et al., 2014) (See Fig. 21).

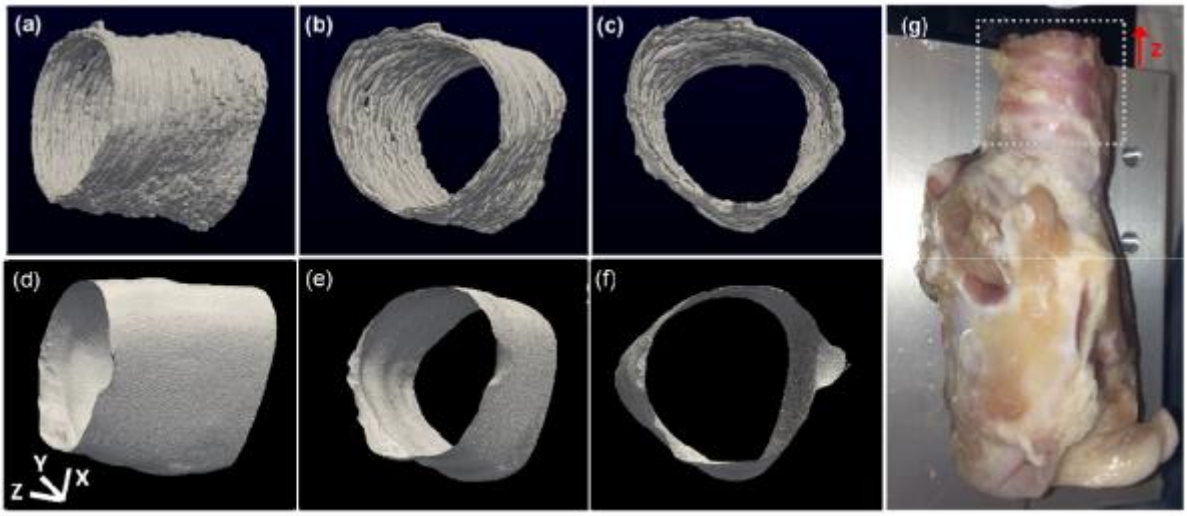

Fig. 21. Anatomical OCT images of a swine trachea displayed in three different viewing angles. (d)–(f): corresponding CT images. (g): photograph of the swine airway; the region that was imaged is indicated by the dotted square. The x, y, and z scale bars each represent 3 mm. With permission reprinted from (Wijesundara et al., 2014).

A third strategy uses miniaturized OCT needle probes. The needle probe can be inserted through the tissue into the region of interest that may be located several centimetres below the surface. Scanning is again performed by rotating the needle or the focusing optics inside the needle. Although the size of needle probes has been reduced to a diameter of about 310 µm, the insertion of the needle will cause some trauma (Lorenser et al., 2011). As the needle can hardly be translated forth and back, the same tissue cannot be imaged during different states of the ventilation cycle. For repetitive scans, probes consisting of an inner part that translates rapidly back and forth multiple times per second was developed to allow 2D image acquisition (McLaughlin et al., 2012).

The imaging of alveolar structures is hampered by the repeated refractive index change from air to liquid, limiting the useful depth to only one or two layers of alveoli. Therefore, several attempts have been made to fill the lung with an index matching fluid. For *ex vivo* imaging, the lung can be filled completely with saline water (Lorenser et al., 2011) or ethanol (Meissner et al., 2009a) increasing the useful imaging depth to 5 or more alveoli in depth. While these approaches are not suited for *in vivo* imaging, a small amount of fluid around the probe can enhance imaging without causing trauma to the animal (Quirk et al., 2014). Moreover, the lungs could be ventilated with a liquid with perfluorocarbons that have a high transport capacity for oxygen and carbon dioxide, in order to enable enhanced OCT imaging *in vivo* (Schnabel et al., 2013).

Potential for flow and aerosol measurements

In Doppler OCT, mostly used to visualize the velocity of scattering particles in flowing fluids, the phase of the signal between A-scans at the same or nearly the same position is analysed (Leitgeb et al., 2003). The phase difference is proportional to the velocity component in the direction of the optical beam. The transversal velocity component can be estimated by phase noise (Walther and Koch, 2009) or by using multiple beam OCT (Haindl et al., 2016; Chen et al., 2017), the latter resulting in a 3D velocity field. Besides Doppler OCT, PTV[11] (Jonas et al., 2011), PIV (Buchsbaum et al., 2015) and correlation-based approaches (Huang et al., 2015) are used to quantify the flow field.

While Doppler methods are mostly applied to the measurement of blood flow, where the erythrocytes form the scattering particles, oil droplets from Intralipid (Kirsten et al., 2015), polystyrene

[11] For the PTV and PIV see chapter 2.3.

microspheres (Jonas et al., 2011; Kirsten et al., 2015) and other particles down to sub-micrometre size (Cimalla et al., 2015; Grombe et al., 2016) can be used as tracers.

Flow measurements in the airway will be hampered by the OCT probe, especially in the deeper and therefore slimmer parts of the airway. Visualization of flow in the alveoli needs particles to reach the alveoli after flowing through multiple airways and bifurcations, which may be difficult to achieve. Moreover, due to the low flow expected in the alveoli, the movement of particles may be dominated by Brownian motion.

The deposition of particles in the airways can likely be detected using suitable OCT probes. OCT can be tailored to detect labelled particles with high sensitivity. Labelling can be performed magnetically and by plasmonic resonance, leading to selective absorption and scattering (Oldenburg et al., 2016). Moreover, contrast can be generated by optical anisotropy and diffusion (Kalkman et al., 2010).

While OCT has so far not been used extensively to measure flow and aerosols in airways, OCT has significant potential to contribute considerably to this field. Measurements on replicas do not suffer from regulatory requirements, but the results may be of limited value because of differences in the dynamic behaviour and surface properties, as discussed earlier. Animal experiments may be challenging due to experimental and regulatory demands but the results would be more comparable to humans. While many of the measurements mentioned above cannot be justified with humans, because of the negative side effects, any possible experiments with humans should only be performed if the individual can benefit from the measurement.

Advantages:

- fast 3D information without ionizing radiation,
- resolution in the µm range,
- Doppler-Information without additional hardware,
- only one optical port needed.

Disadvantages:

- difficult marking of particles,
- optical access needed,
- depth range limited to some mm, maximal few cm at lower resolution.

6.3. Phase Contrast X-ray Imaging (PCXI)

In the last two decades, new methods of x-ray imaging have been developed that are sensitive to soft tissue structures like the respiratory system, via the use of “phase contrast” (Wilkins et al., 2014). Research groups in the field are focusing on realising this technique in a clinical imaging system (Bravin et al., 2013) and are increasingly applying this kind of imaging in biomedical research with animal models.

A conventional x-ray image captures the attenuating properties of structures, in effect creating a shadow image. A phase contrast x-ray image is also sensitive to the refractive properties, and in some cases scattering properties, of any structures. In Fig. 22, we see that attenuation by the sample (described by β for a given material) causes a reduction in the amplitude of the incident x-ray waves (shown the by red arrows), resulting in reduced intensity at the image detector. While this produces strong contrast in the case of bones, soft tissues attenuate weakly and hence are not clearly seen in a conventional image. If an x-ray wavefield passes through materials with different refractive properties (described by δ), a difference in the phase of the x-ray wavefield is introduced (shown by the blue lines of constant phase), in effect changing the direction the wavefield is propagating (see the black arrows). Phase contrast imaging is sensitive to these phase shifts, resulting in much better visualisation of soft

tissue structures. The lungs and airways are particularly well-suited to PCXI because the difference in δ between air and tissue is large compared to that between other tissues, resulting in strong x-ray phase variations from air-filled tissue structures. This means that the respiratory system can be visualised with high sensitivity and resolution down to the µm scale.

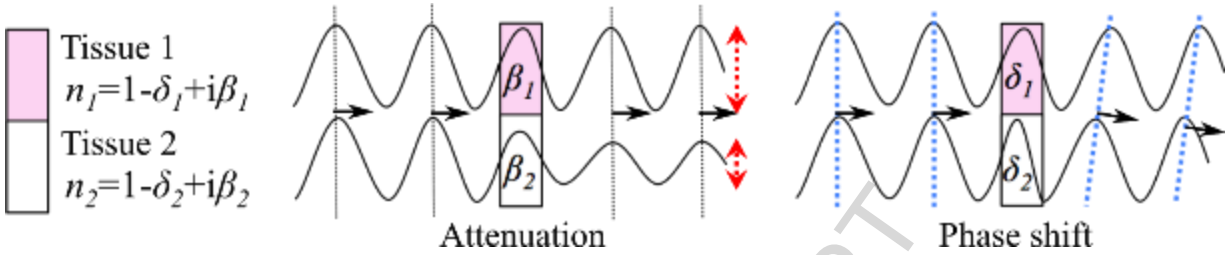

Fig. 22. The x-ray properties of different tissues at a given x-ray energy can be described using a complex refractive index n, where β describes how much the tissue will attenuate the x-ray wavefield and δ describes how the tissue will change the phase of the x-ray wavefield. PCXI extracts quantitative measures of how the phase has been altered by soft tissue structures.

Because the x-ray phase variations introduced by the lungs cannot be directly recorded in the same way as x-ray intensity variations, a special optical set-up must be used to extract x-ray phase shifts or variations. There are several different PCXI set-ups that have been developed, including propagation-based (Cloetens et al., 1996; Snigirev et al., 1998), crystal and grating interferometry (Bonse, 1965; David et al., 2002; Pfeiffer et al., 2006), analyser-crystal (Förster et al., 1980; Ingal and Beliaevskaya, 1995), edge-illumination (Olivo and Speller, 2007) and speckle-tracking (Bérujon et al., 2012; Morgan et al., 2012)/single exposure single-grid set-ups (Morgan et al., 2011; Takeda et al., 1982; Wen et al., 2010). Each set-up provides a different set of advantages in terms of speed, resolution, sensitivity and the requirements on the x-ray source (Wilkins et al., 2014).

Because many of these set-ups require relatively uniform x-ray phase (e.g. see the incoming waves in Fig. 22), much of the development has taken place using highly coherent synchrotron x-rays. A synchrotron facility accelerates electrons around a circular path that is hundreds to thousands of meters in circumference. These electrons travel at near-relativistic speeds, guided by magnets to produce bright, low-divergence x-rays that can be made monochromatic and used in a range of investigative techniques. Imaging applications typically take place tens to hundreds of meters from the x-ray source point, resulting in a highly coherent beam. The translation of PCXI techniques from the synchrotron to more accessible, lower-cost x-ray sources is an active area of research (Olivo and Castelli, 2014), and in particular has investigated liquid–metal–jet sources (Larsson et al., 2011) and compact sources driven by inverse Compton scattering (Bech et al., 2009). Nevertheless, a synchrotron is an invaluable biomedical research tool, in particular because the associated high x-ray flux enables fast imaging (e.g. 200 Hz in (Morgan et al., 2016)), such that the movement and detail of the lungs can be captured in exquisite detail.

Literature to date

Several studies to date have used PCXI to better understand the respiratory system and assist in treatment development, with some examples shown in Fig. 23. High-resolution structural characterisation of the airways is possible by combining PCXI with CT (Parsons et al., 2008), capable of revealing individual alveoli (Sera et al., 2013), even within an *in vivo* volumetric time series (Lovrić, 2015).

By capturing a time sequence of images, it is possible to image the lung dynamics, or any changes to the respiratory system in response to a treatment. One of the very first dynamic PCXI experiments performed at a synchrotron monitored the respiratory action of a beetle (Westneat et al., 2003),

capturing the dilation and contraction of tracheal airways. More recent *in vivo* work has utilised animal models of human lung conditions, primarily in mice, rabbits and rats (Donnelley et al., 2010), with some recent work performed in pigs (Donnelley et al., 2017) and sheep. The highest resolution work (see Fig. 23a) has monitored *in vivo* µm-sized changes in the tracheal airway surface liquid depth in mice in response to the nebulised delivery of surface-rehydrating treatments (Morgan et al., 2014). This is in the context of treating cystic fibrosis airway disease, which develops as a result of a reduced airway surface liquid depth that impairs the clearance of inhaled debris (Tarran et al., 2001). Also in this context, airway surface liquid changes have been monitored in response to the deposition of bacteria in excised pig tracheas (Luan et al., 2014). Studies have directly investigated the *in vivo* clearance of inhaled debris via mucociliary clearance (Fig. 23a), monitoring individual glass particles, several tens of micrometres in diameter, studying changes in clearance rate in response to treatment (Donnelley et al., 2014a) and over a period of 25 hours (Donnelley et al., 2014b), in mouse and pig models. The clearance of larger particles in the form of 350 µm diameter tantalum disks has also been imaged in new-born pigs via multi-detector-row CT (Hoegger et al., 2014). The ability of x-ray imaging to monitor such behaviours *in vivo* presents obvious advantages over studies that use excised tissue or a tissue culture.

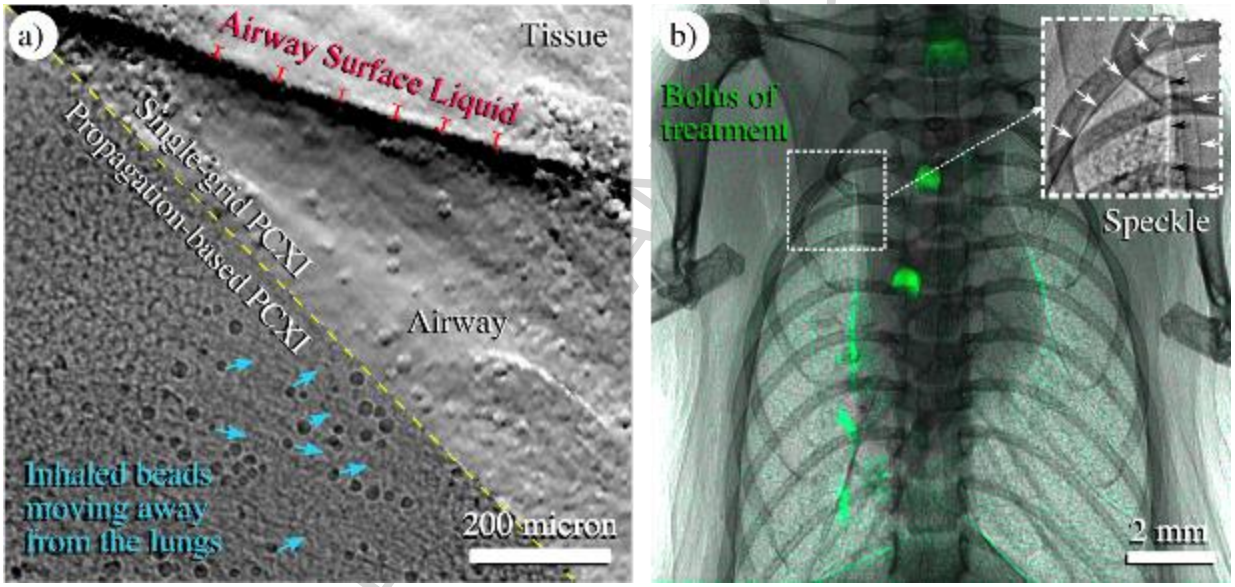

Fig. 23. Examples of respiratory images at various scales obtained using synchrotron-based PCXI. a) One side of the trachea (running horizontally) in a mouse, allowing measurements of the airway surface liquid, shown in red (Morgan et al., 2014) and the clearance velocity of inhaled 10–25 µm debris, shown in blue (Donnelley et al., 2014a). Note the upper right is captured with single-grid PCXI, which displays the rate of change of tissue thickness/composition and the lower left with propagation-based PCXI, where edges are enhanced. b) The delivery of a liquid bolus of treatment into the lungs of a mouse, with digital subtraction highlighting treatment location in green (Donnelley et al., 2013). This image also shows the extra detail obtained in propagation-based phase contrast (inset), with dark lines highlighting the edges of major airways and the periphery of the lungs (posterior surface shown with white arrows, anterior with black arrows), and a speckle pattern seen from the lungs.

At the scale of the entire lungs, several different PCXI modalities have been applied in biomedical research. Propagation-based phase contrast, which enhances the air/tissue interfaces (Kitchen et al., 2004) (Fig. 23b), has been used to monitor the regional distribution of air as newborn rabbit pups take their first breaths (Hooper et al., 2007), enabling optimisation of the ventilation strategy for pre-term

infants (te Pas et al., 2009). The many overlapping alveoli act like lenses in propagation-based PCXI, creating a speckle pattern, as seen in Fig. 23b), that can be analysed to infer information about the alveolar size and density (Carnibella et al., 2014; Kitchen et al., 2015). This speckle pattern can also be tracked through the breath cycle using PIV techniques (see section 2.3) to map the movement of the lungs (Dubsky et al., 2012). When combined with CT and appropriate boundary conditions, CT-PIV can be performed to extract local airflows (Dubsky et al., 2012). This is useful clinically in locating areas of disease (Fouras et al., 2012; Stahr et al., 2016), and the detailed airflow measurements can inform treatment deposition simulations (Dubsky and Fouras, 2015).

Grating interferometry PCXI has also been used to image the lungs, in particular using the scattering/dark field signal. A reduced dark field signal will be seen where there are fewer alveoli to scatter the x-rays, either due to breakdown from emphysema (Hellbach et al., 2015) or wall thickening from fibrosis (Yaroshenko et al., 2015) (note these cases could be differentiated using the attenuation signal as complementary information).

Finally, the inhalation of a xenon contrast agent has been captured at synchrotron sources in the lungs of mice (Bayat et al., 2001), and combined with CT. This unique set-up at the European Synchrotron uses two beams in parallel, one with energy just below and the other just above the K-edge for xenon, so that the difference in attenuation between the two images is large for xenon, but no other part of the image. Digital subtraction can then isolate xenon in the image, tracing the flow of the gas into the lungs. In a similar way, iodine, a highly attenuating liquid, has been used as a substitute for liquid bolus treatments, with high-speed imaging determining the regional distribution in the nasal airways for a given volume (Donnelley et al., 2013). Bolus treatments were also tracked in the lungs, but only down to the third generation, due to an overlapping signal from the lungs and a reduced volume of iodine resulting in weak contrast.

Potential for flow and aerosol measurements

While most of the PCXI respiratory applications so far have focused on assessing the effects of a treatment or a disease, PCXI also presents opportunities for flow and treatment deposition measurements, most easily in animal models. Human imaging at synchrotron x-ray sources requires several years of planning in order to ensure radiation dose is well-controlled and within safety limits (e.g. see dosimetry requirements for radiation therapy in humans at the ESRF[12] (Prezado et al., 2011) or mammography at Elettra[13] (Longo, 2016)). There is also some development required to achieve the field of view necessary to image the whole human lung, for example manufacturing large gratings for grating interferometry (Schröter et al., 2017). Commercial scanners to date that use phase contrast have focused on mammography (e.g. Konica Minolta's PCM system), however lung scanners are a topic of ongoing research by several medical imaging companies.

X-ray CT-PIV already captures useful functional information for *in vivo* local airflow measurements in animal models (Fouras and Dubsky, 2015), and there are clinical trials underway for 2D x-ray PIV (4Dx Limited, 2017). With sufficiently sensitive detectors to ensure a clinically-compatible radiation dose, CT-PIV could become available for human imaging. Imaging the inhalation of Xenon is also a possibility in imaging flow, although the time resolution is limited when capturing 3D information from a single inhalation. At synchrotron x-ray sources, the patient must be rotated to perform CT, and a high rotation speed, necessary for high time resolution, could influence the flow of gas and any deposition of treatment.

Aerosol measurements via PCXI are more difficult than airflow measurements. Unlike nuclear methods, treatment cannot be easily separated in an image from the attenuating and phase-shifting effects of the surrounding organs. Bolus deliveries allow the concentrated localisation of a contrast agent, increasing the contrast of the treatment relative to surrounding anatomy (Donnelley et al., 2013) (Fig. 23b). Aerosolised treatment does not offer this benefit, and hence sensitivity is much lower,

[12] The European Synchrotron Radiation Facility
[13] The third-generation Italian synchrotron radiation facility

particularly given the lungs are constantly moving and do not present a static background, and even when images are triggered to a single point in the breath cycle, cardiovascular movement remains. One alternative would be to focus on just a small region of the airway system so that any deposited treatment is easier to resolve. If an aerosolised treatment were to be detected by PCXI in the whole lung, it must either be strongly attenuating or effectively change the diameter of the airspaces sufficiently that the speckle pattern changes in propagation-based PCXI or the dark-field signal changes in grating interferometry PCXI. The sensitivity of these techniques to these changes is currently under investigation. An alternative solution would be to introduce to the aerosolised treatment some highly attenuating or refractive particles or a contrast agent that would not be absorbed by the body, and then capture the deposit sites via a high-resolution PCXI-CT (either post-mortem in an animal model, or triggered by ventilation to the same point in the breath cycle). Note that the PCXI techniques discussed here could also be used with models of human airways, however there is not a strong advantage to using x-rays compared to visible light in an optically-transparent model, besides the possibility to increase the spatial resolution, which is not a real issue in any case.

While the suite of PCXI techniques is not currently used in flow or aerosol deposition measurements, these new modalities provide significantly increased soft-tissue sensitivity and present opportunities in terms of *in vivo* spatial and temporal resolution.

Advantages:

- high spatial resolution (down to 1 µm),
- high temporal resolution (up to 1000 Hz),
- 3D visualisation possible,
- possible in vivo.

Disadvantages:

- radiation dose,
- signal from treatment not easily separated from the background in the way seen with nuclear imaging methods.

7. Conclusions

The ongoing development of technology for the administration of therapeutic aerosols leads to a pressing need to predict and assess the precise deposition sites of inhaled particles on a microscale level. This task calls for a sophisticated combination of methods ranging from fluid mechanics, mathematics, engineering, pharmacology and medicine. Modern computational methods allow researchers to solve the equations that govern flow and particle motion within human lungs at sufficient resolution. However, these calculations are extremely sensitive to boundary conditions, the method used to solve them, and the practical numerical implementation of the method in the software. Quality experimental data describing deposition is immensely important both for setting boundary conditions in simulation and validating CFPD results.

The description of available experimental methods given here has shown that there is no method that can be used as a universal tool to cover all aspects and demands of CFPD calculations. Keeping in mind that the prediction of local deposition sites at the microscopic level in individualized human airways seems to be the next goal, we should find methods capable of acquiring the deposition data at sub-millimetre resolution. The review presented here showed that the common *in vivo* methods are unable to provide results in such resolution. The CFPD predictions provide results with a resolution that surpasses conventional experimental methods. However, if no *in vivo* experimental data is available for validation, measurements must be performed either *in vitro* or in replicas of human lungs. In the case of airway replicas, all of the methods described here can be useful at a certain stage of the

simulation (acquiring the lung geometry, defining the boundary conditions, validating the local flow velocities and particle deposition) and inevitably must be combined. Note that their physical limits, expressed as measurement uncertainties, need to be carefully considered. To summarize the main features, strengths and limits of the presented methods, we prepared Table 2, which lists all the methods in a way to enable fast comparisons. We needed to make some simplifications to fit all the methods to the limited space of Table 2, so the reader is kindly asked to refer to the respective chapter of this paper to obtain deeper insight on the selected method.

Table 2
Main features of the experimental methods.

Technique	Spatial / time resolution	*In vivo* / *in vitro* / …	Quantities acquired / uncertainties	Fluid(s)[a]	Particles[b]	Cost[c] / availability	Requirements	Special features	Calibration / adjustment[d]
HWA	1 mm / <100 kHz	R	*u* (min. ±0.03 m/s; 5%) / 1C–3C	Gas	N	4 k€ for a single channel device/common in fluid mechanics	Inserting holes	Equidistant sampling, intrusive measurement	Daily / daily
LDA/PDA	0.1 mm / <100 kHz	R	*u* (±1%); *D* (±0.5 μm); *c* (±20%)	Both	Y	40–80 k€ per channel / common in fluid dynamics	Optical access, seeding	Random time sampling, on-line	No / daily
PIV/PTV	[e]>1 μm (for μ-PIV) / <10 kHz	R	*u*, 2C–3C / 0.2 px	Both	Y	80–200 k€ depending on PIV-type	Optical access, refractive index matching, seeding	Stereo PIV, Tomo-PIV, μ-PIV, scanning-PIV, endoscopic PIV	For each measurement
Concentration meas.	Airway generation/single breath	V/R	*c* (±10%)	Gas	Y	About 20 k€	Trained volunteers / lung replica	Simple, easily available	Annually/per experiment
Microscopy	1 mm to generation / per breath	R	*c* (±30%)	Gas	Y	3.5 k€ per equipped microscope/common in environmental sciences	Separable replica of airways, filter preparation equipment	Simple, time-consuming, established methodology	Monthly; regular intra and inter-laboratory checks
Gravimetry/ Fluorometry	Bifurcation, several cm^2	R/V	*c* (±10%)	Gas	Y	3 k€ (laboratory balance), units of k€ for fluorometer	Separable replica or volunteer (for fluorometry)	Simple, low resolution or reduced extent	Annually / per experiment
PET	1–5 mm	V	CPS	Gas	Y	Expensive, human scanners > 1 M€, radiochemistry facilities required.	Species to be tracked labelled with a positron emitter	*In vivo*, 4D (time + space), minimally invasive	Periodically (e.g. monthly)
SPECT/CT	Typically 5–10 mm in clinical scanners	V	CPS	Gas	Y	Cheaper than PET, most hospitals have SPECT, radiochemistry facilities required.	Species to be tracked labelled with a gamma emitter	*In vivo*, 3D, minimally invasive	Periodically (e.g. monthly)
^{3}He MRI		T/V	*u*, 3C, ±6.4%; ±25 mm/s	Air	N	Low availability	MRI with broadband amplifier; gas polarizer; dedicated chest coil; ^{3}He or ^{129}Xe supplies;	3D flow dynamics	Yes
PCXI	1 μm / 100 Hz	V	X-ray image sequence → *u*	Both	Y	Access to set-ups available via peer-reviewed application, without cost	X-ray absorbing or phase-shifting features	PIV of lung motion, 2D, 3D (time/space), 4D (time+space), individual particle motion	No

OCT	1–10 µm / single depth line ~1–10 µs, plane ~1 ms, volume 0.1 s	V/T/R	*u*, *c*	Both	Y	50–200 k€	Optical access, seeding	*In vivo*, 3D	No / rare

Particles | Flow | Flow and particles

V/T/R – *in vivo*/*in vitro*/in replicas; *u* – flow velocity; *D* – particle diameter; *c* – particle concentration; CPS – counts per second, which can be converted to radioactivity per unit volume and to % of injected dose per unit volume, a calibrated standard within the FOV is required for absolute quantitation; Y/N – yes/no; [a]it indicates the possibility to measure in air (or other gas) directly, or in a substitute liquid; [b]capability of the method to measure inhaled particles; [c]the cost is referred as a purchase price of the instrument; [d]the term adjustment express the frequency of adjustments of the system by operator; [e]depends on the size of the FOV in mm and the pixel number of the camera chip, can be determined by the formula: FOV/number of pixels of the chip, example: FOV is 100 × 100mm², camera has 1024 × 1024 px², resolution is 100 µm/px

In conclusion, some recommendations can be given regarding the suitable application of the methods: HWA is a standard flow measurement method applicable in lung flows, but is limited almost exclusively to replicas of lungs. This technique provides high temporal resolution and thus can be used to assess turbulence, for example at the inlet of the replica, and hence helps in determining boundary condition settings. However, HWA is point-wise and intrusive and therefore the optical methods are becoming more popular. LD-based methods are also point-wise, but do not alter the flow and (as well as HWA) can be applied with air as a flowing media. This is their main advantage compared to those methods that measure planar and volumetric flow, which require exact refractive index matching fluid. On the other hand, planar/volumetric methods offer unique details of flow structures usable for CFD validation.

Regarding the data available from aerosol deposition measurements, there is a basis of results acquired using conventional non-imaging methods. However, since these measurements were predominantly performed some time ago, the details of the geometry and measurement procedure have not always been presented in publications. The availability of the methods and their low price facilitate performing new, case-tailored experiments on the appropriate well-described airway replica if necessary. Standard medical imaging methods (PET, SPECT) approach the required resolution, however, they are already reaching their physical limits and therefore cannot be expected to attain the sub-millimetre resolution range. The emerging methods that are anticipated to progress lung flow measurements can image airflow *in vivo* (Hyperpolarised gas MRI), measure detailed structures in alveoli (FD-OCT) or even track individual particles (x-ray Phase Contrast Imaging). However, these techniques have limited accessibility and are not easily or inexpensively implemented more widely. Nevertheless, they promise to bring extremely interesting data that, together with CFPD, can provide great advancement in patient-tailored inhaled medicine.

This review described the broad portfolio of available experimental methods and showed that the selection of suitable methods is not straightforward. The crucial step for the selection of a suitable combination of experimental data or instrumentation seems to be at the beginning of the whole process — acquiring and reproducing the lung geometry. Especially when comparing distinct methods of CFPD calculations, it is necessary to use the identical lung geometry, preferably with sufficient experimental data to evaluate success. After the validation in a standard lung geometry model, the simulation could be extended and compared to *in vivo* data to verify agreement with real physiological processes in general terms. This already points to intensive interdisciplinary and international collaboration since individual teams do not usually have sufficient human and technological resources to provide both highly sophisticated CFPD calculations and specialised experiments.

Acknowledgements

This article is based upon work from COST Action MP1404 SimInhale 'Simulation and pharmaceutical technologies for advanced patient-tailored inhaled medicines', supported by COST (European Cooperation in Science and Technology).

Jan Jedelsky and Frantisek Lizal would like to acknowledge the financial support from the project GA16-23675S funded by the Czech Science Foundation.

Arnoldo Santos is a M+Visión COFUND Advanced Fellow and has received funding from Consejería de Educación, Juventud y Deporte of the Comunidad de Madrid and the People Programme (Marie Curie Actions) of the European Union's Seventh Framework Programme (FP7/2007-2013) under Research Executive Agency grant agreement n° 291820.

Kaye Morgan was supported by a Veski VPRF and completed this work with the support of the Technische Universität München Institute for Advanced Study, funded by the German Excellence Initiative and the European Union Seventh Framework Programme under grant agreement n° 291763 and co-funded by the European Union.

Jordi Llop and Unai Cossio would like to thank the PneumoNP project (FP7-NMP/604434) for financial support.

Disclaimer

The content of this article is the authors' responsibility and neither COST nor any person acting on its behalf is responsible for the use, which might be made of the information contained in it.

References

4Dx Limited, 2017. 4Dx, Melbourne, Australia http://4dx.com/
Adler, K., Brucker, C., 2007. Dynamic flow in a realistic model of the upper human lung airways. Experiments in Fluids 43, 411-423.
Adrian, R.J., Westerweel, J., 2011. Particle Image Velocimetry. CAMBRIDGE UNIV PRESS.
Adrian, R.J., Yao, C.S., 1987. Power spectra of fluid velocities measured by laser. Exp. Fluids 5.
Aisa, L., Garcia, J.A., Cerecedo, L.M., Palacin, I.G., Calvo, E., 2002. Particle concentration and local mass flux measurements in two-phase flows with PDA. Application to a study on the dispersion of spherical particles in a turbulent air jet. Int J Multiphas Flow 28, 301-324.
Albert, M.S., Cates, G.D., Driehuys, B., Happer, W., Saam, B., Springer, C.S., Jr., Wishnia, A., 1994. Biological magnetic resonance imaging using laser-polarized 129Xe. Nature 370, 199-201.
Albrecht, H.-E., 2003. Laser doppler and phase doppler measurement techniques. Springer, Berlin ; New York.
Altshuler, B., 1969. Behaviour of Airborne Particles in the Respiratory Tract, Ciba Foundation Symposium - Circulatory and Respiratory Mass Transport. John Wiley & Sons, Ltd., pp. 215-235.
Amornphimoltham, P., Masedunskas, A., Weigert, R., 2011. Intravital microscopy as a tool to study drug delivery in preclinical studies. Advanced drug delivery reviews 63, 119-128.
Armstrong, J.J., Leigh, M.S., Sampson, D.D., Walsh, J.H., Hillman, D.R., Eastwood, P.R., 2006. Quantitative upper airway imaging with anatomic optical coherence tomography. Am.J.Respir.Crit.Care Med. 173, 226-233.
Ay, M.R., Sarkar, S., 2007. Computed tomography based attenuation correction in PET/CT: Principles, instrumentation, protocols, artifacts and future trends. Iranian Journal of Nuclear Medicine 15, 1-29.
Backman, P., Tehler, U., Olsson, B., 2017. Predicting Exposure After Oral Inhalation of the Selective Glucocorticoid Receptor Modulator, AZD5423, Based on Dose, Deposition Pattern, and Mechanistic Modeling of Pulmonary Disposition. Journal of Aerosol Medicine and Pulmonary Drug Delivery 30, 108-117.
Bachalo, W., Rudoff, R., Brena De La Rosa, A., 1988. Mass flux measurements of a high number density spray system using the phase Doppler particle analyzer, 26th Aerospace Sciences Meeting. American Institute of Aeronautics and Astronautics.
Bailey, M.R., 1994. THE NEW ICRP MODEL FOR THE RESPIRATORY-TRACT. Radiation Protection Dosimetry 53, 107-114.
Banko, A.J., Coletti, F., Elkins, C.J., Eaton, J.K., 2016. Oscillatory flow in the human airways from the mouth through several bronchial generations. International Journal of Heat and Fluid Flow 61, 45-57.
Banko, A.J., Coletti, F., Schiavazzi, D., Elkins, C.J., Eaton, J.K., 2015. Three-dimensional inspiratory flow in the upper and central human airways. Experiments in Fluids 56, 1-12.
Baron, P.A., 2001. Measurement of airborne fibers: a review. Ind Health 39, 39-50.
Bayat, S., Le Duc, G., Porra, L., Berruyer, G., Nemoz, C., Monfraix, S., Fiedler, S., Thomlinson, W., Suortti, P., Standertskjöld-Nordenstam, C.G., Sovijärvi, A.R.A., 2001. Quantitative functional lung imaging with synchrotron radiation using inhaled xenon as contrast agent. Physics in Medicine and Biology 46, 3287-3299.
Behr, J., Zimmermann, G., Baumgartner, R., Leuchte, H., Neurohr, C., Brand, P., Herpich, C., Sommerer, K., Seitz, J., Menges, G., Tillmanns, S., Keller, M., 2009. Lung deposition of a liposomal

cyclosporine a inhalation solution in patients after lung transplantation. Journal of Aerosol Medicine and Pulmonary Drug Delivery 22, 121-129.
Bech, M., Bunk, O., David, C., Ruth, R., Rifkin, J., Loewen, R., Feidenhans'l, R., Pfeiffer, F., IUCr, 2009. Hard X-ray phase-contrast imaging with the Compact Light Source based on inverse Compton X-rays. Journal of Synchrotron Radiation 16, 43-47.
Belka, M., Lízal, F., Jedelský, J., Starha, P., Druckmullerova, H., Hopke, P.K., Jicha, M., 2016. Application of image analysis method to detection and counting of glass fibers from filter samples. Aerosol Science and Technology, 00-00.
Benedict, L.H., Nobach, H., Tropea, C., 2000. Estimation of turbulent velocity spectra from laser Doppler data. Measurement Science & Technology 11, 1089-1104.
Bérujon, S., Ziegler, E., Cerbino, R., Peverini, L., 2012. Two-Dimensional X-Ray Beam Phase Sensing. Physical Review Letters 108, 158102.
Bestion, D., Gaviglio, J., Bonnet, J.P., 1983. Comparison between Constant-Current and Constant-Temperature Hot-Wire Anemometers in High-Speed Flows. Rev Sci Instrum 54, 1513-1524.
Bettinardi, V., Castiglioni, I., De Bernardi, E., Gilardi, M.C., 2014. PET quantification: Strategies for partial volume correction. Clinical and Translational Imaging 2, 199-218.
Bettoncelli, G., Blasi, F., Brusasco, V., Centanni, S., Corrado, A., De Benedetto, F., De Michele, F., Di Maria, G.U., Donner, C.F., Falcone, F., Mereu, C., Nardini, S., Pasqua, F., Polverino, M., Rossi, A., Sanguinetti, M., 2014. The Clinical and Integrated Management of Copd an Official Document of Aimar (Interdisciplinary Association for Research in Lung Disease), Aipo (Italian Association of Hospital Pulmonologists), Simer (Italian Society of Respiratory Medicine), Simg (Italian Society of General Medicine). Sarcoidosis Vasc Dif 31, 3-21.
Bezerra, H.G., Costa, M.A., Guagliumi, G., Rollins, A.M., Simon, D.I., 2009. Intracoronary Optical Coherence Tomography: A Comprehensive Review: Clinical and Research Applications. J Am Coll Cardiol Intv 2, 1035-1046.
Blanchard, J.D., 1996. Aerosol Bolus Dispersion and Aerosol-Derived Airway Morphometry: Assessment of Lung Pathology and Response to Therapy, Part 2. Journal of Aerosol Medicine: Deposition, Clearance, and Effects in the Lung 9, 453-476.
Bonse, U., 1965. An X-Ray Interferometer. Appl Phys Lett 6, 155.
Bovendeerd, P.H.M., Vansteenhoven, A.A., Vandevosse, F.N., Vossers, G., 1987. Steady Entry Flow in a Curved Pipe. Journal of Fluid Mechanics 177, 233-246.
Bowes, S.M., Swift, D.L., 1989. DEPOSITION OF INHALED PARTICLES IN THE ORAL AIRWAY DURING ORONASAL BREATHING. Aerosol Science and Technology 11, 157-167.
Branca, R.T., Cleveland, Z.I., Fubara, B., Kumar, C.S., Maronpot, R.R., Leuschner, C., Warren, W.S., Driehuys, B., 2010. Molecular MRI for sensitive and specific detection of lung metastases. Proceedings of the National Academy of Sciences of the United States of America 107, 3693-3697.
Brand, P., Hederer, B., Austen, G., Dewberry, H., Meyer, T., 2008. Higher lung deposition with Respimat® Soft Mist™ Inhaler than HFA-MDI in COPD patients with poor technique. International Journal of COPD 3, 763-770.
Bravin, A., Coan, P., Suortti, P., 2013. X-ray phase-contrast imaging: from pre-clinical applications towards clinics. Physics in Medicine and Biology 58, R1-R35.
Brezinski, M.E., 2006. Optical coherence tomography for identifying unstable coronary plaque. Int.J.Cardiol. 107, 154-165.
Brücker, C., 1996. 3-D scanning particle image velocimetry: technique and application to a spherical cap wake flow. Appl. Sci. Res. 56, 157-179.
Brücker, C., 1998. a Time-Recording Dpiv-Study of the Swirl Switching Effect in a 90° Bend Flow. Proc. 8th International Symposium on Flow Visualization, Sorrento(NA), Italy, 171.171-171.176.
Brunner, E., Haake, M., Kaiser, L., Pines, A., Reimer, J.A., 1999. Gas flow MRI using circulating laser-polarized 129Xe. J Magn Reson 138, 155-159.
Bruun, H.H., 1995. Hot-wire anemometry : principles and signal analysis. Oxford University Press, Oxford ; New York.

Bruun, H.H., Khan, M.A., Alkayiem, H.H., Fardad, A.A., 1988. Velocity Calibration Relationships for Hot-Wire Anemometry. J Phys E Sci Instrum 21, 225-232.
Bu, R., Balakrishnan, S., Iftimia, N., Price, H., Zdanski, C., Oldenburg, A.L., 2017. Airway compliance measured by anatomic optical coherence tomography. Biomedical Optics Express 8, 2195-2209.
Buchsbaum, A., Egger, M., Burzic, I., Koepplmayr, T., Aigner, M., Miethlinger, J., Leitner, M., 2015. Optical coherence tomography based particle image velocimetry (OCT-PIV) of polymer flows. Optics and Lasers in Engineering 69, 40-48.
Calvo, E., García, J.A., García, I., Aísa, L.A., 2009. Errors analysis in the evaluation of particle concentration by PDA on a turbulent two-phase jet: application for cross section and transit time methods. Experiments in Fluids 47, 489-508.
Carnibella, R.P., Kitchen, M.j., Fouras, A., 2014. Single-shot X-ray measurement of alveolar size distributions. SPIE Medical Imaging 9038, 90380V-90380V-90387.
Cimalla, P., Werner, T., Winkler, K., Mueller, C., Wicht, S., Gaertner, M., Mehner, M., Walther, J., Rellinghaus, B., Wittig, D., 2015. Imaging of nanoparticle-labeled stem cells using magnetomotive optical coherence tomography, laser speckle reflectometry, and light microscopy. BIOMEDO 20, 036018-036018.
Clinkenbeard, R.E., Johnson, D.L., Parthasarathy, R., Altan, M.C., Tan, K.H., Park, S.M., Crawford, R.H., 2002. Replication of human tracheobronchial hollow airway models using a selective laser sintering rapid prototyping technique. Aihaj 63, 141-150.
Cloetens, P., Barrett, R., Baruchel, J., Guigay, J.-P., Schlenker, M., 1996. Phase objects in synchrotron radiation hard x-ray imaging. Journal of Physics D: Applied Physics 29, 133-146.
Collier, G.J., Wild, J.M., 2015. In vivo measurement of gas flow in human airways with hyperpolarized gas MRI and compressed sensing. Magn Reson Med 73, 2255-2261.
Corcoran, T.E., Chigier, N., 2000. Characterization of the laryngeal jet using phase Doppler interferometry. Journal of Aerosol Medicine-Deposition Clearance and Effects in the Lung 13, 125-137.
Corcoran, T.E., Chigier, N., 2002. Inertial deposition effects: A study of aerosol mechanics in the trachea using laser Doppler velocimetry and fluorescent dye. Journal of Biomechanical Engineering-Transactions of the Asme 124, 629-637.
Corieri, P., Riethmuller, M.L., 1989. Laser Doppler velocimetry and computer automation to measure low velocities in a pulmonary model. Iciasf 89 Record: International Congress on Instrumentation in Aerospace Simulation Facilities, 226-236.
Darquenne, C., West, J.B., Prisk, G.K., 1998. Deposition and dispersion of 1-mu m aerosol boluses in the human lung: effect of micro- and hypergravity. Journal of Applied Physiology 85, 1252-1259.
David, C., Nöhammer, B., Solak, H.H., Ziegler, E., 2002. Differential x-ray phase contrast imaging using a shearing interferometer. Applied Physics Letters 81, 3287-3289.
de Boer, J.F., Cense, B., Park, B.H., Pierce, M.C., Tearney, G.J., Bouma, B.E., 2003. Improved signal-to-noise ratio in spectral-domain compared with time-domain optical coherence tomography. Opt.Lett. 28, 2067-2069.
de Rochefort, L., Maitre, X., Fodil, R., Vial, L., Louis, B., Isabey, D., Croce, C., Darrasse, L., Apiou, G., Caillibotte, G., Bittoun, J., Durand, E., 2006. Phase-contrast velocimetry with hyperpolarized 3He for in vitro and in vivo characterization of airflow. Magn Reson Med 55, 1318-1325.
de Rochefort, L., Nguyen, T., Brown, R., Spincemaille, P., Choi, G., Weinsaft, J., Prince, M.R., Wang, Y., 2008. In vivo quantification of contrast agent concentration using the induced magnetic field for time-resolved arterial input function measurement with MRI. Med Phys 35, 5328-5339.
DeHaan, W.H., 2002. Mouth-throat deposition with non-ballistic pharmaceutical aerosol inhalation devices. University of Alberta.
Dolovich, M.B., 2009. 18F-fluorodeoxyglucose positron emission tomographic imaging of pulmonary functions, pathology, and drug delivery. Proceedings of the American Thoracic Society 6, 477-485.
Donnelley, M., Morgan, K.S., Awadalla, M., Farrow, N.R., Hall, C., Parsons, D.W., 2017. High-resolution mucociliary transport measurement in live excised large animal trachea using synchrotron X-ray imaging. Respiratory Research accepted 02/05/2017.

Donnelley, M., Morgan, K.S., Siu, K.K.W., Farrow, N.R., Stahr, C.S., Boucher, R.C., Fouras, A., Parsons, D.W., 2014a. Non-invasive airway health assessment: Synchrotron imaging reveals effects of rehydrating treatments on mucociliary transit in-vivo. Scientific reports 4, 146.
Donnelley, M., Morgan, K.S., Siu, K.K.W., Fouras, A., Farrow, N.R., Carnibella, R.P., Parsons, D.W., IUCr, 2014b. Tracking extended mucociliary transport activity of individual deposited particles: longitudinal synchrotron X-ray imaging in live mice. Journal of Synchrotron Radiation 21, 768-773.
Donnelley, M., Morgan, K.S., Siu, K.K.W., Parsons, D.W., 2013. Variability of In Vivo Fluid Dose Distribution in Mouse Airways Is Visualized by High-Speed Synchrotron X-Ray Imaging. www.liebertpub.com 26, 307-316.
Donnelley, M., Parsons, D., Morgan, K.S., Siu, K., 2010. Animals In Synchrotrons: Overcoming Challenges For High-Resolution, Live, Small-Animal Imaging. AIP Conference Proceedings.
Drexler, W., Morgner, U., K„rtner, F.X., Pitris, C., Boppart, S.A., Li, X.D., Ippen, E.P., Fujimoto, J.G., 1999. In vivo ultrahigh-resolution optical coherence tomography. Opt.Lett. 24, 1221-1223.
Dubsky, S., Fouras, A., 2015. Imaging regional lung function: A critical tool for developing inhaled antimicrobial therapies. Advanced drug delivery reviews 85, 100-109.
Dubsky, S., Hooper, S.B., Siu, K.K.W., Fouras, A., 2012. Synchrotron-based dynamic computed tomography of tissue motion for regional lung function measurement. J R Soc Interface 9, 2213-2224.
Dugernier, J., Hesse, M., Vanbever, R., Depoortere, V., Roeseler, J., Michotte, J.B., Laterre, P.F., Jamar, F., Reychler, G., 2017. SPECT-CT Comparison of Lung Deposition using a System combining a Vibrating-mesh Nebulizer with a Valved Holding Chamber and a Conventional Jet Nebulizer: a Randomized Cross-over Study. Pharmaceutical Research 34, 290-300.
Dullenkopf, K., Willmann, M., Wittig, S., Schone, F., Stieglmeier, M., Tropea, C., Mundo, C., 1998. Comparative mass flux measurements in sprays using a patternator and the phase-Doppler technique. Part Part Syst Char 15, 81-89.
Duma, V.F., Lee, K.S., Meemon, P., Rolland, J.P., 2011. Experimental investigations of the scanning functions of galvanometer-based scanners with applications in OCT. Appl.Opt. 50, 5735-5749.
Durst, F., Melling, A., Whitelaw, J.H., 1981. Principles and practice of laser-Doppler anemometry, 2nd ed. Academic Press, London ; New York.
Eberl, S., Chan, H.K., Daviskas, E., Constable, C., Young, I., 2001. Aerosol deposition and clearance measurement: A novel technique using dynamic SPET. European Journal of Nuclear Medicine 28, 1365-1372.
Edwards, C.F., Marx, K.D., 1995. MULTIPOINT STATISTICAL STRUCTURE OF THE IDEAL SPRAY, PART II: EVALUATING STEADINESS USING THE INTERPARTICLE TIME DISTRIBUTION. 5, 457-505.
Elcner, J., Lizal, F., Jedelsky, J., Jicha, M., Chovancova, M., 2016. Numerical investigation of inspiratory airflow in a realistic model of the human tracheobronchial airways and a comparison with experimental results. Biomechanics and Modeling in Mechanobiology 15, 447-469.
Elsinga, G.E., Van Oudheusden, B.W., Scarano, F., 2006. Experimental assessment of Tomographic-PIV accuracy, 13th Int Symp on Applications of Laser Techniques to Fluid Mechanics Lisbon, Portugal, 26-29 June, 2006.
Farag, A., Hammersley, J., Olson, D., Ng, T., 2000. Mechanics of the flow in the small and middle human airways. J Fluid Eng-T Asme 122, 576-584.
Finlay, W.H., Stapleton, K.W., Yokota, J., 1996. On the use of computational fluid dynamics for simulating flow and particle deposition in the human respiratory tract. Journal of Aerosol Medicine-Deposition Clearance and Effects in the Lung 9, 329-341.
Fishler, R., Hofemeier, P., Etzion, Y., Dubowski, Y., Sznitman, J., 2015. Particle dynamics and deposition in true-scale pulmonary acinar models. Scientific Reports 5, 14071-14071.
Fishler, R., Mulligan, M.K., Sznitman, J., 2013. Acinus-on-a-chip: a microfluidic platform for pulmonary acinar flows. J Biomech 46, 2817-2823.
Fishler, R., Ostrovski, Y., Lu, C.-Y., Sznitman, J., 2017. Streamline crossing: An essential mechanism for aerosol dispersion in the pulmonary acinus. Journal of Biomechanics 50, 222-227.
Fleming, J., Conway, J., Majoral, C., Katz, I., Caillibotte, G., Pichelin, M., Montesantos, S., Bennett, M., 2015. Controlled, Parametric, Individualized, 2-D and 3-D Imaging Measurements of Aerosol

Deposition in the Respiratory Tract of Asthmatic Human Subjects for Model Validation. Journal of Aerosol Medicine and Pulmonary Drug Delivery 28, 432-451.
Fleming, J.S., Conway, J., Majoral, C., Tossici-Bolt, L., Katz, I., Caillibotte, G., Perchet, D., Pichelin, M., Muellinger, B., Martonen, T., Kroneberg, P., Apiou-Sbirlea, G., 2011. The use of combined single photon emission computed tomography and X-ray computed tomography to assess the fate of inhaled aerosol. Journal of Aerosol Medicine and Pulmonary Drug Delivery 24, 49-60.
Forbes, B., Danani, A., Borchard, G., Kassinos, S., 2016. Introducing European COST Action—Siminhale. Inhalation.
Förster, E., Goetz, K., Zaumseil, P., 1980. Double crystal diffractometry for the characterization of targets for laser fusion experiments. Crystal Research and Technology 15, 937-945.
Fouras, A., Allison, B.J., Kitchen, M.j., Dubsky, S., Nguyen, J., Hourigan, K., Siu, K.K.W., Lewis, R.A., Wallace, M.J., Hooper, S.B., 2012. Altered Lung Motion is a Sensitive Indicator of Regional Lung Disease. Annals of Biomedical Engineering 40, 1160-1169.
Fouras, A., Dubsky, S., 2015. The Role of Functional Lung Imaging in the Improvement of Pulmonary Drug Delivery. John Wiley & Sons, Ltd, Chichester, UK.
Fresconi, F.E., Prasad, A.K., 2007. Secondary velocity fields in the conducting airways of the human lung. Journal of Biomechanical Engineering-Transactions of the Asme 129, 722-732.
Gemci, T., Corcoran, T.E., Chigier, N., 2002. A numerical and experimental study of spray dynamics in a simple throat model. Aerosol Science and Technology 36, 18-38.
Gillings, N., 2013. Radiotracers for positron emission tomography imaging. Magnetic Resonance Materials in Physics, Biology and Medicine 26, 149-158.
Girardin, M., Bilgen, E., Arbour, P., 1983. Experimental-Study of Velocity-Fields in a Human Nasal Fossa by Laser Anemometry. Ann Oto Rhinol Laryn 92, 231-236.
Gleich, B., Weizenecker, R., 2005. Tomographic imaging using the nonlinear response of magnetic particles. Nature 435, 1214-1217.
Gracia, R., Marradi, M., Cossío, U., Benito, A., Pérez-San Vicente, A., Gómez-Vallejo, V., Grande, H.J., Llop, J., Loinaz, I., 2017. Synthesis and functionalization of dextran-based single-chain nanoparticles in aqueous media. Journal of Materials Chemistry B 5, 1143-1147.
Grgic, B., Finlay, W.H., Heenan, A.F., 2004. Regional aerosol deposition and flow measurements in an idealized mouth and throat. Journal of Aerosol Science 35, 21-32.
Grombe, R., Kirsten, L., Mehner, M., Linsinger, T.P., Koch, E., 2016. Improved non-invasive Optical Coherence Tomography detection of different engineered nanoparticles in food-mimicking matrices. Food Chem. 212, 571-575.
Grosse, S., Schroder, W., Klaas, M., Klockner, A., Roggenkamp, J., 2007. Time resolved analysis of steady and oscillating flow in the upper human airways. Experiments in Fluids 42, 955-970.
Guilmette, L.A., Wicks, J.D., Wolff, R.K., 1989. Morphometry of human nasal airways in vivo using magnetic resonance imaging. Journal of Aerosol Medicine and Pulmonary Drug Delivery - ISSN 1941-2711 2, 365-377.
Guilmette, R.A., Gagliano, T.J., 1994. Construction of a Model of Human Nasal Airways Using Invivo Morphometric Data. Inhaled Particles Vii, 69-75.
Hahn, I., Scherer, P.W., Mozell, M.M., 1993. Velocity Profiles Measured for Air-Flow through a Large-Scale Model of the Human Nasal Cavity. Journal of Applied Physiology 75, 2273-2287.
Haindl, R., Trasischker, W., Wartak, A., Baumann, B., Pircher, M., Hitzenberger, C.K., 2016. Total retinal blood flow measurement by three beam Doppler optical coherence tomography. Biomedical Optics Express 7, 287-301.
Heenan, A.F., Matida, E., Pollard, A., Finlay, W.H., 2003. Experimental measurements and computational modeling of the flow field in an idealized human oropharynx. Experiments in Fluids 35, 70-84.
Hellbach, K., Yaroshenko, A., Meinel, F.G., Yildirim, A.Ö., Conlon, T.M., Bech, M., Mueller, M., Velroyen, A., Notohamiprodjo, M., Bamberg, F., Auweter, S., Reiser, M., Eickelberg, O., Pfeiffer, F., 2015. In Vivo Dark-Field Radiography for Early Diagnosis and Staging of Pulmonary Emphysema. Investigative Radiology 50, 430-435.

Heraty, K.B., Laffey, J.G., Quinlan, N.J., 2008. Fluid dynamics of gas exchange in high-frequency oscillatory ventilation: In vitro investigations in idealized and anatomically realistic airway bifurcation models. Annals of Biomedical Engineering 36, 1856-1869.
Hetsroni, G., 1989. Particles Turbulence Interaction. Int J Multiphas Flow 15, 735-746.
Heyder, J., Gebhart, J., Roth, C., Stahlhofen, W., Stuck, B., Tarroni, G., DeZaiacomo, T., Formignani, M., Melandri, C., Prodi, V., 1978. Intercomparison of lung deposition data for aerosol particles. Journal of Aerosol Science 9, 147-155.
Hoegger, M.J., Awadalla, M., Namati, E., Itani, O.A., Fischer, A.J., Tucker, A.J., Adam, R.J., McLennan, G., Hoffman, E.A., Stoltz, D.A., Welsh, M.J., 2014. Assessing mucociliary transport of single particles in vivo shows variable speed and preference for the ventral trachea in newborn pigs. Proceedings of the National Academy of Sciences 111, 2355-2360.
Holbrook, L.T., Longest, P.W., 2013. Validating CFD predictions of highly localized aerosol deposition in airway models: In vitro data and effects of surface properties. Journal of Aerosol Science 59, 6-21.
Hooper, S.B., Kitchen, M.J., Wallace, M.J., Yagi, N., Uesugi, K., Morgan, M.J., Hall, C., Siu, K.K.W., Williams, I.M., Siew, M., Irvine, S.C., Pavlov, K., Lewis, R.A., 2007. Imaging lung aeration and lung liquid clearance at birth. Faseb J 21, 3329-3337.
Hopkins, L.M., Kelly, J.T., Wexler, A.S., Prasad, A.K., 2000. Particle image velocimetry measurements in complex geometries. Experiments in Fluids 29, 91-95.
Horsfield, K., Cumming, G., 1967. Angles of branching and diameters of branches in the human bronchial tree. Bulletin of Mathematical Biology 29, 245-259.
Horsfield, K., Cumming, G., 1968. Morphology of the bronchial tree in man. Journal of applied physiology 24, 373-383.
Horsfield, K., Dart, G., Olson, D.E., Filley, G.F., Cumming, G., 1971. Models of the human bronchial tree. Journal of applied physiology: respiratory, environmental and exercise physiology 31, 207-217.
Huang, B.K., Gamm, U.A., Bhandari, V., Khokha, M.K., Choma, M.A., 2015. Three-dimensional, three-vector-component velocimetry of cilia-driven fluid flow using correlation-based approaches in optical coherence tomography. Biomedical Optics Express 6, 3515-3538.
Huang, D., Swanson, E.A., Lin, C.P., Schuman, J.S., Stinson, W.G., Chang, W., Hee, M.R., Flotte, T., Gregory, K., Puliafito, C.A., Fujimoto, J.G., 1991. Optical Coherence Tomography. Science 254, 1178-1181.
Chang, H.K., Elmasry, O.A., 1982. A MODEL STUDY OF FLOW DYNAMICS IN HUMAN CENTRAL AIRWAYS .1. AXIAL VELOCITY PROFILES. Respiration Physiology 49, 75-95.
Chen, C., Cheng, K.H.Y., Jakubovic, R., Jivraj, J., Ramjist, J., Deorajh, R., Gao, W., Barnes, E., Chin, L., Yang, V.X.D., 2017. High speed, wide velocity dynamic range Doppler optical coherence tomography (Part V): Optimal utilization of multi-beam scanning for Doppler and speckle variance microvascular imaging. Opt.Express 25, 7761-7777.
Cheng, K.H., Cheng, Y.S., Yeh, H.C., Swift, D.L., 1997. Measurements of airway dimensions and calculation of mass transfer characteristics of the human oral passage. Journal of Biomechanical Engineering-Transactions of the Asme 119, 476-482.
Cheng, Y.S., Zhou, Y., Chen, B.T., 1999. Particle deposition in a cast of human oral airways. Aerosol Science and Technology 31, 286-300.
Cheng, Y.S., Zhou, Y., Su, W.C., 2015. Deposition of Particles in Human Mouth-Throat Replicas and a USP Induction Port. Journal of Aerosol Medicine and Pulmonary Drug Delivery 28, 147-155.
Choi, J., Tawhai, M.H., Hoffman, E.A., Lin, C.L., 2009. On intra- and intersubject variabilities of airflow in the human lungs. Physics of Fluids 21, 17.
Choma, M., Sarunic, M., Yang, C., Izatt, J., 2003. Sensitivity advantage of swept source and Fourier domain optical coherence tomography. Opt.Express 11, 2183-2189.
Ingal, V.N., Beliaevskaya, E.A., 1995. X-ray plane-wave topography observation of the phase contrast from a non-crystalline object. Journal of Physics D: Applied Physics 28, 2314-2317.
Isabey, D., Chang, H.K., 1982. A MODEL STUDY OF FLOW DYNAMICS IN HUMAN CENTRAL AIRWAYS .2. SECONDARY FLOW VELOCITIES. Respiration Physiology 49, 97-113.

Islam, M.N., Gomer, H., Sacks, S., 2017. Comparison of dimensional accuracies of stereolithography and powder binder printing. International Journal of Advanced Manufacturing Technology 88, 3077-3087.
Janke, T., Bauer, K., 2016. Development of a 3D-PTV algorithm for the investigation of turbulent flow structures in the upper human bronchial tree., 18th International Symposium on Applications of Laser Techniques to Fluid Mechanics,.
Jayaraju, S.T., Brouns, M., Lacor, C., Belkassem, B., Verbanck, S., 2008. Large eddy and detached eddy simulations of fluid flow and particle deposition in a human mouth–throat. Journal of Aerosol Science 39, 862-875.
Jedelsky, J., Lizal, F., Jicha, M., 2012. Characteristics of turbulent particle transport in human airways under steady and cyclic flows. International Journal of Heat and Fluid Flow 35, 84-92.
Jensen, K.D., 2004. Flow measurement. J. of the Braz. Soc. of Mech. Sci. & Eng. 26, 400-419.
Johnstone, A., Uddin, M., Pollard, A., Heenan, A., Finlay, W.H., 2004. The flow inside an idealised form of the human extra-thoracic airway. Experiments in Fluids 37, 673-689.
Jonas, S., Bhattacharya, D., Khokha, M.K., Choma, M.A., 2011. Microfluidic characterization of cilia-driven fluid flow using optical coherence tomography-based particle tracking velocimetry. Biomedical Optics Express 2, 2022-2034.
Jung, W., McCormick, D.T., Zhang, J., Wang, L., Tien, N.C., Chen, Z., 2006. Three-dimensional endoscopic optical coherence tomography by use of a two-axis microelectromechanical scanning mirror. Appl.Phys.Lett. 88, 163901.
Kalkman, J., Sprik, R., van Leeuwen, T.G., 2010. Path-length-resolved diffusive particle dynamics in spectral-domain optical coherence tomography. Physical Review Letters 105, 198302.
Kelly, J.T., Asgharian, B., Kimbell, J.S., Wong, B.A., 2004a. Particle deposition in human nasal airway replicas manufactured by different methods. Part I: Inertial regime particles. Aerosol Science and Technology 38, 1063-1071.
Kelly, J.T., Asgharian, B., Kimbell, J.S., Wong, B.A., 2004b. Particle deposition in human nasal airway replicas manufactured by different methods. Part II: Ultrafine particles. Aerosol Science and Technology 38, 1072-1079.
Kerekes, A., Nagy, A., Veres, M., Rigo, I., Farkas, A., Czitrovszky, A., 2016. In vitro and in silico (IVIS) flow characterization in an idealized human airway geometry using laser Doppler anemometry and computational fluid dynamics techniques. Measurement 90, 144-150.
Kesavanathan, J., Swift, D.L., 1998. Human nasal passage particle deposition: The effect of particle size, flow rate, and anatomical factors. Aerosol Science and Technology 28, 457-463.
Kim, C.S., Fisher, D.M., 1999. Deposition of aerosol particles in successively bifurcating airways models. Aerosol Science and Technology 31, 198-220.
Kim, C.S., Hu, S.C., DeWitt, P., Gerrity, T.R., 1996. Assessment of regional deposition of inhaled particles in human lungs by serial bolus delivery method. Journal of Applied Physiology 81, 2203-2213.
Kim, C.S., Iglesias, A.J., 1989. Deposition of Inhaled Particles in Bifurcating Airway Models: I. Inspiratory Deposition. JOURNAL OF AEROSOL MEDICINE 2, 14.
Kim, C.S., Kang, T.C., 1997. Comparative measurement of lung deposition of inhaled fine particles in normal subjects and patients with obstructive airway disease. American journal of respiratory and critical care medicine 155, 899-905.
Kippax, P., Krarup, H., Suman, J., 2004. Applications for droplet sizing: Manual versus automated actuation of nasal sprays. Pharm Technol, 30–39.
Kirsten, L., Domaschke, T., Schneider, C., Walther, J., Meissner, S., Hampel, R., Koch, E., 2015. Visualization of dynamic boiling processes using high-speed optical coherence tomography. Experiments in Fluids 56.
Kirsten, L., Gaertner, M., Schnabel, C., Meissner, S., Koch, E., 2013. Four-dimensional imaging of murine subpleural alveoli using high-speed optical coherence tomography. Journal Of Biophotonics 6, 148-152.

Kitchen, M.j., Buckley, G.A., Leong, A.F.T., 2015. X-ray specks: low dose in vivo imaging of lung structure and function. Physics in medicine ….
Kitchen, M.j., Paganin, D.M., Lewis, R.A., Yagi, N., 2004. On the origin of speckle in x-ray phase contrast images of lung tissue. Physics in medicine ….
Knopp, T., Conolly, S.M., Buzug, T.M., 2017. Recent progress in magnetic particle imaging: from hardware to preclinical applications. Physics in Medicine and Biology 62, E4-E7.
Kohlhaufl, M., Brand, P., Selzer, T., Scheuch, G., Meyer, T., Weber, N., Schulz, H., Haussinger, K., Heyder, J., 1998. Diagnosis of emphysema in patients with chronic bronchitis: a new approach. European Respiratory Journal 12, 793-798.
Kolanjiyil, A.V., Kleinstreuer, C., 2013. Nanoparticle Mass Transfer From Lung Airways to Systemic Regions-Part I: Whole-Lung Aerosol Dynamics. Journal of Biomechanical Engineering-Transactions of the Asme 135.
Koptyug, I.I., Altobelli, S.A., Fukushima, E., Matveev, A.V., Sagdeev, R.Z., 2000. Thermally polarized (1)H NMR microimaging studies of liquid and gas flow in monolithic catalysts. J Magn Reson 147, 36-42.
Koullapis, P.G., Hofemeier, P., Sznitman, J., Kassinos, S.C., 2017a. An efficient Computational Fluid-Particle Dynamics method to predict deposition in a simplified approximation of the deep lung. European Journal of Pharmaceutical Sciences.
Koullapis, P.G., Kassinos, S.C., Muela, J., Segarra, C., Rigola, J., Lehmkuhl, O., Cui, Y., M. Sommerfeld, J. Elcner, M. Jicha, I. Saveljic, N. Filipovic, F. Lizal, Nicolaou, L., 2017b. In silico methods for regional aerosol deposition in the human airways: A critical review and the SimInhale benchmark case. European Journal of Pharmaceutical Sciences.
Kwak, Y., Nam, S., Akcakaya, M., Basha, T.A., Goddu, B., Manning, W.J., Tarokh, V., Nezafat, R., 2013. Accelerated aortic flow assessment with compressed sensing with and without use of the sparsity of the complex difference image. Magn Reson Med 70, 851-858.
Landahl, H.D., Tracewell, T.N., Lassen, W.H., 1951. ON THE RETENTION OF AIR-BORNE PARTICULATES IN THE HUMAN LUNG .2. Ama Archives of Industrial Hygiene and Occupational Medicine 3, 359-366.
Larsson, D.H., Takman, P.A.C., Lundström, U., Burvall, A., Hertz, H.M., 2011. A 24 keV liquid-metal-jet x-ray source for biomedical applications. Rev Sci Instrum 82, 123701.
Lee Ventola, C., 2014. Medical applications for 3D printing: Current and projected uses. P and T 39, 704-711.
Lee, W.J., Kawahashi, M., Hirahara, H., 2006. Experimental analysis of pendelluft flow generated by HFOV in a human airway model. Physiological Measurement 27, 661-674.
Leitgeb, R., Hitzenberger, C., Fercher, A., 2003. Performance of fourier domain vs. time domain optical coherence tomography. Opt.Express 11, 889-894.
Lemonis, G., 1997. Three-dimensional measurement of velocity, velocity gradients and related properties in turbulent flows. Aerospace Science and Technology 1, 453-461.
Li, Z., Conti, P.S., 2010. Radiopharmaceutical chemistry for positron emission tomography. Advanced Drug Delivery Reviews 62, 1031-1051.
Liaw, C.Y., Guvendiren, M., 2017. Current and emerging applications of 3D printing in medicine. Biofabrication 9.
Lieber, B., Zhao, Y., 1998. Oscillatory flow in a symmetric bifurcation airway model. Annals of Biomedical Engineering 26, 821-830.
Lippmann, M., Yeates, D.B., Albert, R.E., 1980. DEPOSITION, RETENTION, AND CLEARANCE OF INHALED PARTICLES. British Journal of Industrial Medicine 37, 337-362.
Liu, H., 2000. Science and engineering of droplets : fundamentals and applications. Noyes Publications ;

William Andrew Pub., Park Ridge, N.J.

Norwich, N.Y.

Liu, X., Yan, W., Liu, Y., Choy, Y.S., Wei, Y., 2016. Numerical Investigation of Flow Characteristics in the Obstructed Realistic Human Upper Airway. Computational and Mathematical Methods in Medicine 2016, 10.
Lizal, F., Belka, M., Adam, J., Jedelsky, J., Jicha, M., 2015. A method for in vitro regional aerosol deposition measurement in a model of the human tracheobronchial tree by the positron emission tomography. Proceedings of the Institution of Mechanical Engineers Part H-Journal of Engineering in Medicine 229, 750-757.
Lizal, F., Elcner, J., Hopke, P.K., Jedelsky, J., Jicha, M., 2012. Development of a realistic human airway model. Proceedings of the Institution of Mechanical Engineers Part H-Journal of Engineering in Medicine 226, 197-207.
Loira-Pastoriza, C., Todoroff, J., Vanbever, R., 2014. Delivery strategies for sustained drug release in the lungs. Advanced Drug Delivery Reviews 75, 81-91.
Longest, P.W., Holbrook, L.T., 2012. In silico models of aerosol delivery to the respiratory tract - Development and applications. Advanced Drug Delivery Reviews 64, 296-311.
Longest, P.W., Tian, G., Delvadia, R., Hindle, M., 2012. Development of a Stochastic Individual Path (SIP) Model for Predicting the Deposition of Pharmaceutical Aerosols: Effects of Turbulence, Polydisperse Aerosol Size, and Evaluation of Multiple Lung Lobes. Aerosol Science and Technology 46, 1271-1285.
Longo, R., 2016. Current studies and future perspectives of synchrotron radiation imaging trials in human patients. Nuclear Instruments and Methods in Physics Research Section A: Accelerators, Spectrometers, Detectors and Associated Equipment 809, 13-22.
Lorenser, D., Yang, X., Kirk, R.W., Quirk, B.C., McLaughlin, R.A., Sampson, D.D., 2011. Ultrathin side-viewing needle probe for optical coherence tomography. Opt.Lett. 36, 3894-3896.
Lovrić, G., 2015. In vivo study of lung physiology with dynamic synchrotron-based tomographic microscopy.
Lu, C.D., Kraus, M.F., Potsaid, B., Liu, J.J., Choi, W., Jayaraman, V., Cable, A.E., Hornegger, J., Duker, J.S., Fujimoto, J.G., 2014. Handheld ultrahigh speed swept source optical coherence tomography instrument using a MEMS scanning mirror. Biomedical Optics Express 5, 293-311.
Luan, X., Campanucci, V.A., Nair, M., Yilmaz, O., Belev, G., Machen, T.E., Chapman, D., Ianowski, J.P., 2014. Pseudomonas aeruginosa triggers CFTR-mediated airway surface liquid secretion in swine trachea. Proceedings of the National Academy of Sciences 111, 12930-12935.
Lustig, M., Donoho, D., Pauly, J.M., 2007. Sparse MRI: The application of compressed sensing for rapid MR imaging. Magn Reson Med 58, 1182-1195.
Martin, A.R., Thompson, R.B., Finlay, W.H., 2008. MRI measurement of regional lung deposition in mice exposed nose-only to nebulized superparamagnetic iron oxide nanoparticles. J Aerosol Med Pulm Drug Deliv 21, 335-342.
Marx, K.D., Edwards, C.F., Chin, W.K., 1994. Limitations of the Ideal Phase-Doppler System - Extension to Spatially and Temporally Inhomogeneous Particle Flows. Atomization Spray 4, 1-40.
McLaughlin, D., Tiederman, W., 1973. Biasing Correction for Individual Realization of Laser Anemometer Measurements in Turbulent Flows. Physics of Fluids 16, 2082-2088.
McLaughlin, R.A., Yang, X.J., Quirk, B.C., Lorenser, D., Kirk, R.W., Noble, P.B., Sampson, D.D., 2012. Static and dynamic imaging of alveoli using optical coherence tomography needle probes. Journal of applied physiology: respiratory, environmental and exercise physiology 113, 967-974.
Meissner, S., Knels, L., Koch, E., 2009a. Improved three-dimensional Fourier domain optical coherence tomography by index matching in alveolar structures. BIOMEDO 14, 064037.
Meissner, S., Knels, L., Schnabel, C., Koch, T., Koch, E., 2010a. Three-dimensional Fourier domain optical coherence tomography in vivo imaging of alveolar tissue in the intact thorax using the parietal pleura as a window. BIOMEDO 15, 016030.
Meissner, S., Muller, G., Walther, J., Morawietz, H., Koch, E., 2009b. In-vivo Fourier domain optical coherence tomography as a new tool for investigation of vasodynamics in the mouse model. BIOMEDO 14, 034027.

Meissner, S., Tabuchi, A., Mertens, M., Kuebler, W.M., Koch, E., 2010b. Virtual four-dimensional imaging of lung parenchyma by optical coherence tomography in mice. BIOMEDO 15, 036016.
Melling, A., 1997. Tracer particles and seeding for particle image velocimetry. Measurement Science and Technology 8, 1406-1416.
Menon, A.S., Weber, M.E., Chang, H.K., 1984. MODEL STUDY OF FLOW DYNAMICS IN HUMAN CENTRAL AIRWAYS .3. OSCILLATORY VELOCITY PROFILES. Respiration Physiology 55, 255-275.
Miller, P.W., Long, N.J., Vilar, R., Gee, A.D., 2008. Synthesis of11C, 18F, 15O, and 13N radiolabels for positron emission tomography. Angewandte Chemie - International Edition 47, 8998-9033.
Mills, P.H., Wu, Y.J., Ho, C., Ahrens, E.T., 2008. Sensitive and automated detection of iron-oxide-labeled cells using phase image cross-correlation analysis. Magn Reson Imaging 26, 618-628.
Mirsadraee, S., van Beek, E.J.R., 2015. Functional Imaging Computed Tomography and MRI. Clin. Chest Med. 36, 349-+.
Mitchell, J., Bauer, R., Lyapustina, S., Tougas, T., Glaab, V., 2011. Non-impactor-Based Methods for Sizing of Aerosols Emitted from Orally Inhaled and Nasal Drug Products (OINDPs). AAPS PharmSciTech 12, 965.
Moerer, O., Hahn, G., Quintel, M., 2011. Lung impedance measurements to monitor alveolar ventilation. Curr Opin Crit Care 17, 260-267.
Moller, H.E., Chen, X.J., Saam, B., Hagspiel, K.D., Johnson, G.A., Altes, T.A., de Lange, E.E., Kauczor, H.U., 2002. MRI of the lungs using hyperpolarized noble gases. Magn Reson Med 47, 1029-1051.
Morais, G.R., Paulo, A., Santos, I., 2012. Organometallic complexes for SPECT imaging and/or radionuclide therapy. Organometallics 31, 5693-5714.
Morgan, K.S., Donnelley, M., Farrow, N.R., Fouras, A., Yagi, N., Suzuki, Y., Takeuchi, A., Uesugi, K., Boucher, R.C., Siu, K.K.W., Parsons, D.W., 2014. In VivoX-Ray Imaging Reveals Improved Airway Surface Hydration after a Therapy Designed for Cystic Fibrosis. American journal of respiratory and critical care medicine 190, 469-472.
Morgan, K.S., Paganin, D.M., Siu, K.K.W., 2011. Quantitative single-exposure x-ray phase contrast imaging using a single attenuation grid. Optics express 19, 19781-19789.
Morgan, K.S., Paganin, D.M., Siu, K.K.W., 2012. X-ray phase imaging with a paper analyzer. Applied Physics Letters 100, 124102.
Morgan, K.S., Petersen, T.C., Donnelley, M., Farrow, N.R., Parsons, D.W., Paganin, D.M., 2016. Capturing and visualizing transient X-ray wavefront topological features by single-grid phase imaging. Optics express 24, 24435-24450.
Mosbah, K., Ruiz-Cabello, J., Berthezene, Y., Cremillieux, Y., 2008. Aerosols and gaseous contrast agents for magnetic resonance imaging of the lung. Contrast Media Mol Imaging 3, 173-190.
Myojo, T., 1987. Deposition of Fibrous Aerosol in Model Bifurcating Tubes. Journal of Aerosol Science 18, 337-&.
Myojo, T., 1990. The Effect of Length and Diameter on the Deposition of Fibrous Aerosol in a Model Lung Bifurcation. Journal of Aerosol Science 21, 651-659.
Namati, E., Warger, W.C., Unglert, C.I., Eckert, J.E., Hostens, J., Bouma, B.E., Tearney, G.J., 2013. Four-dimensional visualization of subpleural alveolar dynamics in vivo during uninterrupted mechanical ventilation of living swine. Biomedical Optics Express 4, 2492-2506.
Negus, C.R., Drain, L.E., 1982. Mie Calculations of the Scattered-Light from a Spherical-Particle Traversing a Fringe Pattern Produced by 2 Intersecting Laser-Beams. J Phys D Appl Phys 15, 375-402.
Nemes, A., Jalal, S., Moortele, T.V.d., Coletti, F., 2016. Oscillatory flow in a human airway model: MRV and PIV, 18th International Symposium on the Application of Laser and Imaging Techniques to Fluid Mechanics, LISBON | PORTUGAL, JULY 4 – 7, 2016, pp. 345-354.
Newman, S., Fleming, J., 2011. Challenges in assessing regional distribution of inhaled drug in the human lungs. Expert Opinion on Drug Delivery 8, 841-855.
NIOSH, 1994. Fibers, Method 7400 issue #2 (8/15/94), in NIOSH manual of analytical methods, in: Health, N.I.f.O.S.a. (Ed.). NIOSH, Cincinaty, USA.
Nordlund, M., Belka, M., Kuczaj, A., Lizal, F., Jedelsky, J., Elcner, J., Jicha, M., Sauser, Y., Le Bouhellec, S., Cosandey, S., Majeed, S., Vuillaume, G., Peitsch, M., Hoeng, J., 2017. Multicomponent aerosol

particle deposition in a realistic cast of the human upper respiratory tract. Inhalation toxicology in print.
Oakes, J.M., Scadeng, M., Breen, E.C., Prisk, G.K., Darquenne, C., 2013. Regional distribution of aerosol deposition in rat lungs using magnetic resonance imaging. Ann Biomed Eng 41, 967-978.
Oldenburg, A.L., Blackmon, R.L., Sierchio, J.M., 2016. Magnetic and Plasmonic Contrast Agents in Optical Coherence Tomography. IEEE Journal of Selected Topics in Quantum Electronics 22, 133-145.
Oldham, M.J., 2006. Challenges in validating CFD-Derived inhaled aerosol deposition predictions. Inhalation Toxicology 18, 781-786.
Olivo, A., Castelli, E., 2014. X-ray phase contrast imaging: From synchrotrons to conventional sources. Rivista Del Nuovo Cimento.
Olivo, A., Speller, R., 2007. A coded-aperture technique allowing x-ray phase contrast imaging with conventional sources. Applied Physics Letters 91, 074106.
Olson, D.E., Sudlow, M.F., Horsfield, K., Filley, G.F., 1973. Convective Patterns of Flow during Inspiration. Arch Intern Med 131, 51-57.
Olsson, B., Borgstrom, L., Lundback, H., Svensson, M., 2013. Validation of a General In Vitro Approach for Prediction of Total Lung Deposition in Healthy Adults for Pharmaceutical Inhalation Products. Journal of Aerosol Medicine and Pulmonary Drug Delivery 26, 355-369.
Or, D.Y.L., Karmakar, M.K., Lam, G.C.S., Hui, J.W.Y., Li, J.W., Chen, P.P., 2013. Multiplanar 3D ultrasound imaging to assess the anatomy of the upper airway and measure the subglottic and tracheal diameters in adults. Brit J Radiol 86.
Parsons, D.W., Morgan, K.S., Donnelley, M., Fouras, A., Crosbie, J., Williams, I., Boucher, R.C., Uesugi, K., Yagi, N., Siu, K.K.W., 2008. High-resolution visualization of airspace structures in intact mice via synchrotron phase-contrast X-ray imaging (PCXI). Journal of Anatomy 213, 217-227.
Paulus, D.H., Quick, H.H., 2016. Hybrid Positron Emission Tomography/Magnetic Resonance Imaging: Challenges, Methods, and State of the Art of Hardware Component Attenuation Correction. Investigative Radiology 51, 624-634.
Peattie, R.A., Schwarz, W., 1998. Experimental investigation of oscillatory flow through a symmetrically bifurcating tube. Journal of Biomechanical Engineering-Transactions of the Asme 120, 584-593.
Pépin, A., Daouk, J., Bailly, P., Hapdey, S., Meyer, M.E., 2014. Management of respiratory motion in PET/computed tomography: The state of the art. Nuclear Medicine Communications 35, 113-122.
Pfeiffer, F., Weitkamp, T., Bunk, O., David, C., 2006. Phase retrieval and differential phase-contrast imaging with low-brilliance X-ray sources. Nature physics 2, 258-261.
Phalen, R.F., Yeh, H.-C., Raabe, O.G., Velasquez, D.J., 1973. Casting the lungs in-situ. The Anatomical Record 177, 255-263.
Pratt, E.C., Shaffer, T.M., Grimm, J., 2016. Nanoparticles and radiotracers: advances toward radionanomedicine. Wiley Interdisciplinary Reviews: Nanomedicine and Nanobiotechnology 8, 872-890.
Prezado, Y., Vautrin, M., Martínez Rovira, I., Bravin, A., Estève, F., Elleaume, H., Berkvens, P., Adam, J.F., 2011. Dosimetry protocol for the forthcoming clinical trials in synchrotron stereotactic radiation therapy (SSRT). Medical Physics 38, 1709-1717.
Price, E.W., Orvig, C., 2014. Matching chelators to radiometals for radiopharmaceuticals. Chemical Society Reviews 43, 260-290.
Prokop, R.M., Finlay, W.H., Stapleton, K.W., 1995. An in-Vitro Technique for Calculating the Regional Dosages of Drugs Delivered by an Ultrasonic Nebulizer. Journal of Aerosol Science 26, 847-860.
Quirk, B.C., McLaughlin, R.A., Pagnozzi, A.M., Kennedy, B.F., Noble, P.B., Sampson, D.D., 2014. Optofluidic needle probe integrating targeted delivery of fluid with optical coherence tomography imaging. Opt.Lett. 39, 2888-2891.
Raabe, O.G., Yeh, H.C., Schum, G.M., Phalen, R.F., 1976. Tracheobronchial geometry: Human, dog, rat, hamster. Lovelace Foundation Report, Albuquerque, NM, http://mae.ucdavis.edu/wexler/lungs/LF53-Raabe/ (accessed January 2010).

Ramuzat, A., Day, S., Riethmuller, M.L., 1998. Steady and unsteady LDV and PIV investigations of flow within 2D lung bifurcations model, 9th International Symposium on Applications of Laser Techniques to Fluid Mechanics, Lisbon, Portugal.
Ramuzat, A., Riethmuller, M.L., 1997. Application of 2D Laser Doppler Velocimetry to biomedical flows experimental investigations of flows within lung bifurcations, 7th International Conference Laser Anemometry Advances and Applications, Karlsruhe, Germany.
Ramuzat, A., Riethmuller, M.L., 2002. PIV investigations of oscillationg flows with a 3D lung multiple bifurcation model, 11th Int. Symp. on Appl. of Laser Techniques to Fluid Flows, pp. 8-11.
Riera, J., Perez, P., Cortes, J., Roca, O., Masclans, J.R., Rello, J., 2013. Effect of High-Flow Nasal Cannula and Body Position on End-Expiratory Lung Volume: A Cohort Study Using Electrical Impedance Tomography. Respiratory care 58, 589-596.
Robart, D., Breuer, S., Reckers, W., Kneer, R., 2001. Assessment of pulsed gasoline fuel sprays by means of qualitative and quantitative laser-based diagnostic methods. Part Part Syst Char 18, 179-189.
Roisman, I.V., Tropea, C., 2001. Flux measurements in sprays using phase Doppler techniques. Atomization Spray 11, 667-699.
Roth, A.P., Lange, C.F., Finlay, W.H., 2003. The effect of breathing pattern on nebulizer drug delivery. Journal of Aerosol Medicine: Deposition, Clearance, and Effects in the Lung 16, 325-339.
Roth, K.W., 1995. Deposition and dispersion of inertial aerosols in secondary and turbulent flow structures, Mechanical Engineering. Massachusetts Institute of Technology.
Salmi, M., Paloheimo, K.S., Tuomi, J., Wolff, J., Makitie, A., 2013. Accuracy of medical models made by additive manufacturing (rapid manufacturing). J. Cranio-MaxilloFac. Surg. 41, 603-609.
Sankar, S.V., Weber, B.J., Kamemoto, D.Y., Bachalo, W.D., 1991. Sizing Fine Particles with the Phase Doppler Interferometric-Technique. Appl Optics 30, 4914-4920.
Santolaya, J.L., Garcia, J.A., Calvo, E., Cerecedo, L.M., 2013. Effects of droplet collision phenomena on the development of pressure swirl sprays. Int J Multiphas Flow 56, 160-171.
Sarracanie, M., Grebenkov, D., Sandeau, J., Coulibaly, S., Martin, A.R., Hill, K., Perez Sanchez, J.M., Fodil, R., Martin, L., Durand, E., Caillibotte, G., Isabey, D., Darrasse, L., Bittoun, J., Maitre, X., 2015. Phase-contrast helium-3 MRI of aerosol deposition in human airways. NMR Biomed 28, 180-187.
Scarano, F., 2013. Tomographic PIV: principles and practice. Measurement Science and Technology 24, 012001-012001.
Sera, T., Yokota, H., Tanaka, G., Uesugi, K., Yagi, N., Schroter, R.C., 2013. Murine pulmonary acinar mechanics during quasi-static inflation using synchrotron refraction-enhanced computed tomography. Journal of Applied Physiology 115, 219-228.
Schanz, D., Schröder, A., Gesemann, S., 2014. 'Shake The Box' - a 4D PTV algorithm: Accurate and ghostless reconstruction of Lagrangian tracks in densely seeded flows. 17th International Symposium on Applications of Laser Techniques to Fluid Mechanics, 7-10.
Schanz, D., Schröder, A., Gesemann, S., Michaelis, D., Wieneke, B., 2013. ‘ Shake The Box ’: A highly efficient and accurate Tomographic Particle Tracking Velocimetry (TOMO-PTV) method using prediction of particle positions. 10th International Symposium on Particle Image Velocimetry - PIV13. Delft, The Netherlands, July 1-3., 1-13.
Scheuch, G., 1994. Particle recovery from human conducting airways after shallow aerosol bolus inhalation. Journal of Aerosol Science 25, 957-973.
Scheuch, G., Stahlhofen, W., Fang, C.P., Lippmann, M., 1993. 32 O 02 Aerosol recovery after bolus inhalations into an airway cast. Journal of Aerosol Science 24, Supplement 1, S355-S356.
Schmidt, A., Zidowitz, S., Kriete, A., Denhard, T., Krass, S., Peitgen, H.O., 2004. A digital reference model of the human bronchial tree. Computerized Medical Imaging and Graphics 28, 203-211.
Schnabel, C., Gaertner, M., Kirsten, L., Meissner, S., Koch, E., 2013. Total liquid ventilation: a new approach to improve 3D OCT image quality of alveolar structures in lung tissue. Opt.Express 21, 31782-31788.

Schott Medica GmbH, 2017. Precision glassware made by SCHOTT, http://www.schott.com/d/uk/d5759008-05ec-4556-a60a-4b06e341fa54/1.0/precision_glass_rd326.pdf.
Schroter, R.C., Sudlow, M.F., 1969. Flow Patterns in Models of Human Bronchial Airways. Respiration Physiology 7, 341-&.
Schröter, T.J., Koch, F.J., Meyer, P., Kunka, D., Meiser, J., Willer, K., Gromann, L., De Marco, F., Herzen, J., Noel, P., Yaroshenko, A., Hofmann, A., Pfeiffer, F., Mohr, J., 2017. Large field-of-view tiled grating structures for X-ray phase-contrast imaging. Rev Sci Instrum 88, 015104.
Snigirev, A., Snigireva, I., Kohn, V., Kuznetsov, S., Schelokov, I., 1998. On the possibilities of x-ray phase contrast microimaging by coherent high-energy synchrotron radiation. Rev Sci Instrum 66, 5486-5492.
Song, H.K., Dougherty, L., Schnall, M.D., 2001. Simultaneous acquisition of multiple resolution images for dynamic contrast enhanced imaging of the breast. Magn Reson Med 46, 503-509.
Sood, B.G., Shen, Y., Latif, Z., Galli, B., Dawe, E.J., Haacke, E.M., 2010. Effective aerosol delivery during high-frequency ventilation in neonatal pigs. Respirology 15, 551-555.
Sood, B.G., Shen, Y., Latif, Z., Chen, X., Sharp, J., Neelavalli, J., Joshi, A., Slovis, T.L., Haacke, E.M., 2008. Aerosol delivery in ventilated newborn pigs: an MRI evaluation. Pediatr Res 64, 159-164.
Soodt, T., Pott, D., Klaas, M., Schröder, W., 2013. Analysis of basic flow regimes in a human airway model by stereo-scanning PIV. Experiments in Fluids 54.
Stahr, C.S., Samarage, C.R., Donnelley, M., Farrow, N.R., Morgan, K.S., Zosky, G., Boucher, R.C., Siu, K.K.W., Mall, M.A., Parsons, D.W., Dubsky, S., Fouras, A., 2016. Quantification of heterogeneity in lung disease with image-based pulmonary function testing. Scientific reports 6, 15.
Stapleton, K.W., Guentsch, E., Hoskinson, M.K., Finlay, W.H., 2000. On the suitability of k–ε turbulence modeling for aerosol deposition in the mouth and throat: a comparison with experiment. Journal of Aerosol Science 31, 739-749.
Stockhofe, K., Postema, J.M., Schieferstein, H., Ross, T.L., 2014. Radiolabeling of nanoparticles and polymers for PET imaging. Pharmaceuticals 7, 392-418.
Su, W.-C., Cheng, Y.S., 2015. Estimation of carbon nanotubes deposition in a human respiratory tract replica. Journal of Aerosol Science 79, 72-85.
Su, W.C., Cheng, Y.S., 2005. Deposition of fiber in the human nasal airway. Aerosol Science and Technology 39, 888-901.
Su, W.C., Cheng, Y.S., 2006. Deposition of fiber in a human airway replica. Journal of Aerosol Science 37, 1429-1441.
Su, W.C., Wu, J., Marijnissen, C.M., Chengi, Y.S., 2008. Deposition of man-made fibers in a human nasal airway. Aerosol Science and Technology 42, 173-181.
Takeda, M., Ina, H., Kobayashi, S., 1982. Fourier-Transform Method of Fringe-Pattern Analysis for Computer-Based Topography and Interferometry. J Opt Soc Am 72, 156-160.
Tanaka, G., Ogata, T., Oka, K., Tanishita, K., 1999. Spatial and temporal variation of secondary flow during oscillatory flow in model human central airways. Journal of Biomechanical Engineering-Transactions of the Asme 121, 565-573.
Tarran, R., Grubb, B.R., Parsons, D., Picher, M., Hirsh, A.J., Davis, C.W., Boucher, R.C., 2001. The CF Salt Controversy. Molecular cell 8, 149-158.
Taylor, P., Dudek, R., Flaherty, D., Kaempfe, T., 1994. Evaluation of two instruments for the measurement of aerosols. Journal of Aerosol Science 25, 419-423.
te Pas, A.B., Siew, M.L.L., Wallace, M.J., Kitchen, M.j., Fouras, A., Lewis, R.A., Yagi, N., Uesugi, K., Donath, S., Davis, P.G., Morley, C.J., Hooper, S.B., 2009. Establishing Functional Residual Capacity at Birth: The Effect of Sustained Inflation and Positive End-Expiratory Pressure in a Preterm Rabbit Model. Pediatr Res 65, 537-541.
Tearney, G.J., Brezinski, M.E., Bouma, B.E., Boppart, S.A., Pitris, C., Southern, J.F., Fujimoto, J.G., 1997. In Vivo Endoscopic Optical Biopsy with Optical Coherence Tomography. Science 276, 2037-2039.

Theunissen, R., Riethmuller, M.L., 2008. Particle image velocimetry in lung bifurcation models. Particle Image Velocimetry: New Developments and Recent Applications 112, 73-101.
Thompson, R.B., Finlay, W.H., 2012. Using MRI to measure aerosol deposition. J Aerosol Med Pulm Drug Deliv 25, 55-62.
Tropea, C., Yarin, A.L., Foss, J.F., 2007. Springer handbook of experimental fluid mechanics. Springer, Berlin.
Tu, J., Inthavong, K., Ahmadi, G., 2013. Computational fluid and particle dynamics in the human respiratory system, Biological and medical physics, Biomedical engineering,. Springer,, Dordrecht ; New York, p. 1 online resource.
Urbán, A., Zaremba, M., Malý, M., Józsa, V., Jedelský, J., 2017. Droplet dynamics and size characterization of high-velocity airblast atomization. Int J Multiphas Flow in press.
Vakoc, B.J., Lanning, R.M., Tyrrell, J.A., Padera, T.P., Bartlett, L.A., Stylianopoulos, T., Munn, L.L., Tearney, G.J., Fukumura, D., Jain, R.K., Bouma, B.E., 2009. Three-dimensional microscopy of the tumor microenvironment in vivo using optical frequency domain imaging. Nat Med 15, 1219-1223.
Vakoc, B.J., Shishko, M., Yun, S.H., Oh, W.Y., Suter, M.J., Desjardins, A.E., Evans, J.A., Nishioka, N.S., Tearney, G.J., Bouma, B.E., 2007. Comprehensive esophageal microscopy by using optical frequency-domain imaging (with video). Gastrointest.Endosc. 65, 898-905.
van Beek, E.J., Wild, J.M., Kauczor, H.U., Schreiber, W., Mugler, J.P., 3rd, de Lange, E.E., 2004. Functional MRI of the lung using hyperpolarized 3-helium gas. J Magn Reson Imaging 20, 540-554.
Verbanck, S., Darquenne, C., Prisk, G.K., Vincken, W., Paiva, M., 1999. A source of experimental underestimation of aerosol bolus deposition. Journal of Applied Physiology 86, 1067-1074.
Verbanck, S., Ghorbaniasl, G., Biddiscombe, M.F., Dragojlovic, D., Ricks, N., Lacor, C., Ilsen, B., de Mey, J., Schuermans, D., Underwood, S.R., Barnes, P.J., Vincken, W., Usmani, O.S., 2016. Inhaled Aerosol Distribution in Human Airways: A Scintigraphy-Guided Study in a 3D Printed Model. Journal of Aerosol Medicine and Pulmonary Drug Delivery 29, 525-533.
Verbanck, S., Gonzalez Mangado, N., Peces-Barba, G., Paiva, M., 1991. Multiple-breath washout experiments in rat lungs. J Appl Physiol (1985) 71, 847-854.
Verbanck, S., Schuermans, D.L., Paiva, M., Vincken, W., 2001a. Saline aerosol bolus dispersion. II. The effect of conductive airway alteration. Journal of Applied Physiology 90, 1763-1769.
Verbanck, S., Schuermans, D.L., Vincken, W., Paiva, M., 2001b. Saline aerosol bolus dispersion. I. The effect of acinar airway alteration. Journal of Applied Physiology 90, 1754-1762.
Versar Inc., 1988. Current and suggested practices in the validation of exposure assessment models. Office of Health and Environmental Assessment, United States environmental Protection Agency, Washington DC, USA.
Walker, P.S., Conway, J.H., Fleming, J.S., Bondesson, E., Borgström, L., 2001. Pulmonary clearance rate of two chemically different forms of inhaled pertechnetate. Journal of Aerosol Medicine: Deposition, Clearance, and Effects in the Lung 14, 209-215.
Walther, J., Koch, E., 2009. Transverse motion as a source of noise and reduced correlation of the Doppler phase shift in spectral domain OCT. Opt.Express 17, 19698-19713.
Wang, H., Sebrie, C., Ruaud, J.P., Guillot, G., Bouazizi-Verdier, K., Willoquet, G., Maitre, X., Darrasse, L., de Rochefort, L., 2016. Aerosol deposition in the lungs of spontaneously breathing rats using Gd-DOTA-based contrast agents and ultra-short echo time MRI at 1.5 Tesla. Magn Reson Med 75, 594-605.
Wang, Z., Hopke, P.K., Ahmadi, G., Cheng, Y.S., Baron, P.A., 2008. Fibrous particle deposition in human nasal passage: The influence of particle length, flow rate, and geometry of nasal airway. Journal of Aerosol Science 39, 1040-1054.
Weibel, E.R., 1963. Morphometry of the human lung. Springer-Verlag.
Wen, H.H., Bennett, E.E., Kopace, R., Stein, A.F., Pai, V., 2010. Single-shot x-ray differential phase-contrast and diffraction imaging using two-dimensional transmission gratings. Optics Letters 35, 1932-1934.
Westneat, M.W., Betz, O., Blob, R.W., Fezzaa, K., Cooper, W.J., Lee, W.-K., 2003. Tracheal Respiration in Insects Visualized with Synchrotron X-ray Imaging. Science 299, 558-560.

WHO, 1997. Determination of airborne fibre number concentrations. A recommended method by phase-contrast optical microscopy (membrane filter method). WHO, Geneva, p. 53.
Widmann, J.F., Presser, C., Leigh, S.D., 2001. Improving phase Doppler volume flux measurements in low data rate applications. Measurement Science and Technology 12, 1180-1190.
Wieneke, B., 2008. Volume self-calibration for 3D particle image velocimetry. Experiments in Fluids 45, 549-556.
Wieser, W., Biedermann, B.R., Klein, T., Eigenwillig, C.M., Huber, R., 2010. Multi-Megahertz OCT: High quality 3D imaging at 20 million A-scans and 4.5 GVoxels per second. Opt.Express 18, 14685-14704.
Wijesundara, K., Zdanski, C., Kimbell, J., Price, H., Iftimia, N., Oldenburg, A.L., 2014. Quantitative upper airway endoscopy with swept-source anatomical optical coherence tomography. Biomedical Optics Express 5, 788-799.
Wilkins, S.W., Nesterets, Y.I., Gureyev, T.E., Mayo, S.C., Pogany, A., Stevenson, A.W., 2014. On the evolution and relative merits of hard X-ray phase-contrast imaging methods. Philosophical Transactions of the Royal Society A: Mathematical, Physical and Engineering Sciences 372, 20130021-20130021.
Yang, Y., Whiteman, S., van Pittius, D.G., He, Y.H., Wang, R.K.K., Spiteri, M.A., 2004. Use of optical coherence tomography in delineating airways microstructure: comparison of OCT images to histopathological sections. Phys.Med.Biol. 49, 1247-1255.
Yap, Y.L., Tan, Y.S.E., Tan, H.K.J., Peh, Z.K., Low, X.Y., Yeong, W.Y., Tan, C.S.H., Laude, A., 2017. 3D printed bio-models for medical applications. Rapid Prototyping J 23, 227-235.
Yaroshenko, A., Hellbach, K., Yildirim, A.Ö., Conlon, T.M., Fernandez, I.E., Bech, M., Velroyen, A., Meinel, F.G., Auweter, S., Reiser, M., Eickelberg, O., Pfeiffer, F., 2015. Improved In vivo Assessment of Pulmonary Fibrosis in Mice using X-Ray Dark-Field Radiography. Scientific reports 5, 17492.
Zernike, F., 1942. Phase contrast, a new method for the microscopic observation of transparent objects. Physica 9, 686-698.
Zhang, Y., Finlay, W.H., 2005. Experimental measurements of particle deposition in three proximal lung bifurcation models with an idealized mouth-throat. Journal of Aerosol Medicine-Deposition Clearance and Effects in the Lung 18, 460-473.
Zhang, Z., 2010. LDA application methods laser doppler anemometry for fluid dynamics, Experimental fluid mechanics. Springer, Berlin ; London, p. p.
Zhao, Y., Lieber, B.B., 1994a. Steady Expiratory Flow in a Model Symmetric Bifurcation. Journal of biomechanical engineering 116, 318-323.
Zhao, Y., Lieber, B.B., 1994b. Steady Inspiratory Flow in a Model Symmetric Bifurcation. Journal of biomechanical engineering 116, 488-496.
Zhou, Y., Cheng, Y.S., 2000. Particle deposition in first three generations of a human lung cast. Journal of Aerosol Science 31, Supplement 1, 140-141.
Zhou, Y., Su, W.C., Cheng, Y.S., 2007. Fiber deposition in the tracheobronchial region: Experimental measurements. Inhalation Toxicology 19, 1071-1078.
Zwartz, G.J., Guilmette, R.A., 2001. Effect of flow rate on particle deposition in a replica of a human nasal airway. Inhalation Toxicology 13, 109-127.

Figure legends:

Fig. 1. The principle of CTA.

Fig. 2. The LDA principle: a) the optical configuration in the forward, side and backscatter mode, b) fringe pattern with the fringe separation distance *s* and the Gaussian beam diameter *d*, c) the "Doppler burst" signal received by the photodetector and the measurement volume with a conceptual cross-sectional cut.

Fig. 3. a) An example of PSD of the velocity fluctuations of air flow in the centre line of the trachea, with different inspiratory flow rates, tracing 4 μm particles. b) A PDA record of air flow velocity during sinusoidal controlled breathing (TV = 0.5 l, breathing period 4 s) with ten overlapped (phase-averaged) cycles. Time intervals with the laminar and turbulent character of the flow are visible. Zoomed windows document irregularly sampled data and the velocity bias effect. c) Mean axial velocity in a cross section in the trachea for steady inspiration, 30 l/min.

Fig. 4. Typical PIV set-up for planar PIV.

Fig. 5. Velocity vectors and magnitude received from PIV in the upper bronchial tree during inspiration.

Fig. 6. Camera set-up with octagonal tank walls for stereo PIV or volumetric PIV.

Fig. 7. Velocity vectors and normalized vorticity during peak inspiration for different breathing parameters (with permission reprinted from (Adler and Brucker, 2007)).

Fig. 8. Particle trajectories received from 3D-PTV during the peak inspiration phase. Trajectories are colour coded by the velocity magnitude (Janke and Bauer, 2016).

Fig. 9. Example of an automated fiber detection method applied on glass fibers deposited on a nitrocellulose filter: a) a processed image with fibers enhanced by a special algorithm, b) automatically detected fibers in the identical image.

Fig. 10. Schematic representation of the detection of photons using SPECT (a) or planar gamma-camera imaging (b). Only a fraction of the emitted gamma rays reaches the detectors, while others are absorbed in the collimator or never reach the detectors.

Fig. 11. a) Schematic representation of the annihilation process of one positron and one electron, with subsequent emission of two gamma rays. b) Representation of a PET camera. The two photons emitted after the annihilation process are detected simultaneously by two detectors of the ring, placed around the subject under investigation.

Fig. 12. Samples of scintigraphic images from a patient showing deposition pattern from Respimat® SMI before training (a) and after training (b), and from pressurized metered-dose inhaler before training (c) and after training (d). Reprinted with permission of (Brand et al., 2008).

Fig. 13. Shell decomposition of SPECT-CT coronal slices at the level of the right hilum for both nebulizers on the same subject, with the same level of brightness. Both lungs were divided in ten shells (coloured lines through both lungs) distributed from the hilum to the lung periphery. The deposition of the radiolabeled particles of aerosol, depicted in colour, is highly increased with the vibrating-mesh nebulizer with its specific valve-holding chamber in comparison to the constant-output jet nebulizer with a corrugated tube. Activity is seen in the stomach with the vibrating-mesh nebulizer (white arrow). Reprinted from (Dugernier et al., 2017), with permission of Springer.

Fig. 14. a) Representative axial slices of SPECT-CT images obtained at *t* = 0, 24 and 72 hours after administration of 67Ga-labeled particles by intra-tracheal nebulization; SPECT images are co-registered with CT images for easy localization of the radioactivity; b) 3D CT images of the skeleton (grey) co-registered with surface-rendered 3D CT images of the lungs; c) 3D CT images of the skeleton (grey) co-registered with volume-rendered SPECT images of the lungs (green tones).

Fig. 15. Images from a PET scan obtained following inhalation of [^{18}F]FDG aerosol in one subject with asthma and immediately after a methacholine challenge. The baseline scan is reasonably uniform

with ventilation posterior and basal as seen in the one slice in the transaxial plane. On the repeat scan, hot spots are evident throughout the lung as seen on these single slices from the transaxial, coronal, and sagittal planes. Adapted from (Dolovich, 2009).

Fig. 16. Aerosol deposition in the lungs of spontaneously breathing rats using Gd-DOTA-based contrast agents and ultra-short echo time MRI at 1.5 Tesla. Reprinted from (Wang et al., 2016) with permission of John Wiley and Sons.

Fig. 17. Phase-contrast velocimetry with hyperpolarized ^{3}He for in vitro and in vivo characterization of airflow. Reprinted from (de Rochefort et al., 2006) with permission of John Wiley and Sons.

Fig. 18. Phase-contrast helium-3 MRI of aerosol deposition in human airways. Reprinted from (Sarracanie et al., 2015) with permission of John Wiley and Sons.

Fig. 19. Principle of SS OCT. The light from a tunable laser source is guided by optical fibres to a fibre coupler. While one part is reflected at the reference mirror the other part is scattered and partially reflected at the sample, placed underneath a two dimensional scanner, steering the light over the sample. The interfering light is recorded with a detector in the fourth arm of the fibre coupler as a function of wavelength. From the spectrum, the depth information is retrieved.

Fig. 20. Imaging of alveolar structures with OCT in ventilated rats. OCT allows the imaging of morphological features of lung tissue. Even the inner alveolar walls can be visualized. Scale bar 100 µm. While a) shows the 3D image with part of the lung surface (pleura) removed from the data set, b) shows a plane approximately 50 µm beneath the lung surface, c) shows a cross section perpendicular to the pleura. Imaging of deeper alveoli is hampered by the refractive index step between tissue and air.

Fig. 21. Anatomical OCT images of a swine trachea displayed in three different viewing angles. (d)–(f): corresponding CT images. (g): photograph of the swine airway; the region that was imaged is indicated by the dotted square. The *x*, *y*, and *z* scale bars each represent 3 mm. With permission reprinted from (Wijesundara et al., 2014).

Fig. 22. The x-ray properties of different tissues at a given x-ray energy can be described using a complex refractive index n, where β describes how much the tissue will attenuate the x-ray wavefield and δ describes how the tissue will change the phase of the x-ray wavefield. PCXI extracts quantitative measures of how the phase has been altered by soft tissue structures.

Fig. 23. Examples of respiratory images at various scales obtained using synchrotron-based PCXI. a) One side of the trachea (running horizontally) in a mouse, allowing measurements of the airway surface liquid, shown in red (Morgan et al., 2014) and the clearance velocity of inhaled 10–25 µm debris, shown in blue (Donnelley et al., 2014a). Note the upper right is captured with single-grid PCXI, which displays the rate of change of tissue thickness/composition and the lower left with propagation-based PCXI, where edges are enhanced. b) The delivery of a liquid bolus of treatment into the lungs of a mouse, with digital subtraction highlighting treatment location in green (Donnelley et al., 2013). This image also shows the extra detail obtained in propagation-based phase contrast (inset), with dark lines highlighting the edges of major airways and the periphery of the lungs (posterior surface shown with white arrows, anterior with black arrows), and a speckle pattern seen from the lungs.

Table legends:

Table 1. Typical positron emitters (with half-life and positron range).

Table 2. Main features of the experimental methods.

Graphical abstract